Experimental and Numerical Investigations of Novel Passive Micromixers using μ-IF

Yan Feng Fan

A Thesis

in

The Department

of

Mechanical and Industrial Engineering

Presented in Partial Fulfillment of the Requirements

for the Degree of Master of Applied Science (Mechanical Engineering) at

Concordia University

Montréal, Québec, Canada

December 2009

Library and Archives
Canada

Published Heritage
Branch

395 Wellington Street
Ottawa ON K1A 0N4
Canada

Bibliothèque et
Archives Canada

Direction du
Patrimoine de l'édition

395, rue Wellington
Ottawa ON K1A 0N4
Canada

Your file Votre référence
ISBN: 978-0-494-67253-2
Our file Notre référence
ISBN: 978-0-494-67253-2

NOTICE:

The author has granted a non-exclusive license allowing Library and Archives Canada to reproduce, publish, archive, preserve, conserve, communicate to the public by telecommunication or on the Internet, loan, distribute and sell theses worldwide, for commercial or non-commercial purposes, in microform, paper, electronic and/or any other formats.

The author retains copyright ownership and moral rights in this thesis. Neither the thesis nor substantial extracts from it may be printed or otherwise reproduced without the author's permission.

AVIS:

L'auteur a accordé une licence non exclusive permettant à la Bibliothèque et Archives Canada de reproduire, publier, archiver, sauvegarder, conserver, transmettre au public par télécommunication ou par l'Internet, prêter, distribuer et vendre des thèses partout dans le monde, à des fins commerciales ou autres, sur support microforme, papier, électronique et/ou autres formats.

L'auteur conserve la propriété du droit d'auteur et des droits moraux qui protège cette thèse. Ni la thèse ni des extraits substantiels de celle-ci ne doivent être imprimés ou autrement reproduits sans son autorisation.

In compliance with the Canadian Privacy Act some supporting forms may have been removed from this thesis.

While these forms may be included in the document page count, their removal does not represent any loss of content from the thesis.

Conformément à la loi canadienne sur la protection de la vie privée, quelques formulaires secondaires ont été enlevés de cette thèse.

Bien que ces formulaires aient inclus dans la pagination, il n'y aura aucun contenu manquant.

Canada

Abstract

Experimental and Numerical Investigations of Novel Passive Micromixers using μ-IF

Yan Feng Fan

Micromixers are indispensable components in Lab-on-a-Chip and micro total analysis systems (μ-TAS). Typical micromixer applications include the mixing of reagents prior to chemical or biological reactions, drug delivery, medical diagnostics through biological sampling, and DNA sequencing or synthesis. The objective of the present investigation is to develop novel passive microfluidic mixers, which integrate mixing mechanisms of lamination and chaotic advection, through planar channel designs. Lamination is incorporated through repeated separation and combination of the mixing streams, while chaotic advection is implemented through serpentine mixing channels and barriers in the flow. The design includes three innovative in-plane on-chip functional micromixers, of channels ranging in width from 0.05 to 0.2 mm, a constant depth of 0.2 mm, and an overall mixer length of 5 mm. An experimental analysis was carried out to evaluate the mixing performance of the designed mixers. The working fluid is distilled water, with one stream mixed with commercial fluorescence dye. Micro Induced Fluorescence (μ-IF) is used to quantitatively measure instant whole-field concentration distribution in the channels. Images along the axial length of the micromixers were recorded to quantify the mixing performance, over a Reynolds range of 1 to 100, a Péclet range from 10^3 to 10^5, at a Schmidt number in the vicinity of 10^3. The mixing performance shows patterns similar to the Taylor dispersion, which consists of both diffusion and convection. Compared to the designs available in literature, the present micromixers have achieved better mixing efficiency up to 95% with a pressure drop of 20 kPa in a mixing length of 5 mm at $1 \leq Re \leq 100$. The experimental mixing performance is compared with the simulated results, as well as existing experimental data for different designs within the working Reynolds range. The experimental results show a reasonably good correlation with the simulated results.

Acknowledgements

I express my sincere and heartfelt gratitude to my supervisor Professor Ibrahim Hassan for his invaluable supervision and support during this important phase of my career. The knowledge he has imparted on me during my Master study is indispensable and will go a long way into making my career successful.

It is impossible to adequately express my gratitude to my parents, not only for their financial support, but also for encouragement during my hardest time.

I sincerely thank my cousin for his cares on my living. I would also like to thank my group members, Dino, Ayman, Mohamed, Tarek and Tina for their invaluable assistance. I extend my thanks to Dr. Wael Saleh for his indispensable advice and encouragement.

Table of Contents

List of Tables

List of Figures

Nomenclature

Symbols

A	interface area, (m^2)
B	ratio between fluorescence intensity and concentration
C	concentration, (μg/L)
$\overline{C}$	average concentration, (μg/L)
D	diffusion coefficient, (m^2/s)
D_h	hydraulic diameter, (m)
D_n	Dean Number, $D_n = \frac{GW^3}{\mu \nu}\sqrt{\frac{2W}{R}}$
G	pressure gradient at the centerline of pipe, (Pa/m)
H	height of channel, (mm)
I	light intensity
L	length of channel, (mm)
M	mixing efficiency
$\dot{m}$	mass flow rate, (kg/s)
N	total number of sampling
P	pressure drop, (Pa)
Pe	Péclet Number, $\text{Pe} = \frac{D_h V}{D}$
R	channel radius of curvature, (m)

Re	Reynolds Number, $\mathrm{Re} = \dfrac{\rho V D_h}{\mu}$
V	velocity, (m/s)
W	width of channel, (mm)

Greek letters

β	coefficient of response surface model
Γ	numerical diffusion
θ	opening angle, (°)
μ	dynamic viscosity of fluid, (Pa·s)
ν	kinematic viscosity of fluid, (m^2/s)
ρ	density of fluid, (kg/m^3)
σ	standard deviation

Subscripts

f	fluorescence
i	position of node
m	micro-scale mixer
ref	reference value
s	scaled-up mixer
x	vector in x direction
y	vector in y direction

z	vector in z direction

Acronyms

CFD	Computational Fluid Dynamics
CO	Cross-Omega micromixer
DOE	Design of Experiment
IC	Interdigital-Circular micromixer
ICO	Interdigital-Circular-Obstacle micromixer
IO	Interdigital-Obstacle micromixer
LOC	Lab-on-a-Chip
RSM	Response Surface Methodology
SAR	Split-and-Recombine
S/N	Signal-to-Noise
μ-IF	Micro Induced Fluorescence
μ-TAS	Micro total analysis system

Chapter 1

Introduction

A demand for the micro total analysis system, often called μ-TAS or Lab-on-a-Chip (LOC), is growing rapidly, with which easy, fast, efficient and low cost analysis is expected. Microfluidics is a multidisciplinary field consisted of physics, chemistry, engineering and biotechnology, which studies the behaviour of fluids at the microscale. The behaviour of fluids at the microscale can differ from that of 'macrofluidics' since the factors, such as surface tension and viscosity, become dominant compared to inertia. Although the number of applications for microfluidics is currently limited, microfluidics is considered as a highly promising technology for performing rapid and inexpensive chemical and biochemical analyses. Microfluidics is needed to understand the underlying physical mechanics of the molecule or bulk fluid motions in micro/nano configurations and to achieve efficient designs for LOC devices and μ-TAS.

Rapid mixing is essential in many of the microfluidic systems used in biochemistry analysis, drug delivery and sequencing or synthesis of nucleic acids. Biological processes such as cell activation, enzyme reactions and protein folding often involve reactions that require mixing of reactants for initiation. Mixing is also necessary in LOC platforms for complex chemical reactions. The investigation of micromixers as an indispensable component for the realization of microsystems is fundamental for understanding the transport phenomena at the microscale. Rapid and efficient mixing becomes a major challenge facing the microfluidic field. In recent years, some research groups have designed and tested many kinds of micromixers. Some have the potential to be applied in food engineering, chemical or biological reactions such as DNA sequencing or synthesis and biological sampling (Chun et al., 2008). However, in practical applications of microchannel flow, the majority of micro system flows are strongly laminar, due to the high pressure drop in microchannels caused by relatively small channel dimensions. Since only low Reynolds numbers are used, micromixers do not apply turbulent mixing as do conventional mixers, and laminar mixing must be efficiently applied. Compared to turbulent flow, the mixing efficiency in micromixers is very low because the mixing process mainly relies on molecular diffusion. In order to efficiently and effectively complete mixing in practical applications, ideal micromixers which have the features of short mixing length, high mixing efficiency and low pressure drop, are required to satisfy future applications in the biochemistry field at the micro-scale.

In the development of micromixers, experimental mixing studies are a reliable method for analyzing the flow physics. Traditional measurement techniques at the macroscale seem impossible to use at the microscale. New techniques will need to be further relied upon to carry out more than adequate analysis. Micro Induced Fluorescence (μ-IF) has been developed and utilized in the research of micromixer mixing. Through the use of μ-IF technique, a comprehensive experimental study in microchannels is carried out for the micro mixing characteristics. The state-of-the-art, non intrusive experimental technique of μ-IF acquires qualitative and quantitative concentration distribution data. Computational Fluid Dynamics (CFD) has also been widely applied as an assistant analysis tool to understand the flow characteristics. Concentration and velocity distributions could be obtained in order to estimate flow performance and optimize micromixers.

The current study includes four different micromixers. Both μ-IF experiment and numerical simulations are carried out to study the flow characteristics and mixing performance. Chapter 2 presents an extensive literature review on micromixer development, including active micromixers, 3D passive micromixers, 2D passive micromixers, and the applications of fluorescence measurement techniques in the micromixer development. Chapter 3 presents the Cross-Omega micromixer and investigation methods, including mixing visualization, μ-IF principle, test facilities, experimental procedure, numerical simulation, and results. In this chapter, the numerical simulation is validated as an efficient tool to assist the investigation and improvement of micromixers. Chapter 4 presents the numerical investigation of the Interdigital-Circular micromixer. Based on the investigation of the Cross-Omega micromixer, the modification is made in order to increase the mixing efficiency. Systematic optimization methodology is applied to do the optimization. Chapter 5 presents the numerical results of the Interdigital-obstacle micromixer and Interdigital-Circular-Obstacle micromixer, which are developed to further increase the mixing efficiency and reduce the pressure drop. Chapter 6 presents the conclusions and future work.

Chapter 2

Literature Review

This chapter provides a brief review of micromixers and experimental measurements related to micromixing. The classification of micromixers is introduced based on mixing principles. The objectives of this study are listed at the end of this chapter.

2.1 Microfluidic Mixers

Based on the mixing principles, micromixers are mainly classified into two categories: active micromixers and passive micromixers. Active micromixers apply external power to disturb the fluids and enhance mixing. However, passive micromixers are dependent on complex channel structures to overlap and fold the fluids in order to enlarge the interface and improve mixing.

2.1.1 Active Micromixers

Active mixers act on a disturbance imposed by an external field to achieve mixing instead of using complex geometries and/or relatively long channels (Nguyen and Wu, 2005). These external fields inflict time-dependant perturbations on the flow field (DeMello, 2006). Active disturbances may be imposed using moving parts (e.g., stirrer) or no moving parts (i.e., electrokinetics), but in all cases, an external field is required for their operation. Active micromixers can be categorized by the type of external disturbance effects, such as pressure (Bottausci et al., 2007; Liu et al., 2008; Yang et al., 2009), acoustic dynamics (Liu et al., 2002; Liu et al., 2003; Jang et al., 2007), magneto dynamics (Agarwal et al., 2005; Lee et al., 2009; Yang et al., 2008), electro dynamics (Huang et al., 2007; Chun et al., 2008; Luo, 2009) and thermal dynamics (Mao et al., 2002; Tsai and Lin, 2002; Cao et al., 2008).

However, the amplitude and frequency of external power are critical to the mixing efficiency in active micromixers. When the pulsing amplitude and frequency are larger than the critical value, the mixing cannot be improved further. Also, the optimal frequency and amplitude are related to flow rates, which cause complex-operation. Furthermore, biological samples may become damaged in chemical and biological applications due to the application of external fields. Active mixers are often complicated and require complex fabrication processes. In addition, since an external field imposed the disturbance, external power sources are required, which leads to their difficult integration in microsystems. Due to the factors mentioned above, it may be a challenge to implement an active micromixer within a complete micro-system, such as a LOC platform.

Passive micromixers do not have moving parts, but rely on the geometry of microchannels, instead of an external power source, to enhance mixing. Passive micromixers are therefore preferable for future applications due to easy fabrication, lower cost, safe process, and easy-integration into microsystems. In passive micromixers designs, shortening the diffusion length could achieve rapid mixing since the diffusion time is proportional to the square of the diffusive path:

$$t_d \approx L_t^2 / D \tag{2.1}$$

Enlarging the interfacial contact area also increases the mass flux:

$$\frac{\dot{m}}{A} = D\frac{\partial C}{\partial x} \tag{2.2}$$

Lamination and chaotic advection are the main principles to realize the purpose of rapid and complete mixing in passive micromixers. These two principles have been introduced by Branebjerg et al. (1996) and Liu et al. (2000), respectively. The lamination depends on the flow separation to enlarge the contact surface and reduce diffusion paths. Chaotic advection relies on the geometry of the structure to stretch and fold the streams in order to increase the interface between two species. A variety of passive micromixers have emerged, including 3D micromixers and 2D micromixers.

2.1.2 3D Passive Micromixers

In order to generate chaotic advection, a series of 3D micromixers, which have variable channel heights along the entire micromixer, have been applied and developed. Some works have been done (Jen et al., 2003; Lee et al., 2005; Lee et al., 2006; Lee et al., 2007; Xia et al., 2006; Cha et al., 2006; Mouza et al., 2008; Park et al., 2008; Fang and Yang, 2009).

Liu et al. (2000) proposed a 3D serpentine microchannel with a "C-shape" repeating unit as a means of implementing chaotic advection to passively enhance fluid mixing.

Two different channels, straight and square-wave, were developed and compared with the serpentine channel. Experiments demonstrated the ability of flow in this channel to mix faster and more uniformly than either pure molecular diffusion or flow in a "square-wave" channel for Reynolds numbers from 6 to 70. Mixing rates in the serpentine channel at higher Reynolds numbers were consistent with the occurrence of chaotic advection. Visualization of the interface alcohol indicated that the mixing was due to both diffusion and fluid stirring.

A similar micromixer was proposed by Lee et al. (2005), who designed a 3D micromixer which was composed of two microchannel segments, the "main channel" and the "flattened channel", which had different sizes and were arranged perpendicularly. At the intersection of these segments, the fluid inside the micromixer was twisted, and then, in the flattened channel, the diffusion length was greatly reduced, achieving high mixing efficiency. The fluid twisting that led to high mixing efficiency occurred due to different aspect ratios.

Park et al. (2008) improved the serpentine laminating micromixer. The width entering the recombination region was reduced in the F-shape mixing unit, which increased the mixing efficiency to 90% at $Re < 20$.

Park et al. (2004) presented a 3D micromixer based on three processes: stretching and folding, diffusion, and breakup. Stretching and folding the interface of two fluids by rotation enabled enhanced mixing over the entire range of Reynolds numbers. However, rotation was not effective at low Reynolds numbers. In order to improve the mixing at low Reynolds numbers, a breakup method was presented. The breakup method not only actively generated interface, but also enhanced the diffusion process at the interface.

Chang and Cho (2005) presented four different types of static micromixers, including mixers using straight channel flow, microblock-induced alternating whirl flow, microchannel-induced lamination flow and combined alternating whirl–lamination flow. The alternating whirl–lamination (AWL-type) mixer, composed of rotationally arranged microblocks and dividing microchannels, was effective in reducing the mixing length over wide flow rate ranges. Flow visualization verified that the AWL-type micromixer showed mixing lengths of 2.8–5.8 mm for $Re = 0.26$–26.

To obtain chaotic mixing, micromixers with barriers and slanted grooves in microchannels have been developed, as listed in Table 2.2. These micromixers depend on the barriers and slanted grooves to produce helical motions. Therefore, hyperbolic vortices are generated in microchannels.

Slanted grooves micromixers without barriers were designed and investigated. This method was first proposed by Stroock et al. (2002). The slanted grooved mixer (SGM) and staggered herringbone mixer (SHM) were experimentally investigated using the confocal technique. The sketching and folding of flow were observed at $2 \times 10^3 \leq Pe \leq 9 \times 10^5$.

Hu et al. (2006) designed a novel micromixer with Y-type inlet and helical fluid channel, along with herringbone grooves etched on the base of the fluid channel. The mean mixing efficiency around the outlet can reach a value of 90%, even with fluid Reynolds number close to unity. This kind of micromixers could only generate single ellipse motion.

In order to create more complex flow patterns, barriers are placed in microchannels. Two ellipse motions of flow occur, which enlarge the interface. Kim et al. (2004) presented a chaotic passive micromixer called a barrier embedded micromixer (BEM). Chaotic flow was induced by periodic perturbation of the velocity field due to periodically inserted barriers along the top surface of the channel while a helical type of flow was obtained by slanted grooves on the bottom surface.

Yang et al. (2007) proposed a novel design named circulation-disturbance micromixer (CDM). The micromixer consisted of slanted grooves on the bottom and a zigzag barrier on the top. In this micromixer, the fluid produced a transverse motion perpendicular to the main field, and two modulated and hyperbolic vortices of disparate size were induced. Similar research has been conducted by Tung and Yang (2008) and Kang et al. (2008).

Although 3D micromixers are expected to have high mixing performance, fabrication of 3D micromixers layer by layer is complex, and precision alignment between the two layers is difficult.

2.1.3 2D Passive Micromixers

As 3D micromixers are problematic, 2D micromixers have been widely developed due to their ease of fabrication and integration. 2D micromixers have uniform depth microchannels, which are etched in a single plate.

The T-shaped micromixer is the most simple and fundamental 2D micromixer, and has been further investigated by Hoffmann et al. (2006), who reported three regimes of flow: laminar flow, vortex flow and engulfment flow. The disturbed interface between two species at the symmetric plane was found at $Re > 160$. The stretching and thinning of liquid lamellae and the wrapping of two liquid lamellae yielded an enlarged interfacial surface area and led to a considerable increase in the mixing quality. However, sole T-shaped micromixers do not have the capacity to achieve good mixing with low pressure drop.

In order to find out the optimal balance of mixing efficiency and pressure drop, different principles, including split-and-recombine, converging/diverging, Dean Vortex and lamination, are recommended and applied in many studies.

Table 2.1: Summary of 3D channel passive micromixers

Reference	Cross-section	Mixing length	Diffusion coefficient (m^2/s)	*Re* or typical velocity	Best mixing efficiency
Liu et al. (2000)	300 μm × 150 μm	7.5 mm		7-60	98%
Park et al. (2004)	100 μm × 50 μm	4 mm		1-50	> 70%
Lee et al. (2005)	100 μm × 300 μm 300 μm × 10 μm	7.7 mm		2-64 μL/min	> 90%
Chang and Cho (2005)	205 μm × 197 μm	2.8-4.6 mm	1×10^{-9}	0.26-26	100%
Cha et al. (2006)	50 μm × 15 μm	1.4 mm		12.7 μL/min	> 90%
Lee et al. (2006)	400 μm × 100 μm	6 mm	1×10^{-10}	0.012-120	> 90%
Xia et al. (2006)	300 μm × 150 μm	12 mm		0.02-60	
Lee et al. (2007)	100-1000 μm × 365 μm			10-100	90%
Mouza et al. (2008)	0.5-1 mm × 0.5-1 mm			20-350	
Park et al. (2008)		11.75 mm	1×10^{-10}	0.2-20	> 85%
Fang and Yang (2009)	300 μm × 100 μm	6 mm	9.86×10^{-13} — 2.14×10^{-10}	0.01-100	90%

Table 2.2: Summary of 3D micromixers with barriers and slanted grooves

Reference	Cross-section (mm)	Barrier size Cross-section (μm)	Slant groove Cross-section (μm)	Mixing length (mm)	Diffusion coefficient (m^2/s)	*Re* or typical velocity	*M*
Stroock et al. (2002)	0.2 × 0.077		50 × 17.71	3000	4×10^{-10}	0.01-10	> 90%
Kim et al. (2004)	0.24 × 0.06	30 × 40	100 × 9	21	2.8×10^{-10}	0.228-2.28	> 80%
Kim et al. (2004)	Φ 1	100 × 150		9.4	5.3×10^{-9}	6.98-27.92	> 80%
Hu et al. (2006)	0.2 × 0.1		80 × 25	2.95		1-10	98%
Floyd-Smith et al. (2006)	0.2 × 0.06		75 × 15-30			0.004-0.3 ml/min	> 90%
Yang et al (2007)	0.2 × 0.07	20 × 35	50 × 30.6	1.7		0.01-100	60-100%
Wang et al.(2007)	0.2 × 0.0697		30.6 in depth	2		0.007-0.01	60%
Tung and Yang (2008)	0.2 × 0.07	20 × 40	50 × 50	8.1		1.34	> 90%
Kang et al. (2008)	0.2 × 0.077	50 × 51.3	50 × 18	32.34		0.01-30	90%

2.1.3.1 Micromixers with Different Shaped Baffles

Some micromixers contain obstacles or pins placed in microchannels to disturb the fluids. The interfacial area increases and the diffusion path decreases after the fluids pass the obstacles. Different shapes of obstacles are positioned in microchannels. Lin et al. (2007) inserted J-shaped baffles in the T-shaped microchannel to enhance mixing. The mixing performance of the device was investigated by experiment and numerical simulation. The flow located in the center of microchannel had a meander-like path that induced lateral convection in the main channel, resulting in increased mixing. The simulated and experimental results showed that the mixer with J-shaped baffles exhibited better mixing performance than the mixer without baffles, and the percentage of mixing was about 120% - 220% of those without baffles in the range of Reynolds numbers from 5 to 350. The mixing efficiency increased with increasing Reynolds number. After fourteen baffles, the mixing efficiency can reach 64% at $Re = 350$.

Bhagat et al. (2007) presented a micromixer with obstacles positioned within the microchannels to break-up and recombine the flow. The main flow was divided into many substreams after passing the obstacles, which induced a decreased diffusion path and increased interface. Four different shapes of obstacles were designed and simulated: circular, triangular, diamond and stepped diamond. The results showed that the diamond-shaped obstacles had the best mixing performance. Different layouts of obstacles in microchannels were also investigated in order to optimize the design. When the offset was 45 μm, the mixing efficiency improved to 80% at 10 mm for $Re = 0.1$.

Passive micromixers with obstacles in microchannels have also been applied to particle flow mixing. The micromixer with rectangle obstacles used to enhance particle dispersion was designed and tested numerically and experimentally by Bhagat and Papautsky (2008). The conventional effectiveness for particle mixing was examined. The lateral motion of particles was achieved and enhanced by introducing rectangular obstacles. The results showed that the presented micromixer was able to complete ~ 90% fluid mixing in 5 mm and ~ 90% particle dispersion in 3 mm for $Re = 0.05$.

Micromixers with obstacles within the microchannels have good mixing efficiency at low Reynolds numbers (≤ 0.1) or high Reynolds numbers (≥ 300). The former could not achieve rapid mixing and the latter results in high pressure drop. Furthermore, the working fluids located near the side walls have very poor mixing efficiency. Although they have simple structures, these micromixers could not satisfy future applications.

2.1.3.2 Micromixers with Feed-channels

Recycle flows are developed and utilized to enhance mixing. The primary idea is to produce a pressure difference by varying cross-section areas between the downstream and upstream locations in microchannels. The pressure difference drives a part of fluid flow back to the main flow through side channels and pushes the main flow so that mixing is enhanced. Hung et al. (2005) proposed a micromixer, which adds feedback channels on both sides of the main flow channel. The convergent nozzle was used to produce a pressure difference at two inlets of each side channel in order to create recycle flow. After six recycling cells, the mixing efficiency can reach 96% with the pressure drop of 3.5 KPa at $Re = 30$. Jeon et al. (2005) presented a novel recycle micromixer. The geometry, required to perform a recycle flow and effective mixing, was determined by a simulation based on computational fluid dynamics. The simulations were performed at Reynolds numbers of 7, 14 and 28 and channel depths of 100, 150 and 200 μm. The mixing efficiency and the direction of recycle flow were significantly affected by both *Re* and channel depth. The recycle flow was produced at $Re > 7$. The effect of recycle flow on mixing was further improved at higher Reynolds numbers. Increasing channel depth also increased mixing efficiency; the mixing efficiency increased to 97% at a depth of 150 μm for $Re = 42$ after 5 units. Mixing visualization was done to verify the simulation results. Micromixers utilizing recycling flow only operate at a Reynolds number larger than a critical value in order to generate a pressure difference between the inlet and outlet of the side-channels.

2.1.3.3 Micromixers with Vortices Enhancement

In order to enlarge the interface area between species, generating vortices in the microchannels is an ideal method. Based on the vortices pattern, vortices generated in microchannels could be classified into Dean vortices and expansion vortices.

Dean vortices could be generated in curved channels for pressure-driven flow, which was first explored by Dean. Dean vortices are considered as an effective flow characteristic to enlarge the interface area at high Reynolds numbers. In these geometries, curvature amplifies a lateral instability that drives a secondary cross-channel flow. The Dean number characterizes this secondary flow, and defined as

$$D_n = \frac{Gw^3}{\mu\nu}\sqrt{\frac{2W}{R}} \tag{2.3}$$

where G is the centerline pressure gradient driving the primary flow, R is the channel radius of curvature, W is the channel width, μ is the fluid dynamic viscosity, and ν is the kinematic viscosity. In a straight channel ($D_n \sim 0$), pressure-driven flow is unidirectional and develops a parabolic profile with the fluid moving down the center of the channel traveling faster than the fluid traveling along the walls or along the top and bottom. When the flow is directed through a curved channel by pressure, the fluid moving down the center experiences a higher centrifugal force than the surrounding liquid. As a result, a pair of counter-rotating vortices forms that ejects fluid from this high-speed core toward the outer wall. At higher values of D_n, and depending on the aspect ratio of the channel cross-section, additional vortices and time-dependent

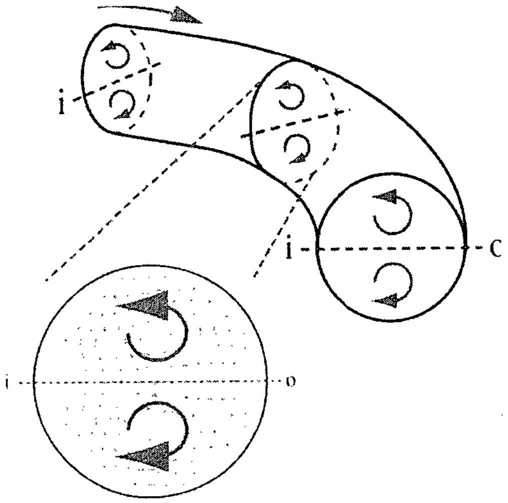

Sudarsan and Ugaz (2006)

Table 2.3: Summary of passive micromixers with obstacles and feed channel

Reference	Obstacle or feed channel	Cross-section (μm)	Mixing length (mm)	D (m^2/s)	*Re*	*Pe*	*M*
Wang et al. (2002)	Circular-shape	300 × 100	1.2	1.2×10^{-9}		200	55%
Lin et al. (2007)	J-shape	500 × 280	5	1×10^{-10}	5-350		> 70%
Bhagat et al. (2007)	Diamond-shape	200 × 55	10	1×10^{-10}	0.01-100		80%
Bhagat et al. (2008)	Rectangular-shape	200 × 50	5	1×10^{-10}	0.05		90%
Jeon et al. (2005)	Feed channel	(50-300) × (100-200)	17.1	1×10^{-9}	7-42		100%
Hung et al. (2005)	Feed channel	(20-400) in width	14.7		5-30		96.8%

oscillations can be formed.

Howell et al. (2004) proposed a micromixer with a curved channel. The movement of pigmented fluid from the inner wall to the outer wall was observed. The vortices were first seen at Reynolds numbers between 1 and 10 and became stronger as the flow velocity was increased. Vortex formation was monitored in channels with depth/width ratios of 0.5, 1.0, and 2.0. The lowest aspect ratio strongly suppressed vortex formation. Increasing the aspect ratio above 1 appeared to provide improved mixing.

Schönfeld and Hardt (2004) numerically investigated helical flows in curved channels and structured channels. Transverse flows in structured microchannels were compared to secondary flow patterns in curved square channels. The corresponding helical flows were analyzed for Dean numbers ranging from 1 to 900. Similar chaotic flow patterns can also be induced with a more simple geometry which relies on curved channels. Based on the results a new type of micromixer was proposed that relied on the transition of the secondary flow pattern from two to four vortices.

Jiang et al. (2004) extended the work and presented a four-element meander mixer relying on alternately switching between different flow-patterns exhibiting four Dean vortices. The experimental and numerical results showed that the mixing performance found for D_n above 140 was different from that at lower D_n; the periodic switching between different vortex patterns led to efficient mixing, manifesting itself in an exponential growth of interfacial area. The residence-time distributions in the mixing channel were also studied numerically, which indicated that hydrodynamic dispersion was substantially reduced relative to a straight channel due to mass-transfer enhancement originating from the transversal redistribution of matter in the chaotic flow.

In order to strengthen the Dean vortices in curved channels, Sudarsan and Ugaz (2006) explored compact spiral-shaped flow geometries designed to achieve efficient mixing. This mixer consists of a series of spiral shaped channels arrayed along the flow path. Channels of different radii were connected to generate more durable Dean vortices. Mixing studies were carried out at flow rates corresponding to Reynolds numbers ranging from 0.02 to 18.6. Transverse Dean flows were induced that augmented diffusive transport and promoted enhanced mixing in considerably shorter downstream distances as compared to conventional planar straight channel designs. Mixing efficiency can be further enhanced by incorporating expansion vortex effects via abrupt changes in cross-sectional areas along the flow path.

In the same year, this group presented two new micromixers which combined the effects of Dean vortices, lamination and diverging. The improved mixing was accomplished by harnessing a synergistic combination of Dean vortices that arose in the vertical plane of curved channels as a consequence of an interplay between inertial, centrifugal, and viscous effects, and expansion vortices that arose in the horizontal plane due to an abrupt increase in a conduit's cross-sectional area.

Besides the application of curved channels, zigzag and wave-like channels were also utilized to generated Dean vortices. Mengeaud et al. (2002) used a zigzag structure to produce secondary flow at high Reynolds numbers. As the Reynolds number increased, the laminar recirculation at the corner increased. However, this work was constricted in the 2D numerical simulation. Further work was done by Yang and Lin (2006). They investigated a zigzag micromixer by numerical simulation and flow visualization. Two cases with and without variable densities were simulated. Double interfaces were formed under conditions of flow in a micro planar serpentine channel at $Re = 16$. A similar design was employed by Tafti et al. (2008) and Chen and Cho (2008), who applied periodic sine wave-like structures to enhance mixing efficiency.

Expansion vortices are generated based on the converging-diverging principle. When the cross-section varies sharply from narrow to wide, the fluid expands in order to fill the flowing regimes. The expansion of fluid creates vortices at the corner of the microchannels and takes a stirring role to increase the mass-advection effect.

Shih and Chung (2008) designed a micromixer that applied the converging/diverging principle. The working fluid was compressed after entering the gap with a shorter width. The mixing efficiency was increased due to the reduced diffusion length and fluid compression. Flow separation and vortices were observed in the mixing chamber, and were caused by the diverging effect. Backflow motion within the mixing chamber assisted the flow in stretching the interface between two species.

Chung et al. (2008) presented a planar micromixer with three baffles. The presence of three baffles caused the flow to separate, and created recirculation and back flow within mixing chambers. Both numerical simulations and experiments were performed to investigate the mixing process within the mixing chambers of the planar micromixer with three baffles at varied baffle height. The fluid mixing was greatly influenced by the baffle height and *Re*, related to the size of recirculation zone. Larger baffle heights or *Re* produced larger recirculation zones and convective mixing. The micromixer with 350 μm high baffles in 400 μm wide channels resulted in over 95% mixing at $Re = 80$ from the simulation results. The experimental results confirmed the above simulation results qualitatively.

2.1.3.4 Micromixers with Circular Chambers

Circular micromixers are a type of multi-lamination mixer, which utilizes self-rotation of the sample fluids from multiple injection channels to produce three-dimensional vortices in the circular mixing chamber at low *Re*, thereby enhancing mixing performance.

Jin et al. (2006) investigated two fluid mixing in a swirl micromixer. The mixing performance of the two fluids was evaluated by varying the Reynolds numbers and the mass fractions of glycerol in water. The numerical results showed that the acceptable uniformity of mixing at $Re = 0.1$ was primarily attributed to time-consuming molecular diffusion, whereas the cost-effective mixing at $Re > 500$ was obtained because of the generation of the swirling flow. The increasing mass fraction of glycerol in water was found to attenuate the mixing performance. The preliminary microscopic visualization of the two-fluid mixing at $Re = 1300$ demonstrated consistency with the numerical results.

Liu et al. (2008) presented the design and characterization of a new multi-inlet vortex mixer (MIVM). The four-stream MIVM was simulated for the control of both the supersaturation and the final solvent quality by varying stream velocities. The design enabled the separation of reactive components prior to mixing and mixing of streams of unequal volumetric flows. Adequate micromixing was obtained with a suitably defined Reynolds number at $Re > 1600$.

The rotation mentioned above was produced at high Reynolds numbers. In order to apply the circular chamber micromixers at a low range of Reynolds numbers, Lin et al. (2005) proposed a 3D vortex micromixer for μ-TAS applications which utilized self-rotation effects to mix fluids in a circular chamber at low Reynolds numbers. The two inlet channels were divided into eight individual channels tangent to a 3D circular chamber for the purpose of mixing. Numerical simulations and experimental flow visualization were employed to predict the self-rotation phenomenon and to estimate the mixing performance under various Reynolds number conditions. The results indicated that the self-rotation effect was induced at $Re \geq 2.32$. The mixing performance can be as high as 90% within a mixing chamber of 1 mm diameter at $Re = 4$.

Table 2.4: Summary of passive micromixers applying vortex stirring principle

Reference	Vortex style	Structure shape	Cross-section	Mixing length	D (m^2/s)	*Re*	D_n	*M*
Schönfeld and Hardt (2004)	Dean vortex	meander	200 μm × 100 μm		1×10^{-9}		1-900	
Yang and Lin (2006)	Dean vortex	Zigzag	(25-50) μm × 25 μm	0.65 mm		2-16		
Sudarsan and Ugaz (2006)	Dean vortex	meander	400 μm × 29 μm	17.5 mm	3×10^{-10}	7.8-31	2.3-9.1	90%
Sudarsan and Ugaz (2006)	Expansion vortex	meander	(100-500) μm × 29 μm	7.8 mm	3×10^{-10}	6.4-32.2	1.7-8.6	80%
Sudarsan and Ugaz (2006)	Dean vortex	meander	150 μm × 29 μm	44.49 mm	3×10^{-10}	0.02-18.6		90%
Kumar et al. (2006)	Dean vortex	meander				0.1-100		
Jiang et al. (2004)	Dean vortex	meander	200 μm × 100 μm				10-200	
Howell et al. (2004)	Dean vortex	meander	1.27 mm × 0.64 mm			3-60		
Shih and Chung (2008)	Expansion vortex	Converging /Diverging	400 μm × 120 μm		3.23×10^{-10}	0.1-40		> 90%
Chung et al. (2008)	Expansion vortex	Converging /Diverging	400 μm × 140 μm	8 mm	3.23×10^{-10}	40-80		99.1%

Later, Lin et al. (2007) improved their design and proposed a rapid circular microfluidic mixer in which an unbalanced driving force was used to mix fluids in a circular chamber at low Reynolds numbers. Each inlet port was separated into two individual channels, which were then attached to opposite sides of the circular mixing chamber. The unequal lengths of these inlet channels generated an unbalanced driving force, which enhanced the mixing effect in the mixing chamber. The numerical and experimental results revealed that the mixing performance can reach 91% within a mixing chamber of 1 mm diameter at *Re* = 3. Additionally, the results confirmed that the unbalanced driving force produced a flow rotation in the circular mixer at low Reynolds numbers, which significantly enhanced the mixing performance.

Table 2.5: Summary of passive micromixers with circular chambers

Reference	Cross-section at inlets (mm)	Inlet No.	Height (mm)	Diameter of chamber	D (m^2/s)	*Re*	*M*
Lin et al. (2005)	0.1×0.04	4-4	1	830 μm	1×10^{-7}	0.5-6	90%
Jin et al. (2006)	2×2	1-1	12	60 mm	7.2×10^{-10}	0.1-1300	67%
Lin et al. (2007)	0.104×0.084	2-2	1	815 μm	1×10^{-7}	0.5-6	> 90%
Liu et al. (2008)	110×150	2-2	1500	600 mm		800-5000	

2.1.3.5 Micromixers with Interdigital Lamination

The interdigital lamination structure is emerged and used to design passive micromixers to increase the interface area and decrease the diffusion path. The principle is to divide the main flow into *n* substreams, which recombine to create the interdigital flow pattern, causing diffusion to occur at a faster rate. Interdigital micromixers have been designed and investigated experimentally (Koch et al., 1998; Bessoth et al., 1999; Ehrfeld et al., 1999; Hardt and Schönfeld, 2003; Hessel et al., 2003; Löb et al., 2004; Pennemann et al., 2005; Ducrée et al., 2006; Lee and Kwon, 2009) and theoretically (Drese, 2004; Wu and Nguyen, 2005; Cerbelli and Giona, 2008).

Based on the flow direction, the interdigital micromixers are classified into counter-current flow interdigital micromixers and co-current flow interdigital micromixers. Counter-current flow interdigital micromixers were numerically studied by Serra et al. (2005) and used to apply chemical reactions by Ehrfeld et al. (1999) and Fukuyama et al. (2002). However, many research groups focus on co-current flow interdigital micromixers.

Koch et al. (1998) proposed two different micromixers with lateral and vertical mixing based on the lamination principle. The first mixer separated the main flow into partial flows, which were laterally alternated in order to increase the boundary surface between the liquids. The second mixer superposed two fluids by injection of one liquid into the other. A Similar concept of lateral mixing was applied in the micromixer presented by Bessoth et al. (1999). The two working fluids were divided into many substreams before mixing. Then the substreams well combined to complete the interdigital flow pattern in order to increase the interface and reduce the diffusion length compared to the T-shaped micromixer. The mixing regime was selected as a straight channel. After 15ms, the mixing efficiency could reach 95%.

Bessoth et al. (1999) were the first to mention the effect of laminar width distribution on mixing. They proposed that the relatively long time between a high percentage of mixing being achieved and completion was due to the fact that the fluid laminae at the edge of the channel were thicker than the ones in the center. Diffusion occurred in both directions, apart from the outermost laminae, which can only mix with one neighbouring layer. However, there was no progress on the modification based on the concept.

In order to improve the mixing performance of interdigital micromixers, Hessel et al. (2003) and Hardt and Schönfeld (2003) individually experimentally and numerically investigated four interdigital structure micromixers with different focusing regimes: rectangular, triangle, slit-shaped and superfocus. The uniform lamellae were applied and the lamellar number of each species was fixed at fifteen. The micromixer with the superfocus regime achieved better mixing than the others, and was considered to be the optimal design. Gas/liquid and liquid/ liquid mixing in this kind of micromixer have also been investigated (Löb et al., 2004; Serra et al., 2005; Pennemann et al., 2005; Löb et al., 2006). The optimization of the superfocus mixer was performed with an analytical model in the creeping laminar flow regime by Drese (2004). Both the focusing section and the mixing channel were analyzed to determine the influence of design dimensions of mixer on the mixing quality. Each lamina had a constant width of 0.1mm for both species, and the opening angle was 50°. The width and length of the mixing channel were discussed according to the height of the mixing channel and pressure drop. All analysis was based on fixing the mixing quality at 99%. Increasing the pressure drop induced reduced mixing quality in the focusing regime. When the height of the channel was beyond a critical value at each pressure drop, the effect of channel height disappeared. This critical value of channel height decreased with increasing pressure drop. Cerbelli and Giona (2008) analyzed the dynamics of mixing that took place in the mixing channel downstream of the interdigital apparatus with a rectangular focusing regime. The mixing length was estimated through a mathematical model. Three different flow profiles at inlet (plug, shear and Poiseuille flow), were applied to determine the effect of the flow profile on mixing length. The mixing length was significantly affected by the flow profile at a high degree of lamination of the feed stream, and insignificantly by the lamellar thickness.

However, all studies mentioned above only focused on the focusing structure and mixing length, and showed bad mixing quality near the inner wall. Based on the interdigital micromixer proposed by Hessel et al. (2003), Lee and Kwon (2009) presented an improved interdigital micromixer, which consisted of interdigital inlets and recirculation zones in order to enhance the mixing over a range of high Reynolds numbers. The vortex was formed in the recirculation zone at $Re \geq 100$, and enhanced the mixing by convection. Mixing was completed at $Re = 800$.

2.1.3.6 Micromixers with Split-and-recombine

The split-and-recombine (SAR) mixers have been widely used in recent micromixer development. This kind of mixer creates sequential multi-lamination patterns, which are different from the parallel approach of the interdigital feeds. In contrast to the commonly applied interdigital multi-lamination approach used in micro-reaction technology, SAR mixing relies on a *multi*-step procedure. The basic operations are: splitting of a bi- or multi-layered stream perpendicular to the lamella orientation into sub-streams which are then recombined. Usually, these basic steps are accomplished by one or more reshaping steps. The lamination structure of flow occurs in the mixing regimes instead of the inlet zones, as is the case with interdigital micromixers.

Branebjerg et al. (1996) theoretically studied a micromixer based on multistage multi-layer lamination. Two micromixers were proposed, denoted as horizontal and vertical lamination. The micromixer was designed to work in the flow range 1 - 10 pl/min with a Reynolds number less than unity and an undisturbed laminar flow pattern. Based on the concept of Branebjerg et al. (1996), research was conducted by Schönfeld et al. (2004) and Hardt et al. (2006).

Schönfeld et al. (2004) investigated an optimized split-and-recombine micromixer with uniform ‘chaotic’ mixing, using computational fluid dynamics (CFD). The mixing was performed for Reynolds numbers in the range of about 1 to about 100. A positive

Table 2.6: Summary of lamination micromixers

Reference	Number of lamination pattern	Cross-section of substream channel (μm)	Flow type	D (m^2/s)	*Re* or typical velocity
Bessoth et al. (2005)	2 × 16	50	Co-current		3-200 μL/min
Ehrfeld et al. (1999)	2 × 15	(25 – 40) × 300	Counter-current		50-3000 ml/h
Hessel et al. (2003)	2 × 15	60 × 150	Co-current	1×10^{-9}	5-1000 ml/h
Lee and Kwon (2009)	2 × 4	500	Co-current	1×10^{-9}	10-1000

finite-time Lyapunov exponent, which was generic feature of multi-step SAR mixers, was associated with chaotic advection.

Hardt et al. (2006) further investigated SAR mixers theoretically and experimentally. The theoretical model relied on solving 1D diffusion equation in a frame of reference moving with the flow, thus avoiding the usual numerical diffusion related to the prediction of high-Péclet number mixing. In the high Péclet-number regimes, diffusive mass transfer was more or less negligible up to a certain stage of lamella multiplication. Diffusion then rapidly reduced the peaks of the concentration profile and led to a fully mixed state.

In order to simplify the fabrication process, the split-and-recombine principle has also been achieved in 2D micromixer developments in recent years. Some works have been done based on this principle (Hong et al., 2004; Nguyen et al., 2008; Chung et al., 2008; Hsieh and Huang, 2008; Chung and Shih, 2007; Chung and Shih, 2008).

Hong et al. (2004) applied the Tesla structure to split and recombine flows to enhance the mixing. The total length was only 10 mm. It was dependent on the combined effects of diffusion and convection. The pressure drop was less than 10 kPa at approximately Re = 100, and the mixing efficiency can reach more than 90%. The main fluid was divided into substreams which decreased the diffusion path. The impact of substreams against each other at the position of recombination was also able to enhance the mixing.

Chung and Shih (2007) proposed and investigated a planar three-rhombus micromixer with two constriction elements by simulations and experiments. Higher constriction elements with low blockage ratios may significantly enhance fluid mixing by combining principles of split-and-recombine, focusing/diverging, and recirculation. The local high flow velocity induced by the high constriction element provided both high inertial forces and centrifugal forces for enhancing mixing efficiency under asymmetrical flow. The smaller blockage ratio and higher Reynolds number resulted in higher mixing efficiency. Chung and Shih (2008) improved their design and introduced a rhombic micromixer with a converging-diverging nozzle at the outlet. The new design reduced the large pressure drop created by the blockage. In order to maintain a high mixing performance, a converging-diverging nozzle was added at the outlet. As mixing efficiency is dependent upon Reynolds numbers and geometrical parameters, the parameters of number of rhombi, turning angle and absence or presence of the converging-diverging element were selected for optimization. A smaller turning angle, higher Reynolds number and increasing number of rhombi resulted in better fluid mixing due to the occurrence of increased recirculation, which was beneficial for both the increased interfacial contact area between two species and the convective mixing.

2.2 Summary and Motivation

Recently, there has been a large demand for the development of smart disposable LOC for the application of clinical diagnostics and biochemical detection systems. The implementation of LOC technology at the microscale requires the development of several basic devices, such as micropumps, microvalves, micromixers, etc. Numerous researchers have focused on developing conventional micropumps and microvalves in recent years. In the development of a smart disposable LOC, smart micromixing on a chip has been considered to be one of the most difficult tasks, since fluid mixing in a microchannel is difficult due to its low Reynolds number. In order to realize the smart micromixing module, innovative on-chip mixers should be first explored, achieving the fundamental requirements of passive, disposable, and functional formats. Thus, new smart passive fluidic micromixers will be investigated in this research.

Some researchers have been developing active micromixers in order to achieve the requirements of LOC for micromixers: rapid mixing, high mixing efficiency, low pressure drop, and easy-integration and operation. However, there have been several challenging issues related to these micromixers, such as fabrication, system integration, reliability, and complex control circuitry. Increasingly, researchers are looking at passive microfluidic components, or smart materials/structures, to realize the same functions. These passive microfluidic components or smart materials/structures should have smart functionality without further complex control/actuation due to their special structures,

Table 2.7: Summary of split-and-recombine passive micromixers

Reference	Mixing length (mm)	Cross-section (mm)	D (m^2/s)	*Re* or typical velocity	*M*
Schönfeld et al. (2004)	960	2 × 4		1-100	
Nguyen et al. (2008)	3.2	0.011 × 0.02	1×10^{-9}	5.5-56	90%
Hsieh and Huang (2008)	10	0.2 × 0.2	1×10^{-9}	0.027-0.081	> 91%
Hong et al. (2004)	10	0.2 × 0.11	1×10^{-10}	1-100 μL/min	90%
Hardt et al. (2006)	96	2 × 4	1×10^{-11}	50-4000 ml/h	100%
Chung et al. (2008)	10.25	(0.2-0.3) × 0.13	3.23×10^{-10}	0.1-100	90%
Chung and Shih (2007)	10.25	0.25 × 0.12	3.23×10^{-10}	1-50	90%

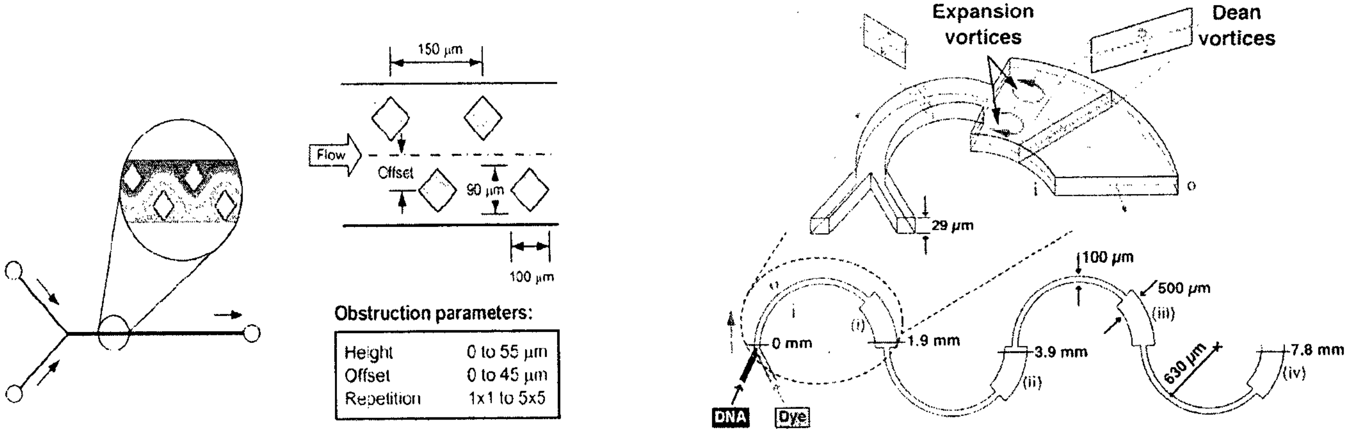

(a) Bhagat et al. (2007)

(b) Sudarsan and Ugaz (2006)

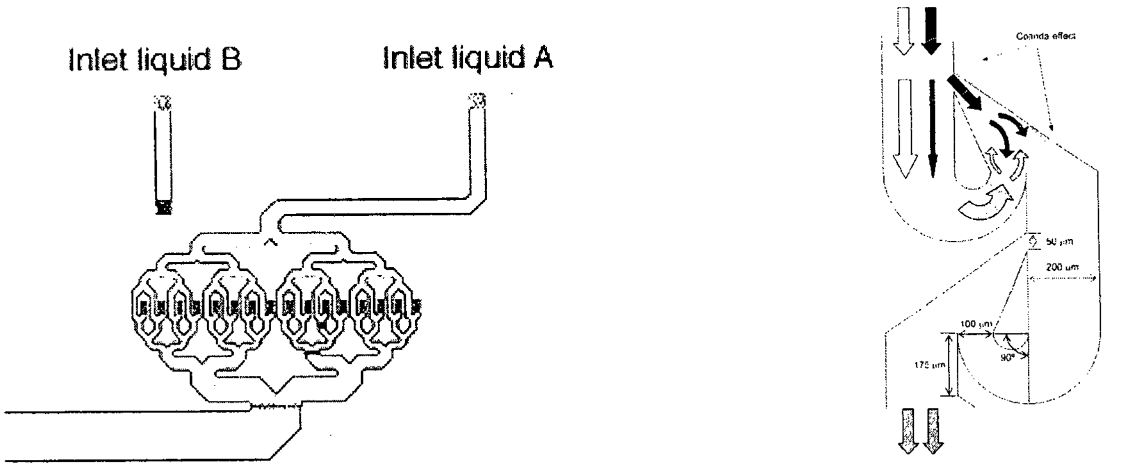

(c) Bessoth et al. (1999)

(d) Hong et al. (2004)

Figure 2.1: 2D passive micromixers with different mixing principles. (a) Obstacles. (b) Vortex. (c) Lamination. (d) Split-and-recombine.

working principles, or material characteristics. Three-dimensional micromixers have been developed and show very good mixing performance. Current generation micromixing techniques, however, have made useful contributions to the field of microfluidics. Many of them require channel geometries that utilize complex fabrication techniques. Moreover, the problem arises when two patterned surfaces need to be aligned, assembled, and bonded with accurate precision. In cases where the bonding is irreversible, the opportunity to realign in case of initial error is nonexistent and many of the fabrication steps have to be repeated.

In order to accurately characterize the mixing process, numerical simulations and experiments have been used to assist in understanding the mixing performance in microchannels by almost all researchers. In numerical simulation, commercial CFD software is applied, such as Ansys-CFX, CFD-ACE, and Fluent. Based on different grid systems and different commercial codes, different results are obtained for the same design. Furthermore, ND (numerical diffusion or artificial diffusion) reduces the accuracy. Therefore, numerical simulation alone seems to be an impossible tool to accurately estimate the mixing efficiency of micromixers. Experiments must be conducted to verify the accuracy of numerical simulations. However, different research groups employ different experimental techniques to determine when the fluid streams become mixed. These experiments carried out using techniques based on observing color changes at the interface between streams of different dyes and reagents (e.g., phenolphthalein and sodium hydroxide) that react to form a visible interfacial front between streams. In addition to these "top view" measurement techniques, some groups have employed confocal microscopy in order to image cross sectional slices of the flow field. The mixing efficiency is related to the height of focus plane. The situation becomes even more complex when this variety of experimental characterization technique is further combined with the use of different working fluids and different data analysis algorithms, as shown in Tab. 2.8. For the same design, different experimental techniques and analysis algorithms could produce different results for mixing efficiency. It also seems that a single experiment could not obtain the convinced results.

The motivation behind this work is to overcome some of the limitations associated with the above-mentioned micromixers and investigation methods. Considering all these factors in both active and passive micromixers, there still exists the need to build mixers that achieve passive micromixing in the shortest possible distances by using simplified microchannels (ideally, planar 2-D smooth-walled) that can be easily constructed (ideally, in a single lithography step). The purpose of this research is to design ideal planar passive micromixers, which are able to achieve rapid mixing with high mixing efficiency, and low pressure drop over a wide range of working Reynolds numbers, for disposable LOC. Improved investigation methods will lead to more reliable and accurate results.

2.3 Objectives

The mixing concept, design, fabrication, simulation, and characterization of the proposed microfluidic devices will be discussed in this study. Both numerical simulations and μ-IF experiments are applied to investigate the mixing performance. The following objectives are completed:

- ➢ A passive micromixer with T-shaped inlet, denoted as CO, is designed and investigated by experiment and numerical simulation. This micromixer contains two

Table 2.8: Summary of techniques used in micromixers development

Reference	Solution	Solute	Image	Intensity	CFD
Liu et al. (2002)	DI-water	A mixture of phenolphthalein and sodium hydroxide	Top		CFD-ACE
Wu and Li (2008)	DI-water	Fluorescein with sodium carbonate/bicarbonate	Top	σ	COMSOL MULTIPHYSICS
Lin et al. (2005)	Sodium borate	Rhodamine B	Top	σ	CFD-ACE
Lee and Kwon (2009)	water	Black dye	Top	η	Fluent
Lin et al. (2007)	DI-water	Black ink	Top	ε	CFD-ACE
Chung et al. (2008)	DI-water	Quick Blue ink	Top	M	CFD-ACE
Sudarsan and Ugaz (2006)	DI-water	Blue and yellow food color	Top	Mixing Intensity	
Sudarsan and Ugaz (2006)	DI-water	Rhodamine 6G	Cross-section	σ	

units named “Cross-unit” and “Omega-unit”, which achieve mixing through the Dean vortices and split-and-recombine principles. The corners are applied to change the flow direction. Due to the uneven velocity distribution caused by pressure-driven, the Dean vortices are generated to stir the fluids in order to increase the interface and enhance the mass-advection.

- Based on the investigation of CO micromixer, the improvement is made to increase the mixing efficiency and reduce the pressure drop. Interdigital-circular micromixer, denoted as IC, which combines lamination and split-and-recombine principles, is presented to achieve good mixing at a wide range of Reynolds numbers. Since the numerical simulation is verified by the experiment in the investigation of the CO micromixer, the IC micromixer is studied by numerical simulation.
- In order to improve the mixing in the IC micromixer, an interdigital-obstacle micromixer is designed and investigated by numerical simulation. This micromixer applies the obstacles to generate the meander-like mixing path in order to enhance the mass-advection effect at low Reynolds numbers.
- The Micro Induced Fluorescence (μ-IF) technique is applied as an experimental investigation tool to quantitatively measure the mixing efficiency. It is a whole field instant concentration measurement technique. Rhodamine 6G is selected as the media to achieve the mixing measurement.
- Since the fluorescence intensity over the channel depth is received, the flow characteristics perpendicular to the flow direction could not be obtained from the experiment. Numerical simulation is utilized to assist in understanding the mixing performance in microchannels. The results will be verified by experiment.

Chapter 3

A Novel Planar Passive Micromixer

A novel planar passive micromixer is proposed and investigated by experiment and numerical simulation. The micro Induced Fluorescence technique is applied for quantitative concentration measurement. Mixing visualization is performed to observe the mixing performance along the entire micromixer. Numerical simulation is also applied to investigate the flow characteristics and mixing performance since the μ-IF is limited in term of obtaining enough mixing information. The numerical results are validated by the experimental data.

3.1 Experimental Investigation of Mixing Quality

3.1.1 Cross-Omega Micromixer (CO)

It is known that a reduction in the diffusive path between two fluid streams along with an increase in the interfacial contact area will enhance the mixing quality. Therefore, the geometry dimensions and structure are very important for passive micromixers, as they manipulate the flow without the use of external fields. Figure 3.1 shows the schematic of the present scaled-up mixer with a T-shaped inlet. The structure can be divided into two units named "cross" and "omega". The compound of one cross unit and one omega unit is called "cell". Two cross units are connected with an omega unit. Consecutive omega units have the same size and an angle difference of 180°. Dean vortices, split-and-recombine in cross units, and focusing/diverging fluids in omega units are considered to be the mixing mechanisms used to enhance the mixing in this design. Two pressure-driven mixing species are pushed into the mixing channels. The main flow is split into two substreams at the entrance of the cross unit, which then recombine at the exit. This induces an increased mixing length and reduced diffusion length between the two species in each branch of the cross unit. In the omega unit, the diffusion path is shortened because of the smaller width of the channel. The focusing/diverging occurs at the entrance and exit of the omega unit, which increases the mixing efficiency. Furthermore, variable widths of the omega unit also lead to the focusing/diverging effect. The right angles in the cross units and the omega units change the direction of flow, and Dean vortices may be generated due to the centrifugal force.

3.1.2 Fabrication of Test-section

To employ the μ-IF technique, the test-sections must be optically accessible at the bottom of microchannels in order to transmit the excited light. Test sections fabricated in glass, PDMS, or transparent plastic which are entirely optically clear, possess the advantages of increased illumination, ease of test section alignment with the microscope objectives, and a readily observable test setup. In addition, a smooth inner wall surface provides a good optical path for μ-IF measurement and improves accuracy.

A scaled-up micromixer is manufactured in order to provide a rapid and effective flow visualization experiment, and to reduce the cost. Since the test-section is scaled-up, conventional machining methods are used in the fabrication. The thickness of the upper and lower acrylic slabs are 3 mm and 6 mm, respectively. The channels have a constant depth of 3 mm. The channels are milled in the bottom slab, after which the thin acrylic slab is bonded to the top to close the channels. Flexible tubes are glued to the two inlets and the outlet. The inlets and outlet have dimensions of 4.5 mm and 3 mm in width, respectively.

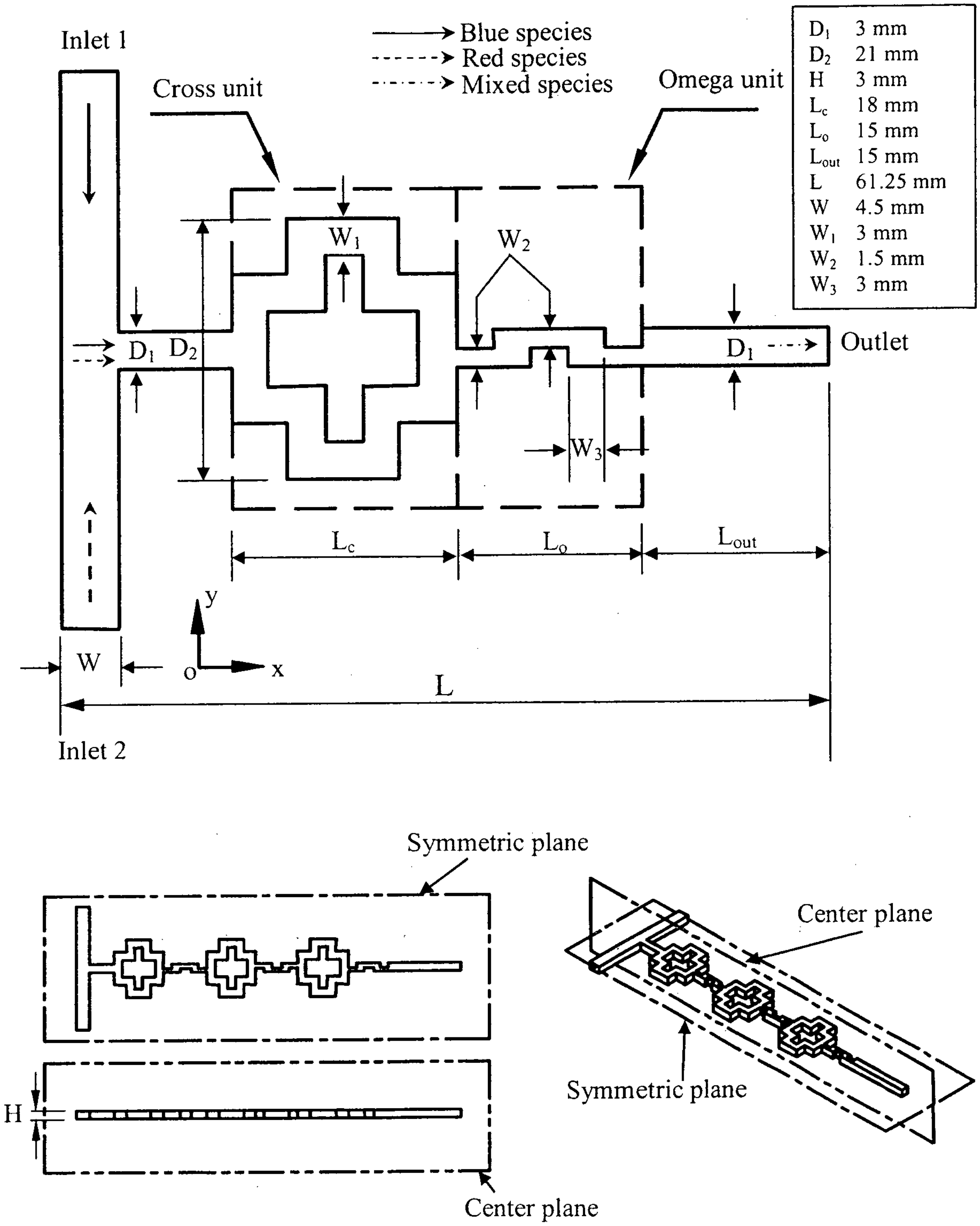

Figure 3.1: Schematic of the present micromixer and 3D model with three cells.

3.1.3 Geometric and Dynamic Similarity

For complete similarity between the scaled-up mixer (s) and the micromixer (m), both geometric and dynamic similarity should be achieved. Geometric similarity is satisfied when

$$\left(\frac{D_H}{L_a}\right)_s = \left(\frac{D_H}{L_a}\right)_m, \ \left(\frac{W}{L_a}\right)_s = \left(\frac{W}{L_a}\right)_m, \ \left(\frac{H}{L_a}\right)_s = \left(\frac{H}{L_a}\right)_m \tag{3.1}$$

where W and H represent the width and height of channels, respectively.

Mass-diffusion and mass-convection are responsible for the majority of mixing. Hence, velocity and concentration are significant parameters in micromixer investigations. Two dimensionless parameters are applied to assess the dynamic similarity: the Reynolds number and the Péclet number. The Reynolds number, defined as a ratio of inertia forces to viscous forces, is used to estimate the fluid characteristics in channels. The Péclet number, defined as the ratio of convective mass transfer to diffusive mass transfer, is utilized to assess the mixing process.

In order to maintain the same fluid characteristics, the following should be conserved between the scaled-up mixer and the micromixer:

$$(Re)_m = (Re)_s \tag{3.2}$$

Equation (3.2) can be presented as

$$\left(\frac{\rho U D_H}{\mu}\right)_m = \left(\frac{\rho U D_H}{\mu}\right)_s \tag{3.3}$$

If the physical properties of working fluids (density, viscosity and diffusion coefficient) are the same in both the scaled-up mixer and micromixer, equation (3.3) can be developed as:

$$(UD_H)_m = (UD_H)_s \tag{3.4}$$

Dividing by the diffusion coefficient on both sides gives

$$\left(\frac{UD_H}{D}\right)_m = \left(\frac{UD_H}{D}\right)_s \tag{3.5}$$

Therefore, the Péclet number can be maintained if the Reynolds numbers are the same in the scaled-up mixer and micromixer. Therefore, the scaled-up mixer can be considered to correctly estimate the mixing process in the micromixer.

3.1.4 Quantitative Measurement: μ-IF

Micro Induced Fluorescence (μ-IF) is an optical technique used to measure instant whole-field concentration/temperature distributions in micro liquid flows. It is a relatively recent experimental technique, having been widely used in micro flow concentration/temperature measurements in the past five years. This method allows for practical qualitative and quantitative measurements in microchannels by acquiring fluorescence signal emitted from fluorescence dye. The whole process includes five stages: feeding, illuminating, recording, processing and analyzing flow fields. In the following sections, the μ-IF technique along with the measurement principle and experimental flow loop are introduced. Also, the implementation of μ-IF, the general operating procedure and data post-processing are discussed in upcoming sections.

3.1.4.1 Induced Fluorescence Measurement Principle

The principle is mainly dependent on the fluorescent physical property. A fluorophore is a molecule that is capable of fluorescing. In its ground state, the fluorophore molecule is in a relatively low-energy, stable configuration, and it does not fluoresce. When light from an external source hits a fluorophore molecule, the molecule

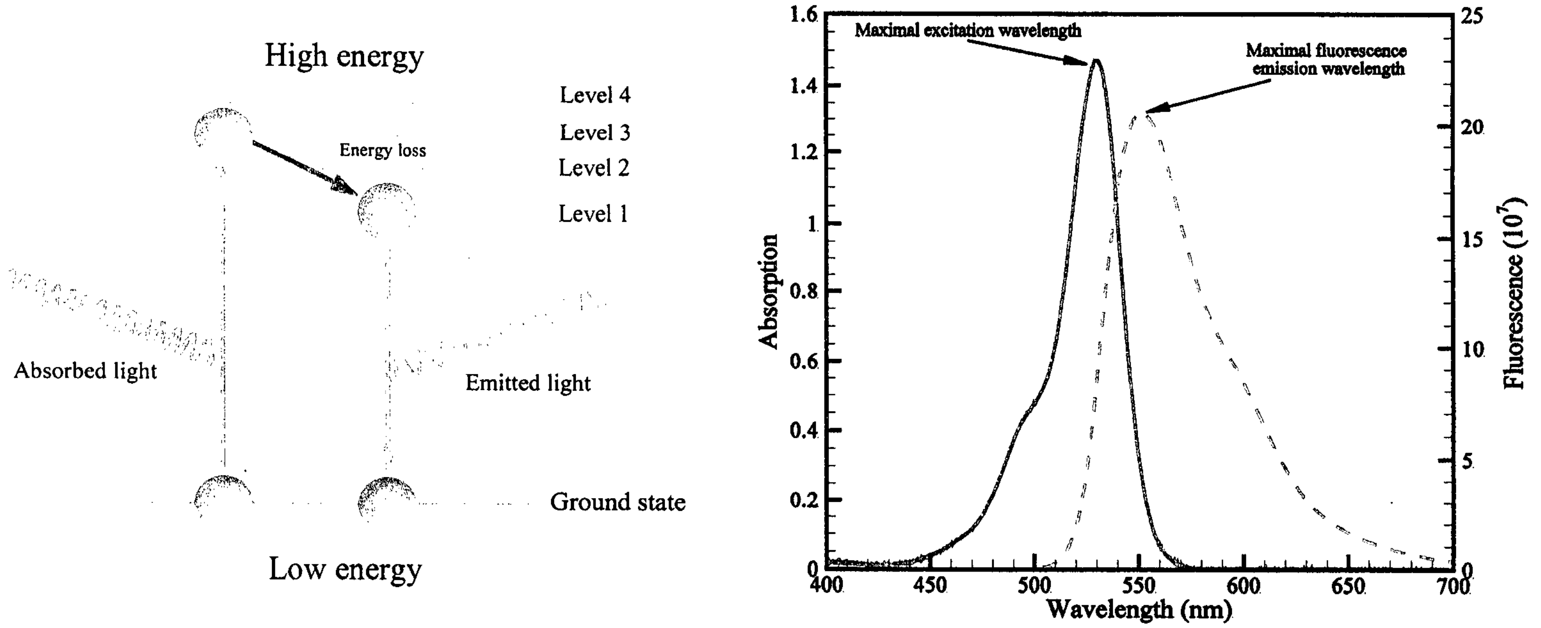

(a) Energy levels in the fluorescence process

(b) The absorption and emission spectrum

Figure 3.2: The emission principle of fluorescence and the absorption and emission spectrum.

absorbs the light energy. If the energy absorbed is sufficient, the molecule reaches a higher-energy state, called an excited state. There are multiple excited states or energy levels that the fluorophore can attain, depending on the wavelength and energy of the external light source. Since the fluorophore is unstable at high-energy configurations, it eventually adopts the lowest-energy excited state, which is semi-stable. The length of time that the fluorophore is in excited states is called the excited lifetime, which lasts for a very short time, ranging from 10^{-15} to 10^{-9} seconds. Next, the fluorophore rearranges from the semi-stable excited state back to the ground state, and the excess energy is released and emitted as light. The emitted light is of lower energy, and thus longer wavelength, than the absorbed light. This means that the color of the light that is emitted is different from the color of the light that has been absorbed. Emission of light returns the fluorophore to its ground state. The fluorophore can again absorb light energy, and repeatedly undergo the same process. The absorption and emission process is shown in Fig. 3.2a.

The number of excited fluorophore molecules is related to the wavelength of excited light. For a particular dye, some fluorophore molecules become excited if a short wavelength of light is shined on a dye solution. However, the majority of the molecules are not excited by this wavelength of light. With the increase in excitation wavelength, more molecules are excited. A certain wavelength of excitation light exits at which the proportion of excited molecules is maximal. At wavelengths longer than this value, the fluorophore molecules still absorb energy and fluoresce, but again in smaller proportions. Based on the relationship between the wavelength of excitation light and the proportion of excited fluorophore molecules, a curve could be determined, as shown in Fig. 3.2b (solid line). Therefore, for each fluorescent dye, there is a specific wavelength "the excitation maximum" that most effectively induces fluorescence. Just as fluorophore molecules absorb a range of wavelengths, they also emit a range of wavelengths. There is a spectrum of energy changes associated with these emission events. A molecule may emit a different wavelength with each excitation event because of changes that can occur during the excited lifetime, but each emission will be within the range. Although the fluorophore molecules all emit the same intensity of light, the wavelengths/the colors of the emitted light are not homogeneous. Collectively, however, the population fluoresces most intensely at a certain wavelength. Based on this distribution of emission wavelengths, a curve could be given as the Fluorescence Emission Spectrum, as shown in Fig. 3.2b (dotted line).

Because of the difference in wavelengths between excited light and fluorescence, the excited light may be removed by a filter. Only fluorescence can pass through and be collected by detector. Grey images are created for concentration analysis. Based on the different grey levels, the concentration can be determined.

The analysis of IF is based on the Beer-Lambert law of absorption. Figure 3.3 shows the light path of excited light and fluorescence. The excited light intensity reaching the bottom of microchannel is assumed to be constant, and is denoted as I_0. After passing through the fluids between the bottom and focus plane, a portion of excited light is absorbed and the intensity is reduced to $I(x,h)$. Fluorescence is emitted from the dye after being illuminated by excited light, and the initial intensity is $I'(x,h)$. When the fluorescence arrives at the bottom of the channel, the intensity is lessened to $I_f(x,0)$.

Based on the Beer-Lambert law of absorption, the intensities of excited light and fluorescence at different locations could be obtained as:

$$I(x,h) = I_0 \exp[-\int_0^h (\varepsilon C(x,y) - \eta_w) dy] \tag{3.6}$$

$$I'(x,h) = I(x,h)\, \varepsilon\, C(x,h)\, \phi\, V_0 \tag{3.7}$$

$$I_f(x,0) = I'(x,h) \exp[-\int_0^h (\varepsilon' C(x,y) - \eta'_w) dy] \tag{3.8}$$

The fluorescence arriving at the bottom passes the objective lens system and is received by CCD camera. The received intensity of fluorescence is given by

$$I_f = k_1\, k_2\, \varphi\, \varepsilon\, C(x,h)\, V_0\, I_0 \exp[-\varepsilon \int_0^h C(x,y) dy - \varepsilon' \int_0^h C(x,y) dy - \eta_w h - \eta'_w h] \tag{3.9}$$

where I_f is the intensity received by CCD, I_0 is the excited light intensity, ϕ is the quantum efficiency defined as the ratio between the emitted and the absorbed energy, ε is the extinction coefficient of the dye for incident light, k_1 and k_2 are the transmission coefficients of the lens which can be considered as constant, $C(x,h)$ is the local dye concentration at $y = h$, η_w and η'_w are the molecular extinction coefficient of the ambient fluid for the excited light and fluorescence, respectively, and V_0 is the volume illuminated by excited light. Here, I_0, k_1, k_2, V_0, η_w and η'_w are considered to be constant. Due to the low concentration, the term $\exp[-\varepsilon \int_0^h C(x,y) dy - \varepsilon' \int_0^h C(x,y) dy]$ can be viewed as one. At weak extinction, ϕ and ε are constant. Through calibration, these constants can be eliminated. The intensity received by CCD is therefore only proportional to the concentration of dye:

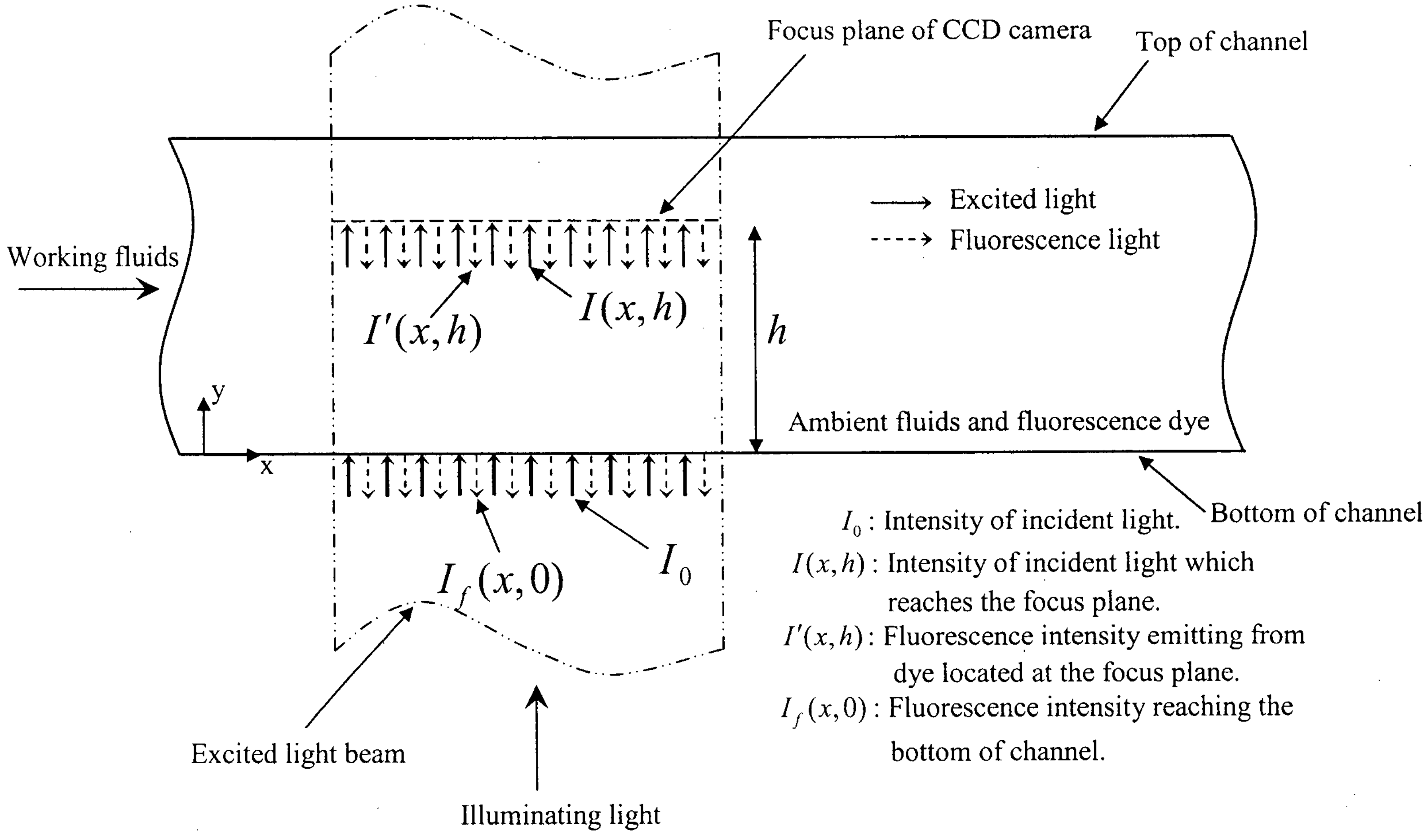

I_0 : Intensity of incident light.

$I(x,h)$: Intensity of incident light which reaches the focus plane.

$I'(x,h)$: Fluorescence intensity emitting from dye located at the focus plane.

$I_f(x,0)$: Fluorescence intensity reaching the bottom of channel.

Figure 3.3: The intensities of excited light and fluorescence along the light path.

$$I_f = B\,C(x,h) \tag{3.10}$$

$$B = k_1\ k_2\ \varphi\ \varepsilon\ V_0\ I_0\ \exp[-\varepsilon\int_0^h C(x,y)dy - \varepsilon'\int_0^h C(x,y)dy - \eta_w h - \eta'_w h] \tag{3.11}$$

The coefficient B is approximately constant. The relationship between intensity and local concentration may be viewed as linear. Through calibration, the coefficient B can be eliminated. The local concentration is obtained through fluorescence intensity as:

$$\frac{I_f}{I_{ref}} = \frac{C(x,y)}{C_{ref}} \tag{3.12}$$

where I_{ref} is the reference fluorescence intensity; C_{ref} is the reference concentration. Both I_{ref} and C_{ref} are obtained through the calibration curve.

The μ-IF technique applies the same method as conventional IF concentration measurements. The concentration is judged from the fluorescence intensity. However, conventional IF illuminates a single measurement plane with a thickness of 1-3 mm, and μ-IF illuminates the entire volume of the test section. Illuminating the entire volume is necessary at the microscale since the formation, alignment, and orientation of a very thin light sheet would be extremely difficult. Due to this "volume illumination", all fluorescence dyes in the flow field are illuminated (not just those in the signal plane) and will contribute to the resulting images. The fluorescence signals over the microchannel depth will be received by the detector.

3.1.4.2 Experimental Facilities

The experimental flow loop with a schematic of the μ-IF system used in the present investigation is shown in Fig. 3.4. The flow loop consists of test-section and two syringe pumps, which are used to independently supply the two working fluids. The μ-IF system was purchased from Dantec Dynamics, and includes image acquisition and post-processing. The primary components, associated with the μ-IF system, are a mercury lamp, an inverted epi-fluorescent microscope, a CCD camera, a Synchronization Unit, and a Dell Precision Workstation equipped with specialized computer software (FlowManager v4.50) to control flow field acquisition and processing.

Flow loop: includes the test-section and two syringe pumps. The syringe pump (New Era Pump Systems model NE-1010) is programmed for the desired flowrates and syringe diameter. Prior to operation, the working fluid is prepared by mixing the fluorescence dye with distilled water at predetermined concentrations. Syringes with a capacity of 60 ml are manufactured by BD Company. The maximum rate of pushing speed is 7635 ml/hr and the minimum rate is 58.26 μl/hr. The dispensing accuracy is ± 1%.

Fluorescence dye: Rhodamine 6G is used as a fluorescence media and can be considered to be optimal since it has a small overlap between the absorption and emission spectra, low temperature sensitivity, and relatively high quantum efficiency in order to provide a high signal to noise ratio. The currently used fluorescence dye, produced by SIGMA-ALDRICH Company, has an optimal excitation/emission wavelength of 530/560 nm. The fluorescence intensity has a linear relationship with concentrations in a certain range. Beyond this range, the relationship between the concentration and fluorescence intensity is no longer linear. Hence, the predetermined concentrations of fluorescence dye should be within the linear range. Also, the concentration of fluorescence dye is as large as possible in order to obtain a strong fluorescence signal which may reduce the effect of noise.

Excited light: 100W Hg lamp with a lamp house (Nikon LH-M100C-1), connected to a power supply of Mercury-100W (CHIU TECHNICAL Corporation), supplies continuous light with 510-560 nm wavelength which is closed to the maximal excited wavelength. Standard bulbs used by the microscope are USHIO USH-102DH. The continuous light has lower energy than the pulsed laser, which could avoid the photobleaching effect.

Inverted epi-fluorescence microscope: This microscope (Nikon Eclipse TE2000-S) combines a series of mirrors to guide a light beam to illuminate the entire fluid volume. The test section is securely fixed to the stage of the inverted microscope, below which the objectives are located. The stage is a horizontal table, capable of fine movements in both the streamwise and spanwise directions. The objectives (of magnification 2X, 4X, 10X, 20X, 40X, and 60X) are all mounted on a turret below the stage, for simplicity in changing from one magnification to another. The "Bino" mode is applied to obtain the fluorescence over the channel depth.

Filter cube: the light, which is ready to be received by CCD camera, consists of excited light scattered from the solution, walls, and fluorescence. Here, excited light is considered as a "noise source". The filter cube (Chroma Technology) is configured for excitation with green excited light (band pass at 535 nm, band width of 50 nm) and fluorescence emission in the orange part of the spectrum (band pass at 610 nm, band width of 75 nm). The filter cube also contains a dichoric mirror which ensures the efficient transfer of excited light to the test section while providing transmission of the fluorescence signal to detect, as well as reduce, noise.

Photo detector: HiSense MkII CCD camera (Hamamatsu Photonics) is mounted to the side of the microscope. It is used to capture fluorescence signals with fast speed and high resolution. The different grey levels of images in each pixel are caused by the variable fluorescence intensity. The size of the image taken by the CCD camera is 1344 x 1024 pixels. The microscope image is delivered to the camera through a camera adapter (1X magnification). The camera operation is controlled by the computer.

Image post-processing: a Dell Precision Workstation, equipped with two 3.60 GHz Intel Xeon processors, 4 GB of RAM, two 250 GB 7200 RPM hard disks, and a 128 MB video card, is used to record images, analyze and generate the concentration distribution map. A National Instruments NI-IMAQ PCI-1426 frame grabber card, which is used in conjunction with the camera to record the images, is installed at the workstation.

3.1.4.3 Experimental Procedure

Working principle:

Two working fluids are used for μ-IF experiment. One is pure DI-water, and the other is a mixture of DI-water and fluorescence dye. The μ-IF experiment is achieved based on an inverted epi-fluorescence microscope, incorporating both coarse and fine focus knobs. An epi-fluorescence filter cube is equipped inside. After passing through a beam expander, continuous light at a wavelength of 532 nm, as excited light, illuminates a volume of working fluids directed by the epi-fluorescence filter cube. The fluorescence dye emits fluorescent light at a wavelength of about 612 nm after excited by the excited light. A portion of excited light, scattered and reflected by the mixture of dye and water, and fluorescence emitted from dye pass through the filter cube. Only orange fluorescence light with a 610 nm wavelength can be transmitted, while scattered excited light (noise) is

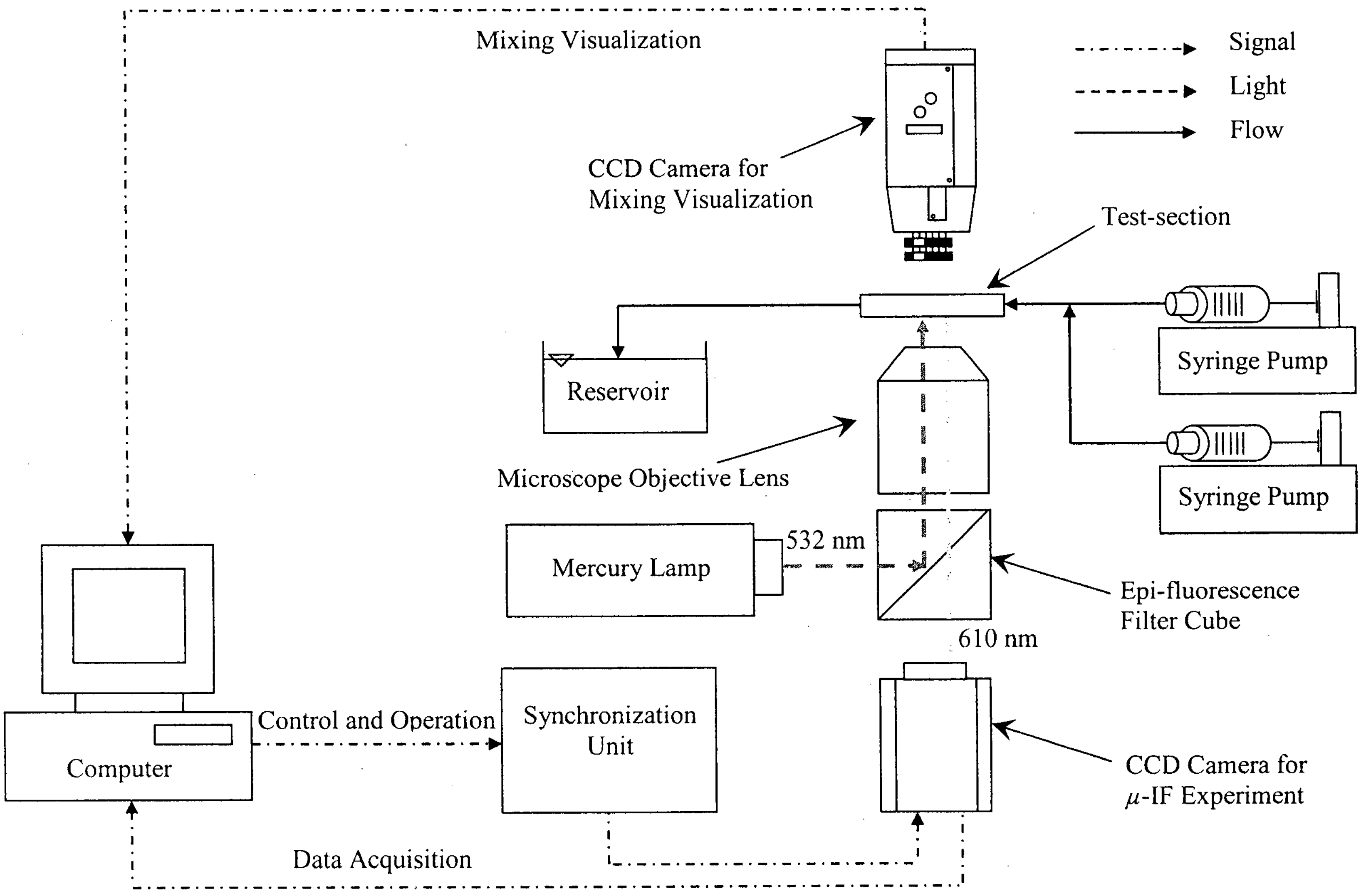

Figure 3.4: Experimental facilities for μ-IF measurement.

filtered out. The CCD camera captures the fluorescence, records fluorescence intensity, and transmits the images to the computer workstation equipped with FlowManager software for post-processing, as shown in Fig. 3.4.

General Procedure:

The general operating procedure of the μ-IF system is as follows: 1–Make six solutions with different concentrations for the calibration before experiment; 2–Position the test section on the microscope stage, with the appropriate microscope objective, to adequately visualize the location of interest; 3–Fix the focus plane at the center of the microchannels through the use of coarse and fine knobs; 4–Turn off lights in the room and switch on the mercury lamp. Wait until the lamp intensity becomes uniform and stable; 5–Individually introduce the six mixtures of water and dye with different concentrations into the test section with a syringe pump; 6–Take ten images at each concentration and calculate the average image using FlowManager software; 7–Select the six average images individually obtained at each concentration to generate the calibration curve; 8–Change the upper limit of concentration to acquire the linear calibration curve. The selected upper limit of concentration will be used in the following experiment; 9–Connect the two syringe pumps with two inlets. One syringe is filled with distilled water while the other is filled with the mixture with concentrations determined in the previous step; 10–Set the diameters of syringe and volume rate; 11–With the syringe pumps steadily operating in the pumping mode, record one hundred images in one setup; 12–Analyze resulting images and obtain concentration distributions for each setup based on the calibration curve using FlowManager software.

Calibration:

Calibration is used to determine the linear range between fluorescence intensity and concentration. Before μ-IF measurements begin, six solutions with different concentrations are made to determine the proper concentration of fluorescence dye at which the relationship between concentration and fluorescence intensity is approximately linear. The concentrations of these solutions are 0 μg/L, 100 μg/L, 200 μg/L, 300 μg/L, 400 μg/L and 500 μg/L. During the calibration procedure, the outlet is blocked by one syringe. The mixture of DI-water and dye with different concentrations is individually pushed from inlet 1 to inlet 2 by a syringe pump. By doing this, the photobleaching effect can be avoided since the working fluid keeps flowing in the microchannel. The focus plane is fixed at the center of microchannel near inlet 1. Ten images at each concentration are taken and the average is calculated to create a calibration curve. Figure 3.5 shows calibration curve between the concentration and fluorescence intensity. In the range of concentrations from 0 to 500 μg/L, the relationship is almost linear. The concentrations of the two working fluids at the inlets are selected as 500 μg/L and 0 μg/L in order to obtain a relatively strong fluorescence signal.

Experiment:

During the experiment, the objective lens is maintained at the same position used in the calibration in order to maintain same experimental conditions. The interval time between two captured images is set to 0.05 s. One hundred images are taken at each concentration and the average image is obtained. The situation is considered to be steady-state. The objective lens with 2X magnification (Nikon Corp. Plan UW 2×/0.06) is selected in order to obtain good mixing visualization and concentration measurements.

Data processing:

The size of images captured by CCD is 1344 × 1024 pixels and the resolution is 3.41 μm/pixel. The re-sampling process is done by 5 × 5 pixels in order to obtain local intensity and eliminate random noise. The final size of images is 268 × 204 pixels and the final resolution of images is 17.05 μm/pixel. Figure 3.6a shows the processed image obtained from μ-IF experiment at the inlet at $Re = 20$. The image is transferred from greylevel into color based on the calibration shown in Fig. 3.5. The local planar concentration distribution in the x-y plane is acquired. In order to obtain the concentration distribution at the region of interest, the measured line is selected and the concentration distribution at this line may be obtained, as shown in Fig. 3.6b. The local concentration is normalized by the maximum concentration (500 μg/L). Hence, the mixing efficiency at the exit of each cell and the outlet may be calculated by:

$$M = 1 - \sqrt{\frac{1}{N}\sum_{i=1}^{N}\left(\frac{C_i - \overline{C}}{\overline{C}}\right)^2} \tag{3.13}$$

$$\overline{C} = \frac{\sum_{i=1}^{N} C_i}{N} \tag{3.14}$$

where N is the total number of pixels between two side walls at the measured line in the experiment or the number of grids at the measured line in the simulation; C_i is the concentration at the i^{th} pixel in the experiment or the value at the i^{th} grid in the simulation along the measured line; $\overline{C}$ is the average concentration at the measured line. The value of mixing efficiency ranges from 0 (no mixing) to 1 (total mixing).

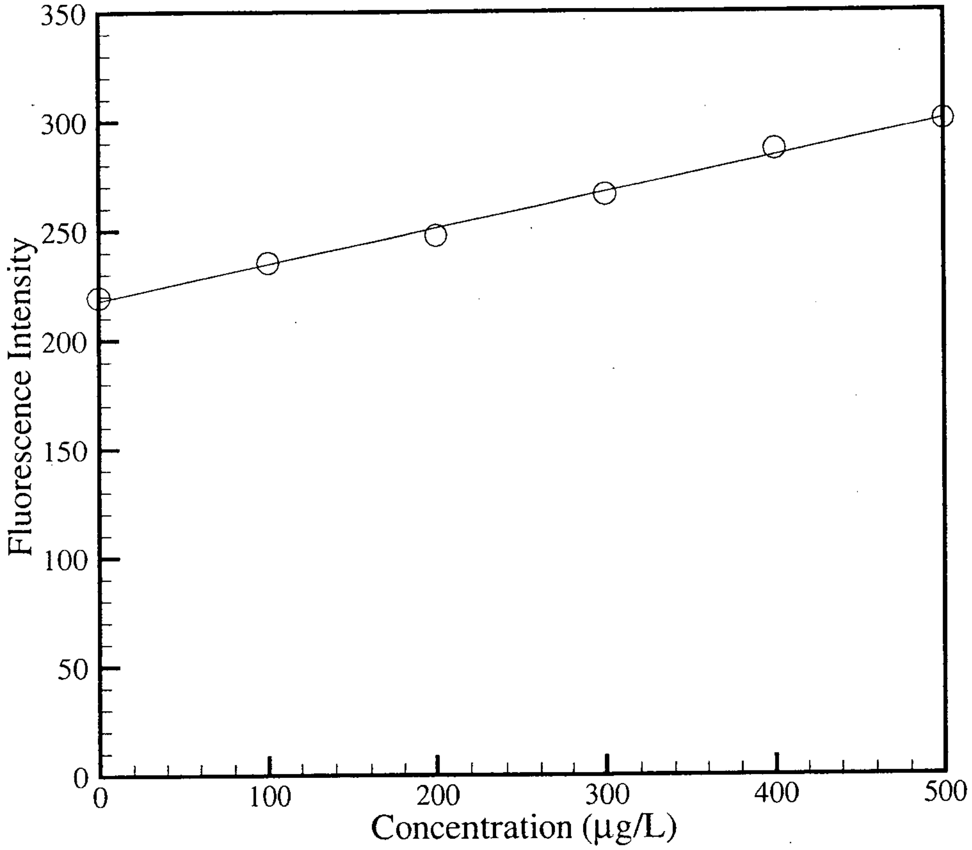

Figure 3.5: Calibration curve used for μ-IF measurement.

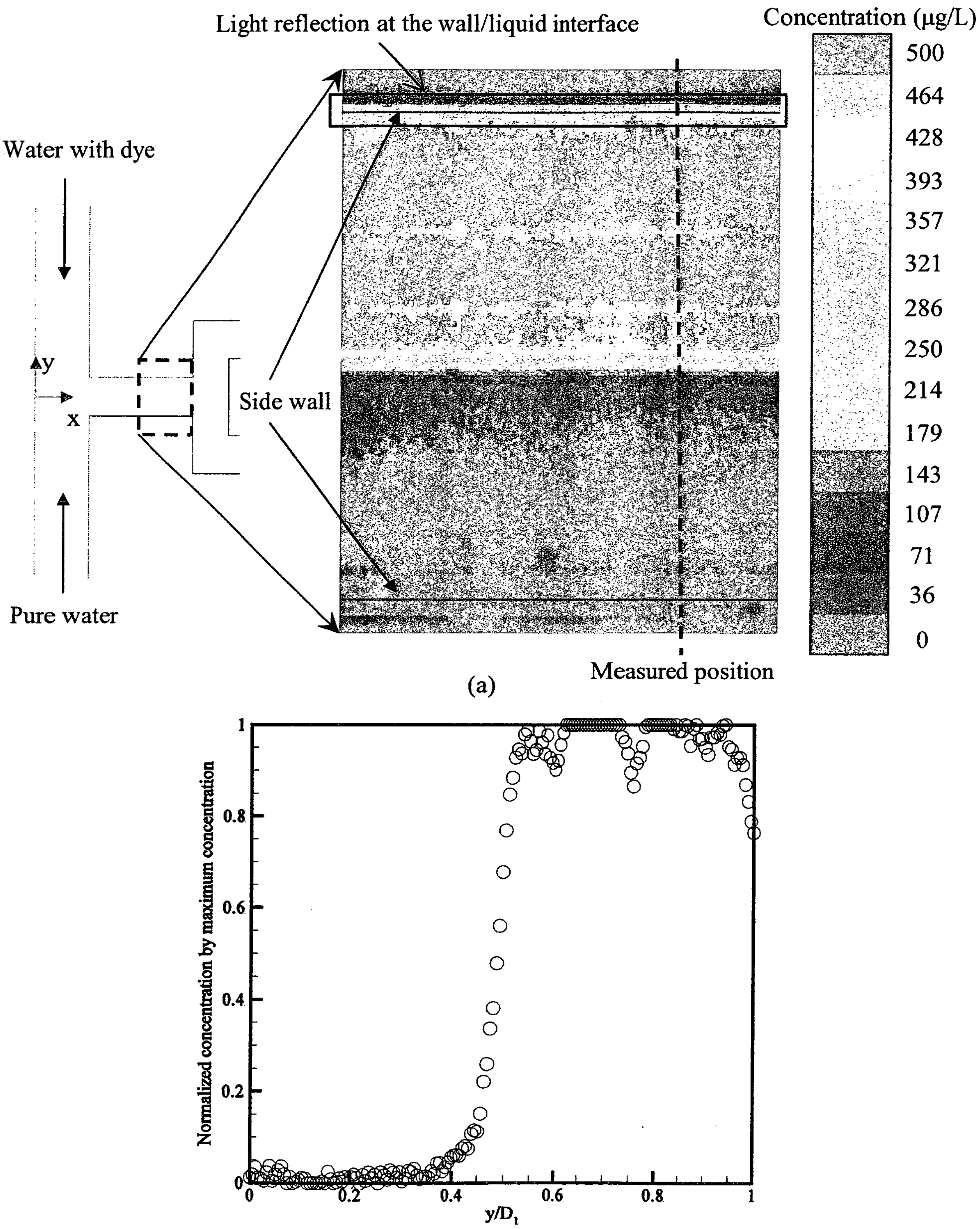

(a)

(b)

Figure 3.6: Concentration distribution obtained from μ-IF at $Re = 20$.

3.1.4.4 Experimental Challenges

The first challenge is the fabrication of test-sections. Since μ-IF technique is based on optical measurements, the requirements include cost-effective fabrication, and optically clear test sections which have the ability to function properly with the excited light emission are extremely stringent. Flat and clear test-section surfaces which reduce refractions and reflections of excited light are preferable since the light reflection at the inner walls of the microchannels induces an overestimation of mixing, as shown in Fig. 3.6a.

Fluorescence dye has strong attaching force. After μ-IF experiments, the inner surface of the test-sections will be polluted by the fluorescent dye, which will influence the next measurement. Furthermore, the overlapping of the fluorescence absorption and emission spectrum causes error in concentration measurements.

In addition, the syringe pump employs a stepper motor and worm gear, as well as a plunger-type syringe. The operating flow rates are not as accurate as expected due to the friction of the plunger and the operation of the stepper motor. Furthermore, the two syringe pumps disturb each other since the flow directions of two pumps are face-to-face.

3.1.5 Mixing Visualization

The same flow rate should be supplied to each of the two inlets so that the interfacial surface of the two working fluids is located along the symmetric plane, and the fluid acts as steady-state. Two syringe pumps (New Era Pump System NE-1010) are used to supply species to the two inlets. Although both pumps are the same model, calibration is still required to test if the two pumps are able to supply the same flow rate, so as to satisfy the experimental requirements. Mixing visualization has been conducted to determine the range of *Re* at which both pumps supply the same flow rate. The body force can be neglected as the surface tension and viscous forces are dominant at the microscale. The selection of the two working fluids is important since the body forces cannot be neglected in the scaled-up micromixer, where viscous forces and inertial forces are dominant. Two working fluids of a similar density have been selected to ensure that mixing diffusion only occurs in the y-direction when the two species merge at the entrance of the T-shaped inlet. Green and red food colors are selected as visual media. The images are taken by a 3CCD color video camera (SONY DXC-9000). The mixing process can be viewed through color variation from the top surface.

3.1.6 Results and Discussion

Figure 3.7 shows the selected positions used to analyze the mixing process in the experiment. Six positions from x-1 to x-6 are selected to investigate the effect of the cell number in μ-IF. Corners 1-5 are chosen for illuminating the species distribution. The three positions, P-1, P-2, and P-3, are used to observe the flow path in the mixing visualization. Figure 3.8 presents the pre-processed greylevel images of mixing, obtained by CCD, at the inlet and outlet of the test-section along the symmetric plane at $1 \leq Re \leq 50$ in order to qualitatively observe the mixing in the fluorescence experiment. Figure 3.8a captures images at the inlets. No mixing occurs at this position. This image could be used as a reference to judge the mixing process of Fig. 3.8b-f, based on the greylevel image. Mixing may be completed well at $Re = 1$, judging by the light intensity at the outlet as shown in Fig. 3.8b, although the interface could not be clearly distinguished. When *Re* reaches 5, the mixing efficiency decreases, as shown in Fig. 3.8c, and the interface is clearly visible. Mixing efficiency keeps decreasing at $Re = 10$ as shown in Fig.

3.8d. The greylevel difference between black and white is more apparent than at *Re* = 5. This is a result of reduced residual time. The working fluids do not have adequate time to mix well before they flow out of the test-section. The mixing efficiency improves, however, at $Re \geq 10$ due to the change of mixing mechanisms from mass-diffusion to a combination of mass-diffusion and mass-convection. The combined mixing mechanism increases the mixing although the residual time is reduced as *Re* increases. The greylevel difference tends to be smaller from *Re* = 20 to 50, as shown in Fig. 3.8e and 3.8f. In order to quantitatively estimate the mixing, the post-processing of images obtained from the fluorescence experiment is carried out by FlowManage V4.5. The details have been introduced in data processing section.

The fluctuations of single or multi-syringe pumps have been proposed (Angele et al., 2006; Vanapalli et al., 2007; Ribeiro et al., 2008). In the present study, one hundred images are taken in five seconds at the entrance of the first cell at $1 \leq Re \leq 50$. The average image at each *Re* is calculated and the concentration distribution is obtained through the calibration curve. Pump 1 is first connected to inlet 1, which is denoted as Pump 1_Inlet 1. Pump 1 is then switched to connect with inlet 2, which is denoted as Pump1_Inlet 2. At *Re* = 5, 10, 20 and 50, the concentration distributions of Pump 1_inlet 1 and Pump 1_inelt 2 are almost the same. The interface is located at the same position. This concludes that the two pumps supply the same average flow rate within the tested time. A difference occurs, however, at *Re* = 1. The two pumps are no longer able to supply the same average flow rate within the tested time. In order to obtain measurements at *Re* = 1, multiple repeated measurements are taken and the assessment of images obtained from the experiments are performed at the exit of the first cell since

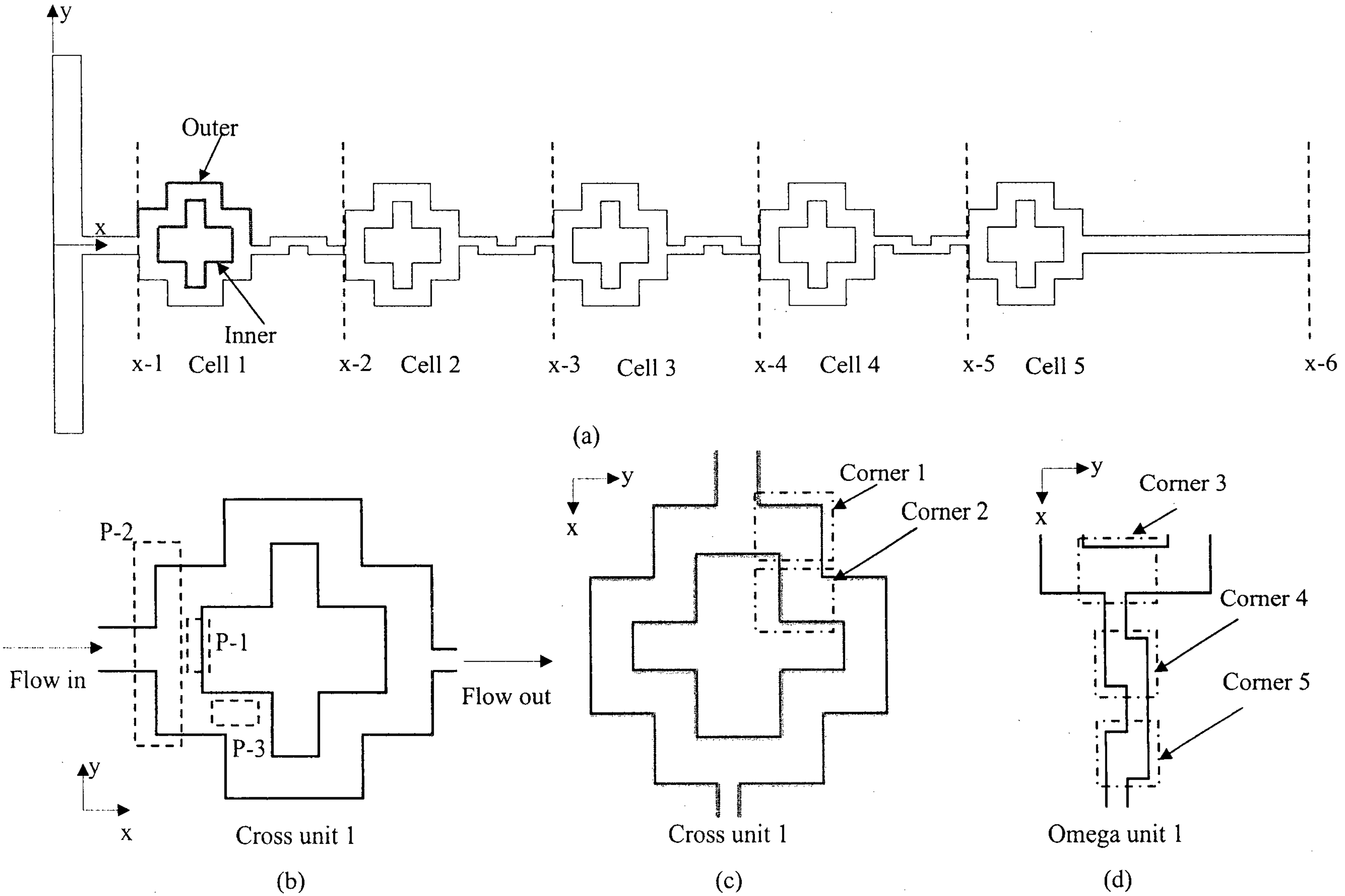

Figure 3.7: Positions used for mixing investigation in the present design.

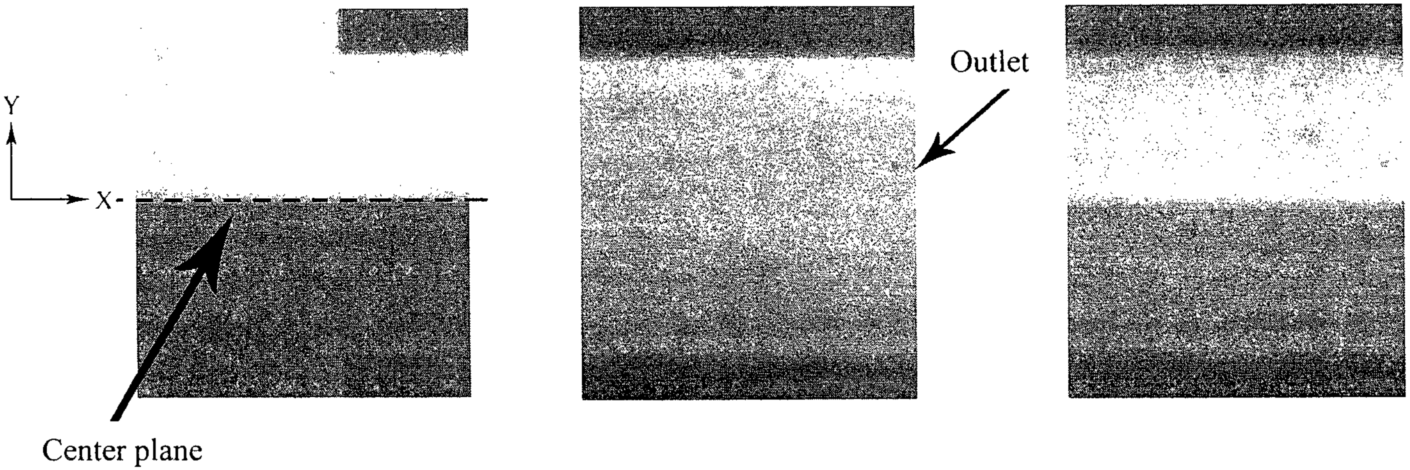

(a) The inlet at *Re* = 1 (b) The outlet *Re* = 1 (c) The outlet at *Re* = 5

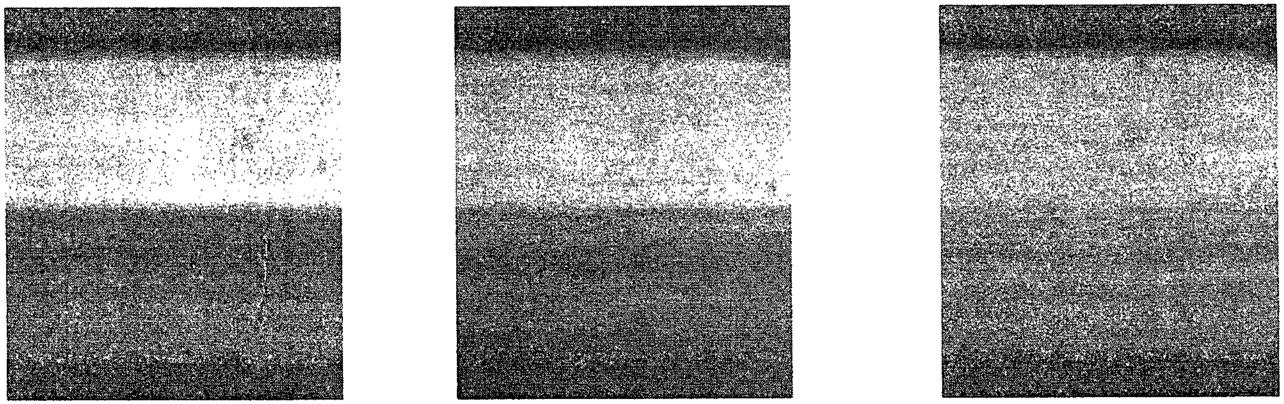

(d) The outlet at *Re* = 10 (e) The outlet at *Re* = 20 (f) The outlet at *Re* = 50

Figure 3.8: The pre-processed images obtained from μ-LF experiment.

the interface could be observed clearly. The images acquired from the multiple repeated measurements, where the interface is located at the center plane, are selected and the average image is obtained to investigate the mixing. Therefore, the mixing measurements are taken over the valid range $5 \leq Re \leq 50$ at the outlet, and $1 \leq Re \leq 50$ at the exit of the first cell, which is used for the validation of numerical simulation.

Figure 3.9 shows the mixing process at corner 1 and corner 2 obtained by fluorescence measurement. At $Re = 20$, the mixed fluid is close to the outer wall at corner 1. When Re reaches 50, all mixed fluid is located at the corner, and unmixed fluid lies at the inner side. Furthermore, the mixing of the species at the same corner is more sufficient than at $Re = 20$. Also, the concentration distribution at $Re = 50$ is more obvious. At corner 2, the mixed fluid moves to the inner side and the unmixed fluid is located at the outer side at $Re = 20$ and 50. At $Re = 20$, almost no fluid is at the corner. However, the corner is filled with the mixed species at $Re = 50$. In order to understand this phenomenon, a simulation is conducted to assist in the analysis. Figure 3.10 shows the streamlines in half of the first cell at $Re = 50$. The fluid located at the center of the channel has the highest velocity, which produces maximum centrifugal force. This force drives the fluid with green color towards the inner side after entering the cross unit, as shown at P-2. The fluid with the blue color located at the inner side is compressed and moves to the outer side along the top surface, as shown at P-2. The movement of the fluid becomes stronger as Re increases. This phenomenon shows good correlation with the experimental results shown in Fig. 3.9. The fluid with blue color is located at the center plane in the straight channel before entering the cross unit, such that this part of fluid is mixed. It moves to corner 1 due to compression, and causes mixing of the species at

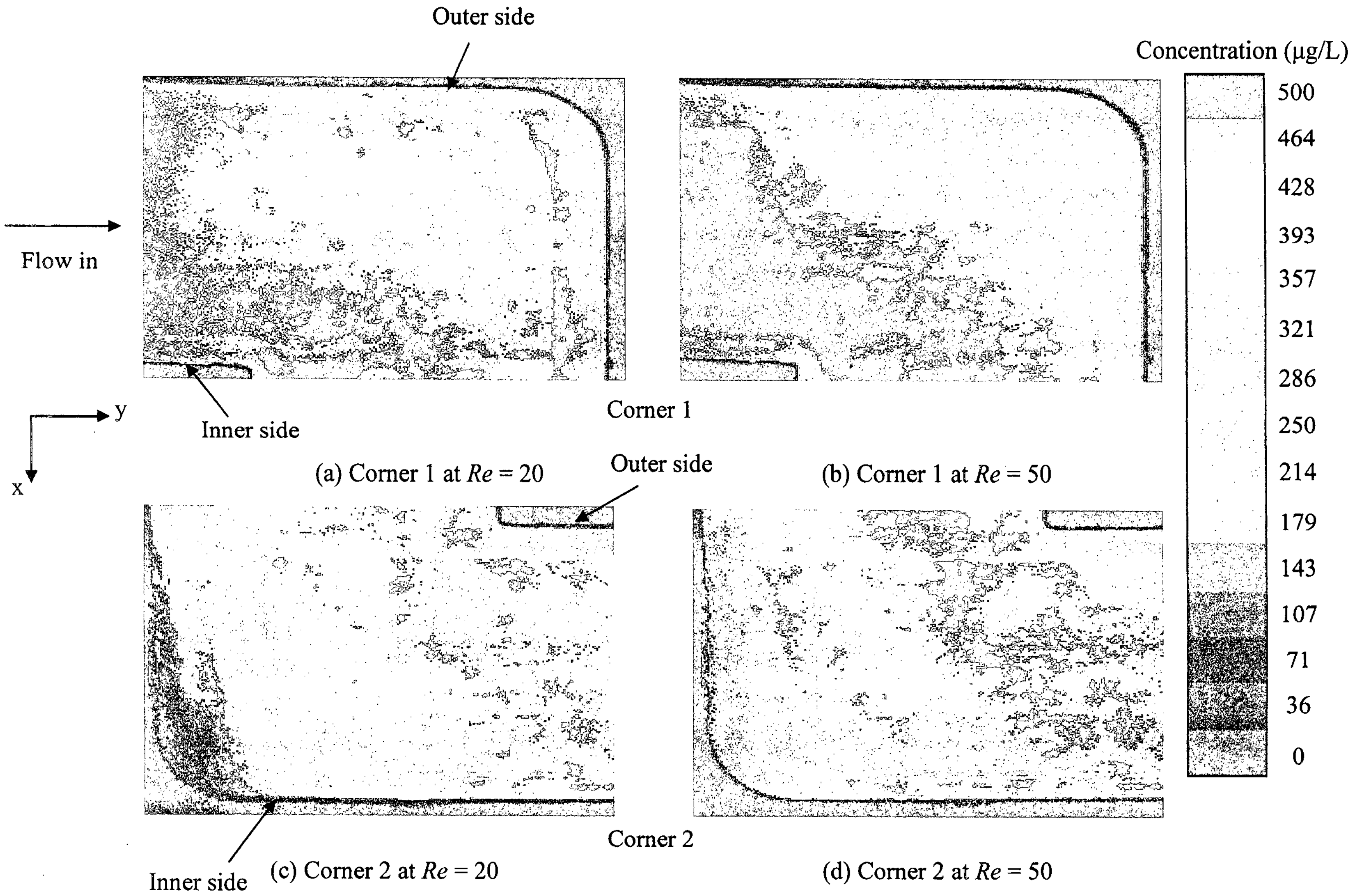

(a) Corner 1 at *Re* = 20

(b) Corner 1 at *Re* = 50

(c) Corner 2 at *Re* = 20

(d) Corner 2 at *Re* = 50

Figure 3.9: Mixing images obtained by μ-IF at corner 1 and corner 2.

corner 1, as shown in Fig. 3.9. When the blue color fluid moves from the inner side to the outer side along the top surface, the overlap of fluids occurs, which increases the contact area. Also, recirculation flow at the corners is generated and enhances mass-convection. At *Re* = 50, the inertial force is much larger than the viscous force. A part of the fluid separates from the main fluid, and a vortex is generated at the corner leading to accelerated mixing. Figure 3.11 presents the mixing efficiency in the symmetric plane at six positions from x-1 to x-6, as shown in Fig. 3.7. At x-1, the mixing efficiency decreases as *Re* increases from 10 to 50 in the straight channel, as an increase in *Re* results in a decreased diffusion time. The mixing efficiency increases faster at higher *Re* in the first mixing cell as the effects of the fluid overlap and flow recirculation are enhanced as *Re* increases. Among the tested *Re,* the mixing efficiency is highest at *Re* = 50. After five cells, the best mixing efficiency, 61%, appears at *Re* = 50, and the worst mixing efficiency is 34% at *Re* = 10.

Figure 3.12 shows the mixing efficiency of several passive planar micromixers presented in the past five years. The present micromixer has better mixing efficiency than most designs for $5 \leq Re \leq 50$. The mixing efficiency of the presented design, calculated at the outlet, decreases as *Re* increases at $Re \leq 10$, since the residual time is reduced. The species do not have adequate time to achieve good mixing. The mixing efficiency increases, however, as *Re* increases at $Re \geq 10$ due to the change in the mixing mechanism. The mixing mechanism changes from mass-diffusion to the combined mechanisms of mass-diffusion and mass-advection.

In order to investigate the mixing process in the entire mixer, mixing visualization is applied. Figure 3.13 shows the mixing visualization where green and red food colors are

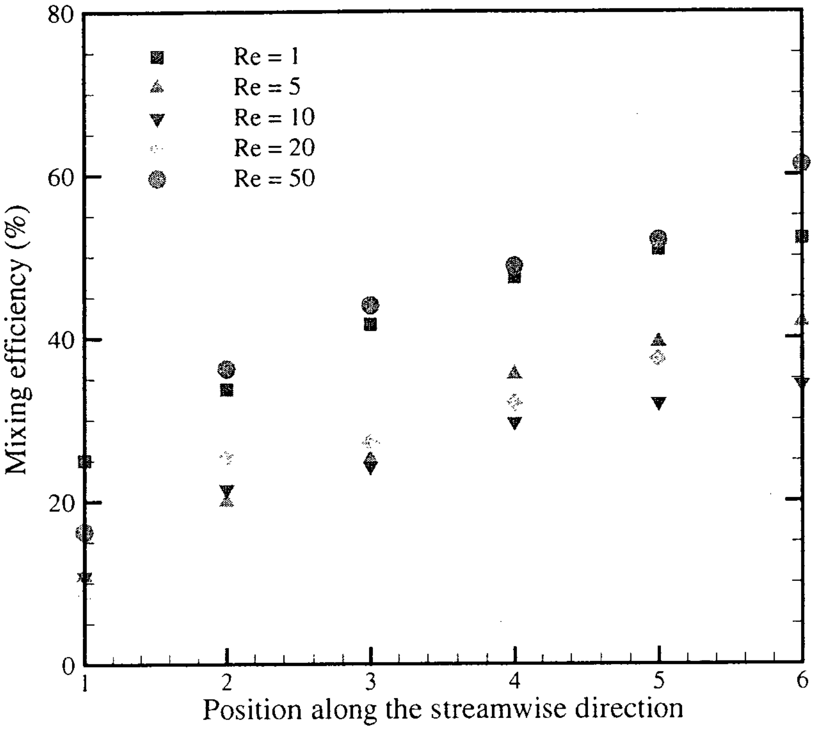

Figure 3.11: Mixing efficiency at six positions along the x direction.

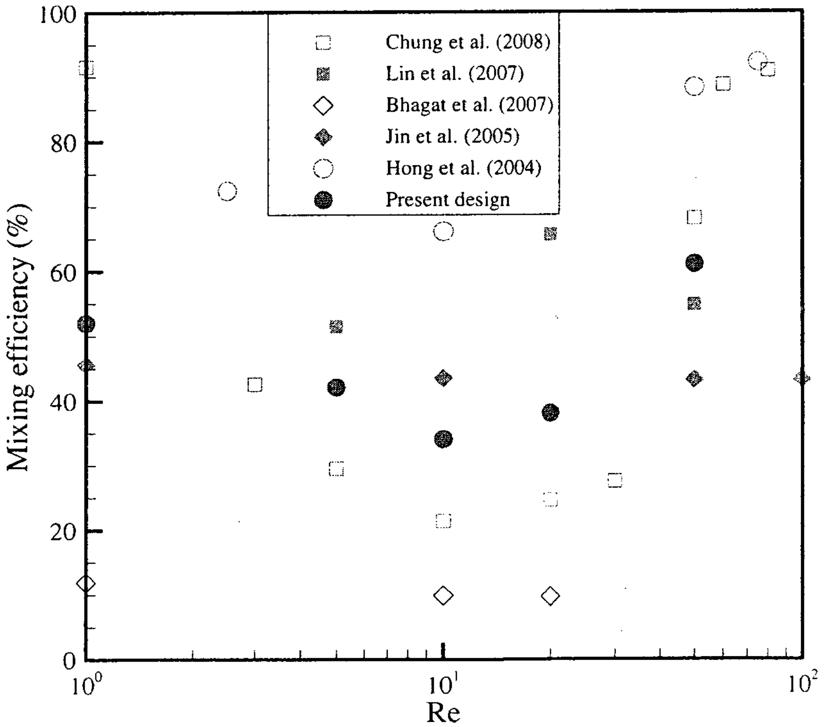

Figure 3.12: Mixing efficiency at the outlet at $1 \leq Re \leq 50$.

applied. The mixing process is judged based on the color brightness. Complete mixing corresponds to the black color. At *Re* = 1, the two species start to mix at the center plane as shown at area-1. Mixing is enhanced due to the diverging effect at the entrance of the first cross unit, as shown at area-2. At the exit of first cross unit, the colors at the upper and lower parts at the exit of the first cell become darker than at area-1. After four cells, the color becomes almost black. The interface between the two species cannot be clearly distinguished at the outlet. When *Re* reaches 10, the color variation is not obvious, which represents insufficient mixing process along the entire flow domain. Since an increased *Re* leads to a shortened residual time of working fluids in the channels, the working fluids do not have enough diffusion time to obtain adequate mixing. The mixing efficiency decreases at *Re* = 10, which corresponds to the results obtained from quantitative measurements. Mixing is completed very well at *Re* = 60. After three cells, the interface of the two working fluids is hardly observed. There are two areas which require attention. At area-3, the interface is twisted near the outer wall. Vortices can be seen at this location. At area-4, two species appear in each branch of the cross unit. In order to obtain clearer images to estimate this phenomenon, the position of the entrance of the first cell is focused on. At P1, nine pictures are taken within one second to see the variation of the interface at *Re* = 50, as shown in Fig. 3.14. From this figure, one can observe the oscillation of the interface from t = 0.1 s to 0.9 s. A similar phenomenon is also observed at *Re* = 1, 5, 10 and 20. The mixing visualization results show that the oscillation occurs over the entire tested range of *Re*. The oscillation frequency and amplitude increase with increasing *Re*. The two syringe pumps are no longer able to supply same pressure to the two inlets. Oscillation of the interface leads to uneven species distributions in the cross units. The unstable oscillation is probably caused by the pump working principle. It has a good agreement with the fluorescence measurements. Figure 3.15 shows the mixing visualization of P-2 & P-3 at *Re* = 20 and 50. As seen in these two pictures, a portion of the red species enters the green species domain, as shown at P-3, caused by the oscillation. At P-2, the dark fluid, indicating complete mixing, is monitored to obtain the flow characteristics. At *Re* = 20, this part of the black species is forced to the outer wall after entering the branch of the cross unit. This path could be observed clearly. This phenomenon is also seen at *Re* = 50, however, the path becomes indistinct and a large portion of the black fluid is created at the corner in the cross unit. The mixing visualization is in accordance with fluorescence experimental results.

3.2 Numerical Investigation

3.2.1 Computational Models

Numerical simulations are applied to assist in comprehending how fluids behave in microchannels. Since the structure of the present micromixer is symmetrical, a half model of the first cell of CO-micromixer is built and meshed in order to reduce the calculation time. The grid system of CO micromixers is shown in Fig. 3.16. Numerical diffusion plays a key role in simulation results, and was proposed by Hardt and Schonfeld (2003) who investigated an analytical model of the concentration profile in multi-lamination flow. Numerical diffusion, caused by the finite differential method, dominates diffusive mass transfer on computational grids instead of physical diffusion, especially for liquid-liquid mixing with characteristic diffusion constants on the order of 10^{-9} m^2/s. It is related to the velocity, grid size, and the scheme. Numerical diffusion in second-order upwind scheme may be expressed by:

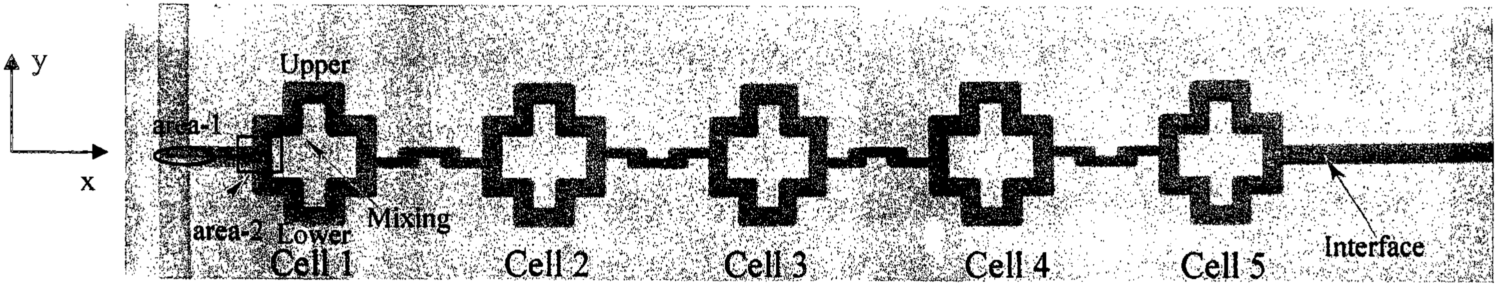

(a) $Re = 1$

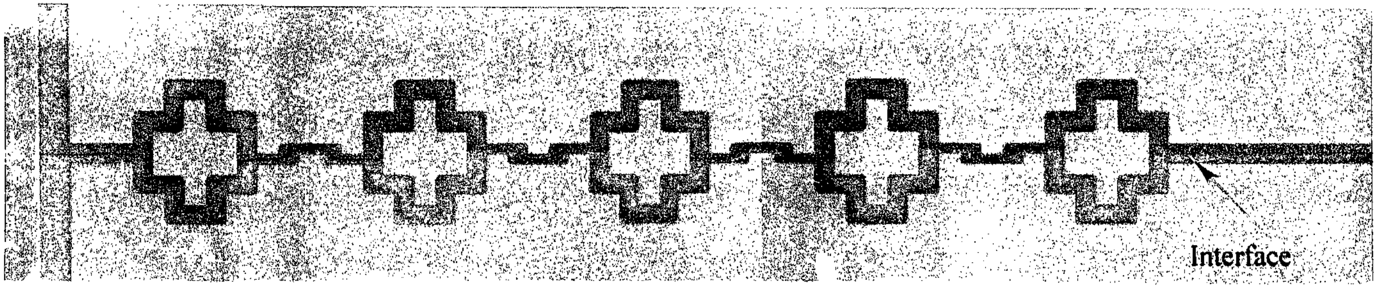

(b) $Re = 10$

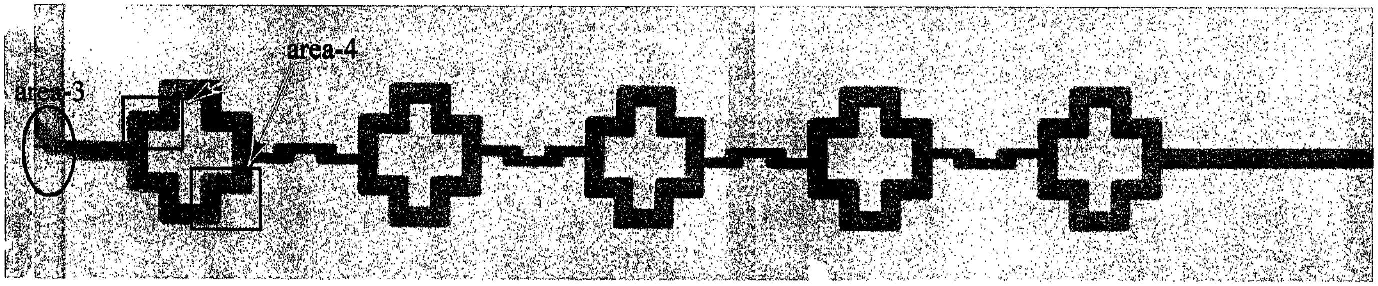

(c) $Re = 60$

Figure 3.13: Mixing visualization of the proposed mixer with five cells.

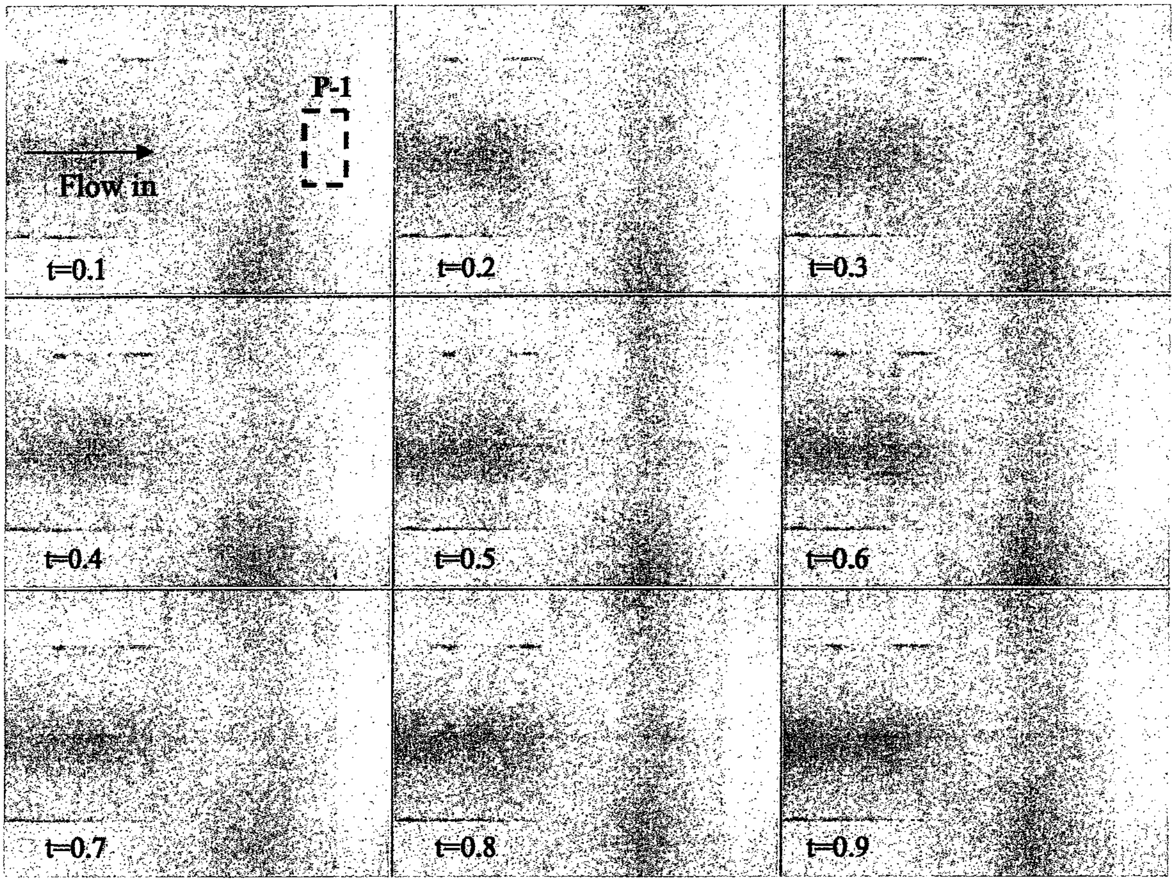

Figure 3.14: Mixing visualization at P-1 taken within one second at *Re* = 50.

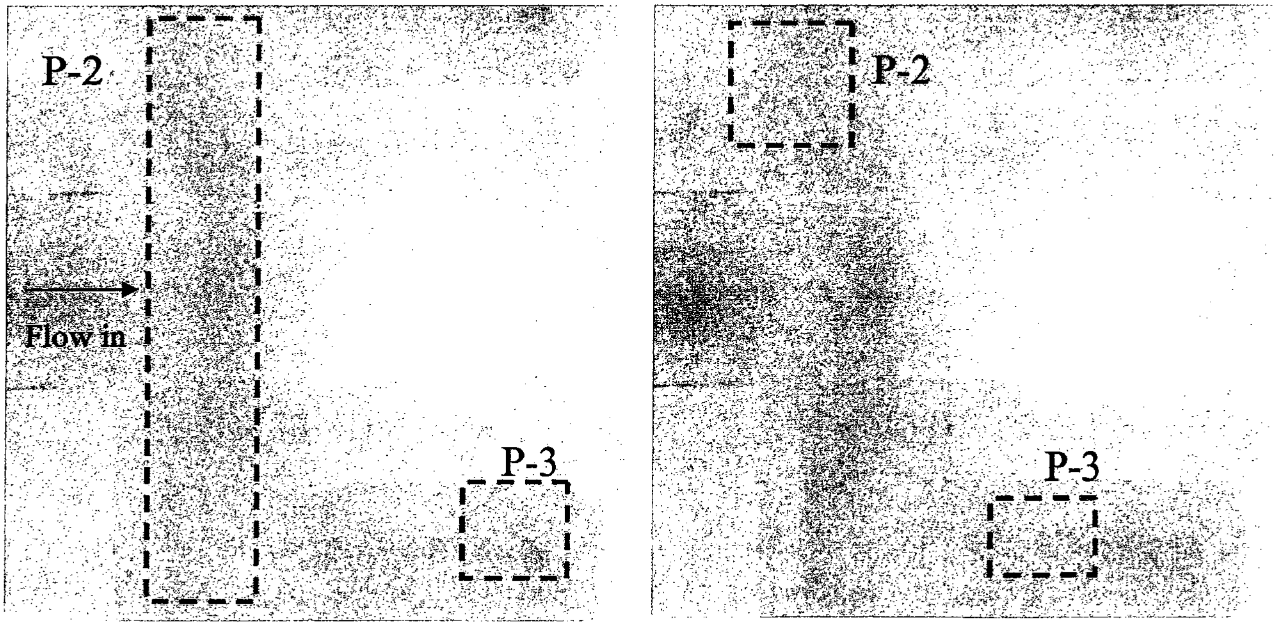

(a) *Re* = 20

(a) *Re* = 50

Figure 3.15: Mixing visualization of P-2 and P-3.

$$\Gamma = \frac{u_x \Delta x}{2} \tag{3.15}$$

Grid independence is performed in order to minimize the effect of numerical diffusion. As stated in Hardt and Schonfeld (2003), a higher scheme applied in the simulation also could reduce the effect of this parameter. Since numerical diffusion is related to the grid size, a fine mesh would be applied to the entire flowing domain, not only near the wall. Since the depth of the microchannels in the present design is constant, a 2D drawing is imported into the pre-processing software. The unstructured grid scheme is used to mesh the 2D model after defining the flow regime. The structure scheme is applied in the z-direction depending on the extension of the 2D model.

3.2.2 Numerical Simulation

Fluent® 6.3 is used as a numerical simulation tool. Some assumptions are proposed before doing numerical simulations. The flow is viewed as steady-state and incompressible. No-slip boundary conditions exist at the inner walls. According to these assumptions, the governing equations, based on the continuity equation and Navier-Stokes equation, are represented as:

$$\nabla \cdot \boldsymbol{V} = 0, \tag{3.16}$$

$$\rho \boldsymbol{V} \cdot \nabla \boldsymbol{V} = -\nabla \boldsymbol{P} + \mu \nabla^2 \boldsymbol{V}, \tag{3.17}$$

$$\boldsymbol{V} \cdot \nabla C = D \nabla^2 C \tag{3.18}$$

The Navier-Stokes equation and continuity equation can be solved to obtain velocity in case of an incompressible fluid. The velocity is substituted into the convection-

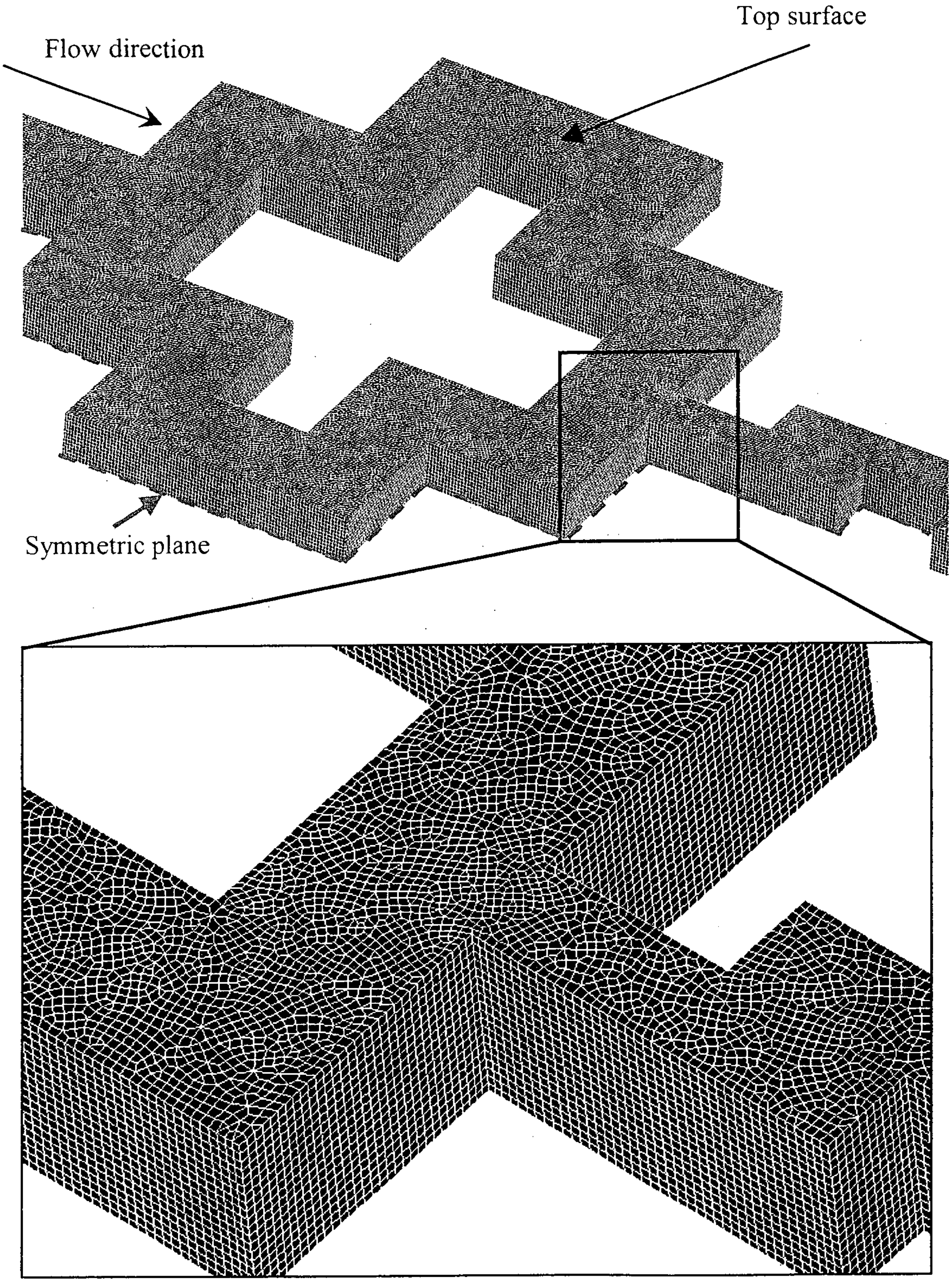

Figure 3.16: Grid system of the half model of the CO micromixer.

-diffusion equation to solve the concentration distribution. The species transport model is selected to solve this case. Two species are defined in material options. One species is defined as pure water, with density and viscosity set as 10^3 kg/m^3 and 10^{-3} kg/m·s, respectively. A new species, named "dye", is defined to mix with the pure water to simulate the experimental environment. It has same values of density and viscosity as water. The diffusion coefficient of this new species in water is fixed at 2.8×10^{-10} m^2/s for the CO-micromixer and 1×10^{-9} m^2/s for the IC and IO micromixers. Because there is no heat transfer, the energy equation is turned off. The operating pressure is fixed at 10^5 Pa. For the boundary conditions, "velocity-inlet" type is assigned to both inlets. The velocity direction is normal to the boundary. The dye concentrations of water and dye are set as 0 and 1, respectively. Ideal mixing means the concentration of dye reaches 0.5. The outlet boundary is set as "pressure-outlet". The reference pressure is fixed at zero. The "SIMPLEC" module is applied for the pressure-velocity coupling analysis of two mixing flows in microchannels. The discretization is "third-order QUICK" for velocity and species, and "second-order upwind" for pressure. The application of higher order could minimize the numerical diffusion as proposed by Hardt and Schonfeld (2003). The maximum number of iterations is set to 3000 and the convergence criterion is 10^{-5} for continuity, velocity, and species in order to obtain converging results.

3.2.3 Results and Discussion

Grid independence is performed to minimize numerical diffusion. Since the numerical diffusion is related to the velocity, the grid independence is performed at the maximum tested *Re*, which is selected as 50. Figure 3.17 shows the velocity and concentration distributions at the intersection of the symmetric plane and the exit plane of the first cell. The results show there is no obvious change in velocity and concentration as the grid number is larger than 1.6 M. Hence, the grid system of 1.6 M is selected for the further investigation.

Figures 3.18-20 show the concentration distribution based on experimental results and simulation at corners 3-5 (see Fig. 3.7). These figures show good agreement between experimental and simulation results. At corner 3, the interface is inclined to the left side on the top surface due to the asymmetric structure at *Re* = 20. At *Re* = 50, a vortex can be observed at the entrance of the omega unit. The concentration distribution becomes more complex than at *Re* = 20. The interface area is increased and the mass-convection is enhanced. At corner 4, the concentration increases from the left side to the right side at *Re* = 20. Fluids with high concentrations (> 0.5) are located on the right side and fluids with low concentrations (< 0.5) are on the left side. However, the fluids with low concentration move to the right side, and a "sandwiched" flow pattern is generated at *Re* = 50. A part of fluids with low concentration is compressed to the right side through the top of the microchannel. A Dean vortex is created at the corner. A similar phenomenon

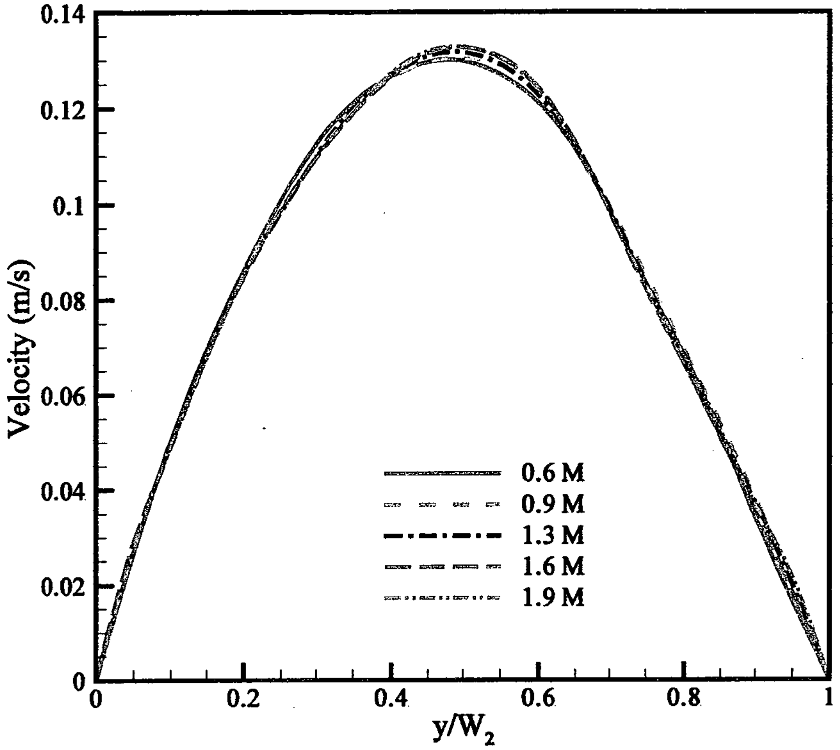

(a) Velocity

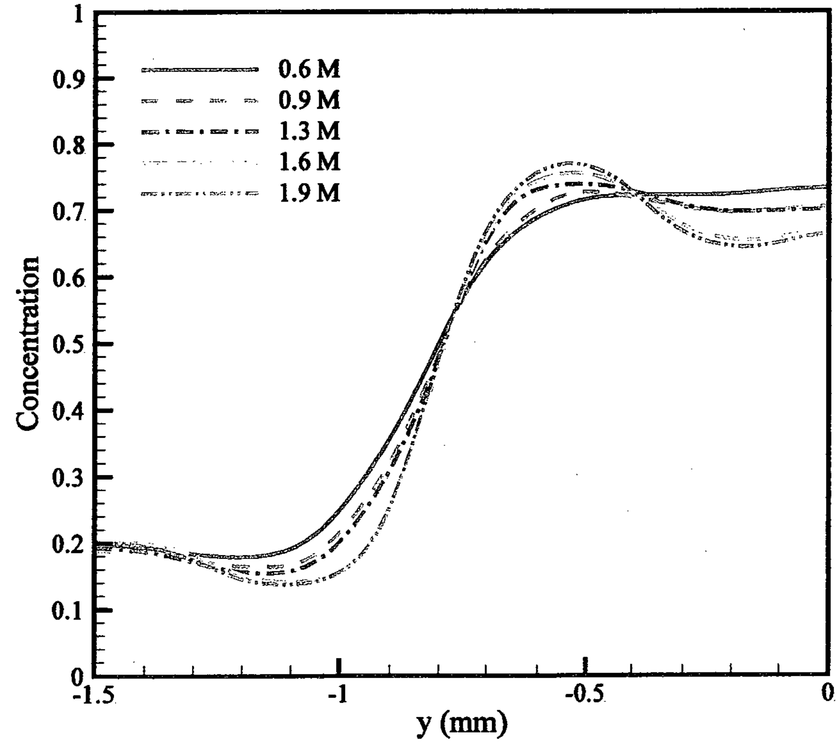

(b) Concentration

Figure 3.17: Velocity and concentration distributions at the intersection of the symmetric plane and first cell exit plane at different grid sizes.

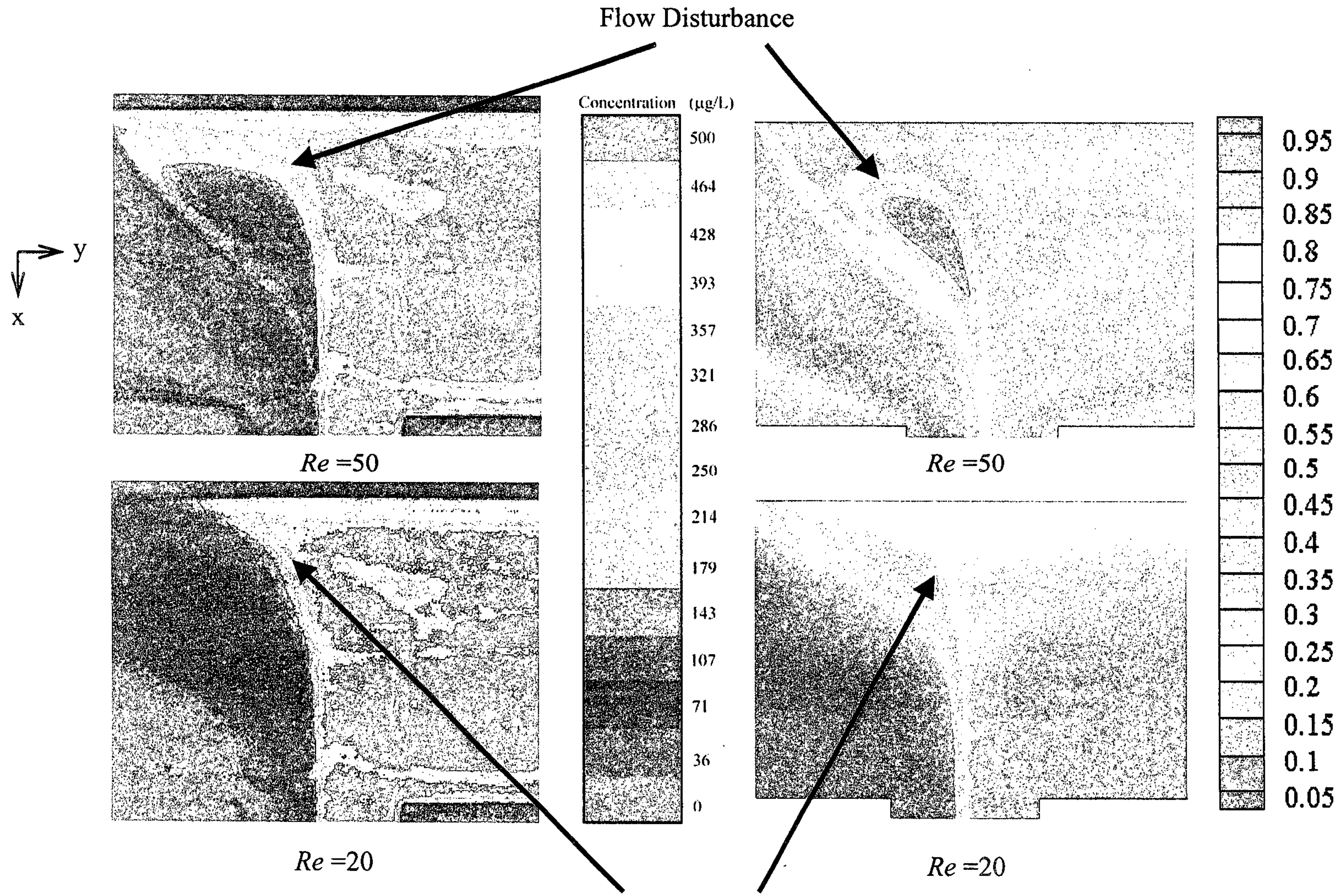

(a) Experiment (b) Simulation

Figure 3.18: Concentration distribution obtained from experiment and simulation at corner 3.

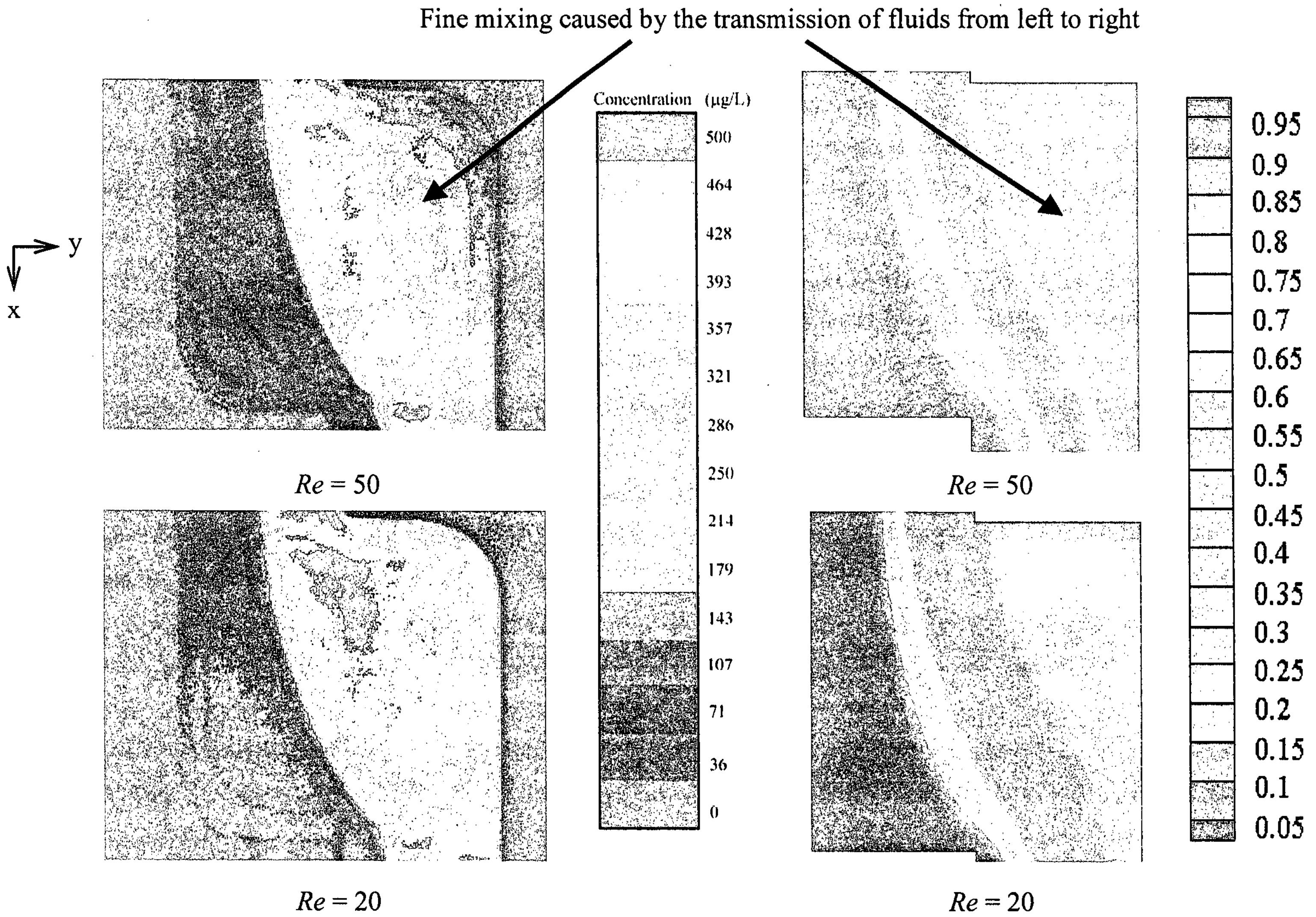

(a) Experiment (b) Simulation

Figure 3.19: Concentration distribution obtained from experiment and simulation at corner 4.

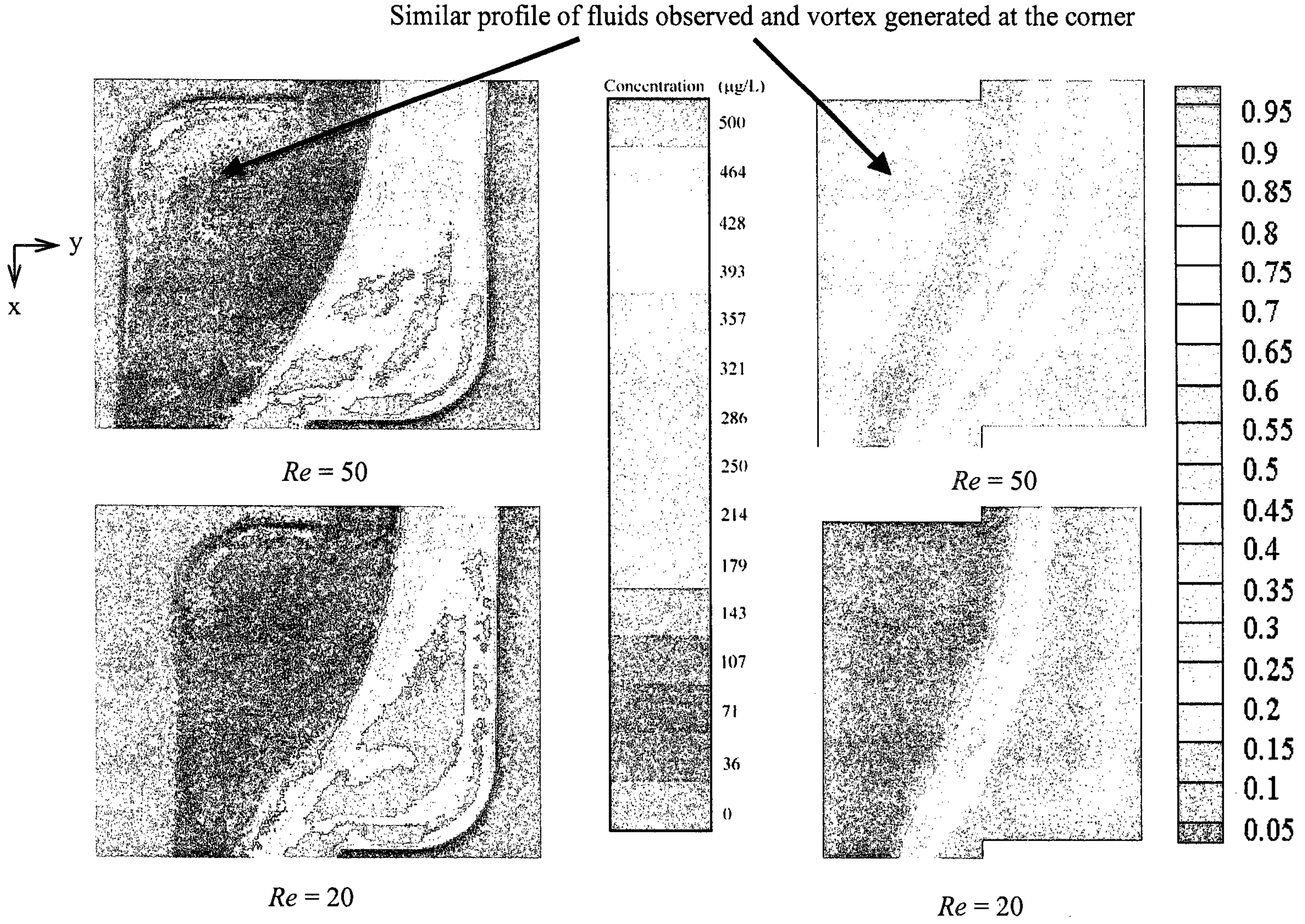

Similar profile of fluids observed and vortex generated at the corner

(a) Experiment

(b) Simulation

Figure 3.20: Concentration distribution obtained from experiment and simulation at corner 5.

could be observed at corner 5. The vortices generated at the corners are able to increase the mass-convection at *Re* = 50 compared to *Re* = 20. In order to further understand the flow patterns in the microchannels, numerical simulation results are used to display the mixing process.

Figure 3.21 shows the comparison of experiment and simulation mixing efficiency at the exit of first cell. Both results have good agreement at $1 \leq Re \leq 50$, as shown in Fig. 3.12 (a). The mixing efficiency decreases at $1 \leq Re \leq 5$ due to the reduction in diffusion time. Due to the low *Re,* the viscous force is dominant. The fluids are difficult to separate from the main flow. Mass-diffusion dominates the mixing and the mass-convection has secondary effects on mixing. The difference between experiment and simulation may be caused by the light reflection near the wall in the experiment. The light reflection leads to the appearance of good mixing near the wall, which overestimates the mixing efficiency, as shown in Fig. 3.6(a). Second, since the test-section is scaled-up, traditional manufacturing processes are applied. The wall is not smooth, which induces uneven light intensity distribution. The difference between experiment and simulation is within 20% at $1 \leq Re \leq 50$, as shown in Fig. 3.12(b). Figure 3.22 shows the iso-surface at *Re* = 5. Judging from this figure, fluids with different concentrations flow in microchannels side by side. No disturbance or recirculation flow is generated. Mixing is mainly dependent on mass-diffusion. Figure 3.24 shows the concentration distribution and velocity vector at eight cross-sections along the microchannels, as shown in Fig. 3.23. The interface remains straight at C1 and C2, and a small portion of fluids goes up and down along the center plane, which is caused by the parabolic velocity distribution. The maximum velocity is located at the symmetric plane. After the two species encounter each other at C1, the fluids with higher momentum in the symmetric plane are compressed more than others, which induces fluids to move up along the center plane. From C5 to C8, the interface fluctuates left and right when the fluids pass the corners. The fluctuation of interface enhances the Taylor dispersion, which accelerates the mixing. At the side walls, a small portion of fluids have z-velocity due to the centrifugal force. After the flow enters the corner or changes the flow direction, the fluids with higher velocity generate larger centrifugal forces, and move to the outer wall. Hence, the fluids in the symmetric plane have highest centrifugal force. After arriving at the side wall, the fluids in the symmetric plane are stopped by the side wall and compressed to move toward the z-direction. It is worth noting that the average concentration in each branch of cross unit is no longer 0.5, judging from the images obtained from C3 and C4. The fluids with high concentration ($\geq$ 0.5) enter one branch and the fluids with low concentration ($\leq$ 0.5) enter the other branch. This induces low mixing efficiency in the cross unit, which could be considered to be a shortage of the CO micromixer. Figure 3.25 shows the stream lines at five corners shown in Fig. 3.7. The stream lines are very smooth in the symmetric plane. Only at corners 4 and 5 are small vortices observed.

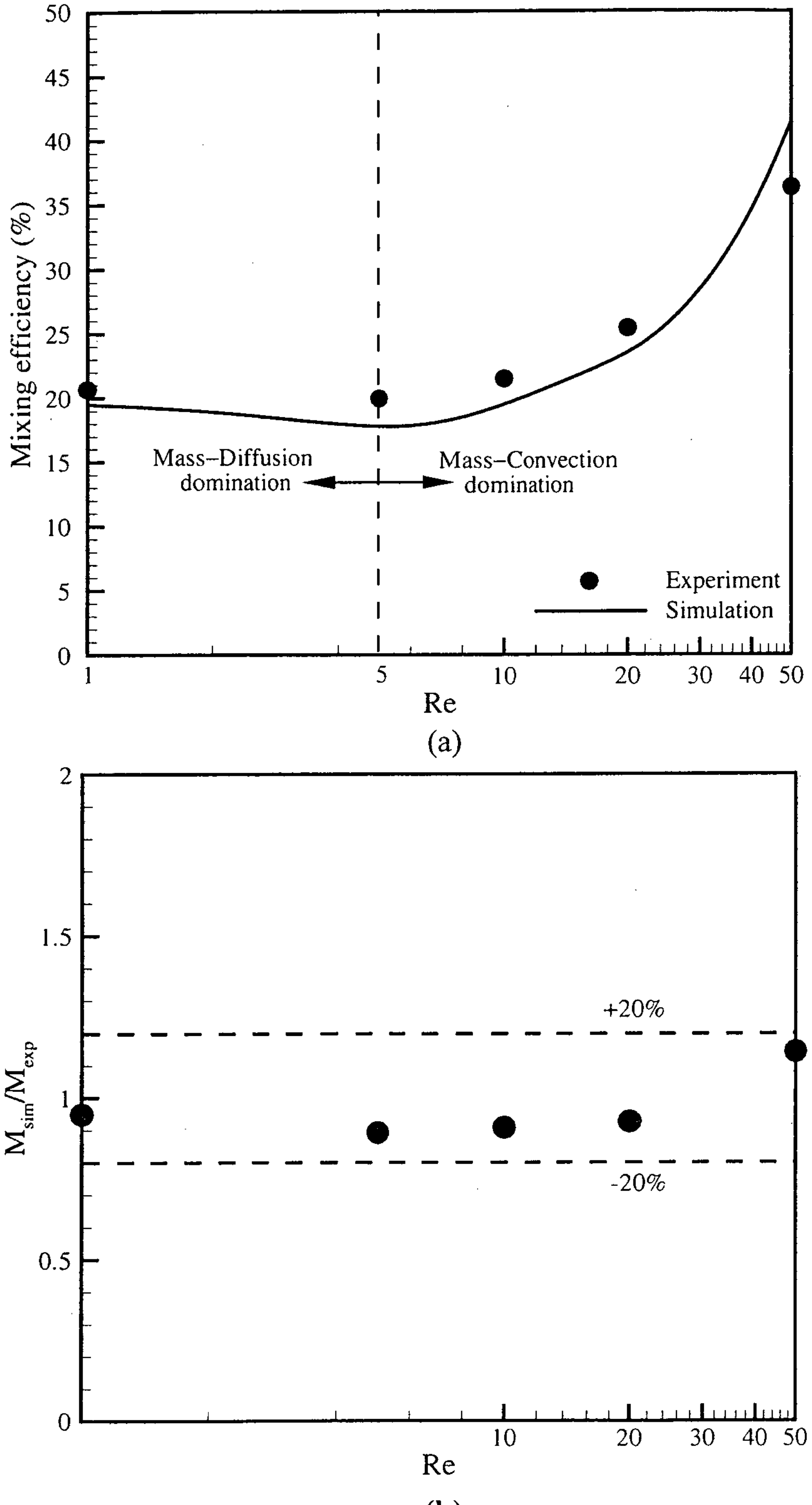

(a)

(b)

Figure 3.21: Comparison of experimental and simulation results at the exit of first cell.

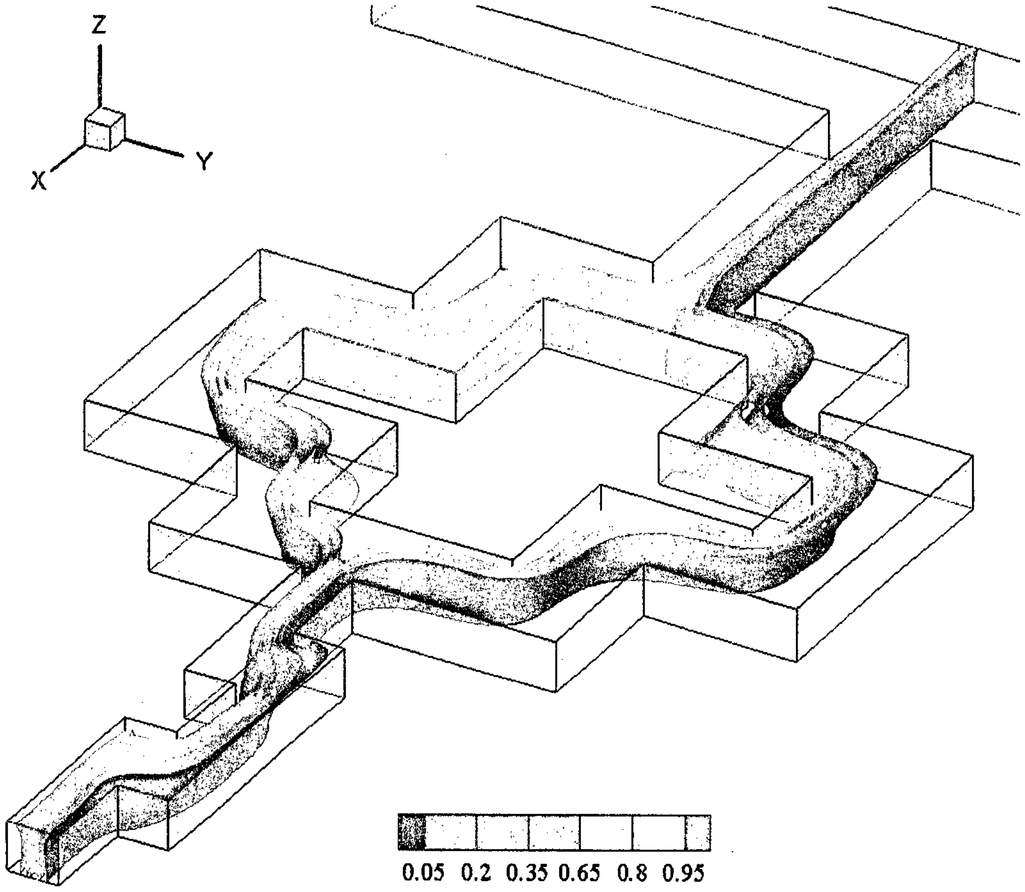

Figure 3.22: Iso-surface of concentration at $Re = 5$ in the first cell.

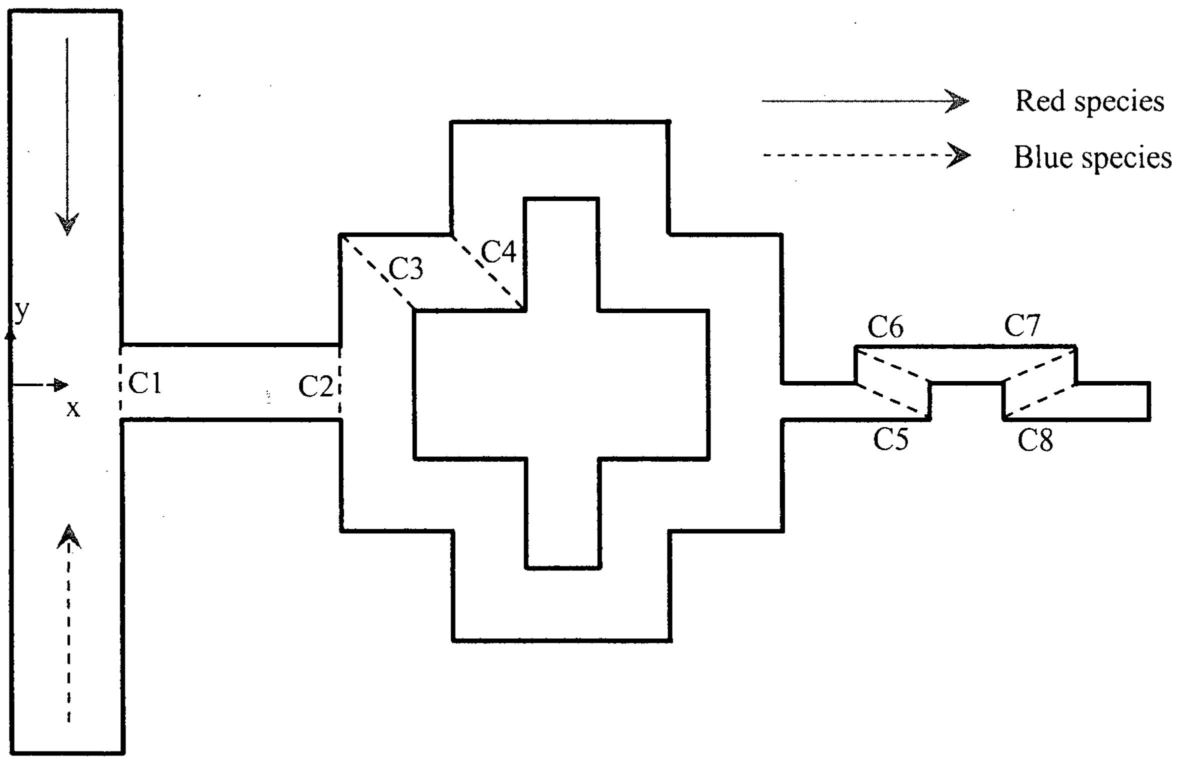

Figure 3.23: Positions of eight presented sections in the first cell.

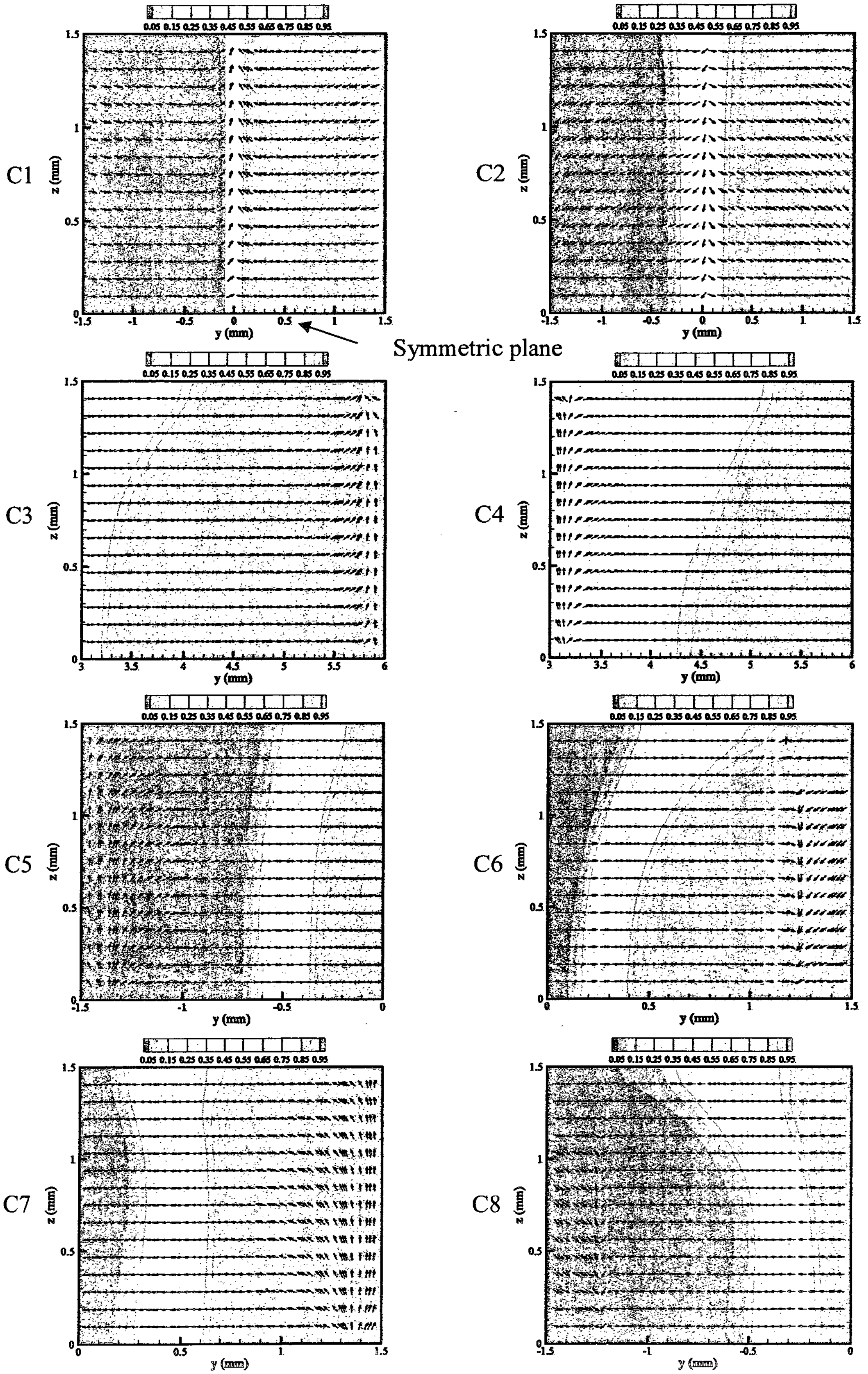

Figure 3.24: Concentration distributions and velocity vectors of eight cross-sections at $Re = 5$.

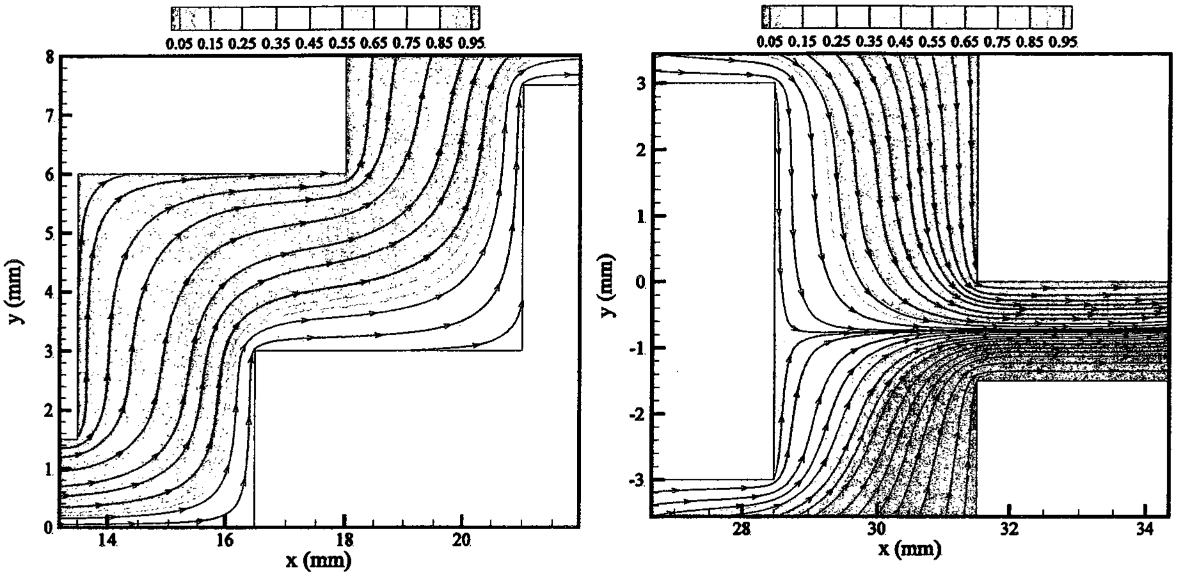

Corners 1&2

Corner 3

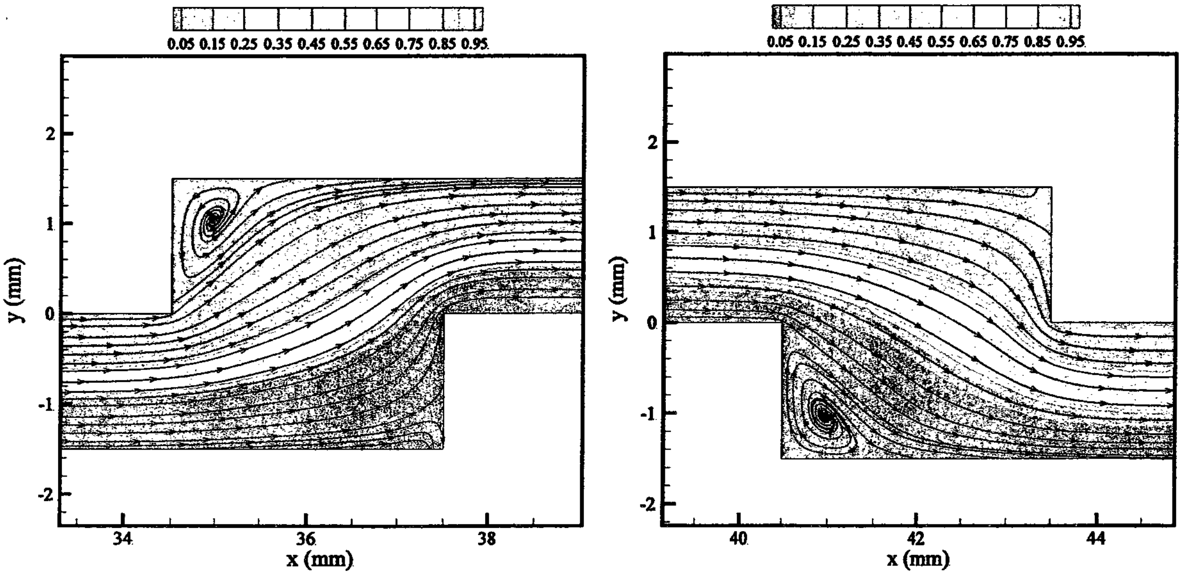

Corner 4

Corner 5

Figure 3.25: Concentration distributions and streamlines located at corners 1-5 along the symmetric plane (refer to Fig 3.7).

The mixing efficiency increases at $5 \leq Re \leq 50$ due to the change in mixing mechanism. Along with increasing Re, the inertial force becomes dominant. The mixing mechanism changes from mass-diffusion to a combination of mass-diffusion and mass-convection.

Figure 3.26 shows the iso-surface at $Re = 50$. The overlap of fluids becomes more serious compared to $Re = 5$, which increases the diffusion area. Figure 3.27 shows the concentration distributions and velocity vectors at eight cross-sections. As observed from the velocity vectors, a pair of vortices is generated at C1 for the same reason as described at $Re = 5$. However, the movement of fluids becomes greater due to the larger velocity. At C2, the mixed fluids at the top surface have a larger area than at the symmetric plane. The fluids moving toward the top surface are separated from the top wall and sub-streams move left and right. The fluids near the top wall are stretched, which lead to a larger area of mixed fluids. At C3-C8, due to higher Re, the centrifugal force is larger than at $Re = 5$. Recirculation flows are created, which increase the effect of convection on mixing. Also, the interface between two species becomes very complex, and the diffusion area is enlarged. Figure 3.28 shows the streamlines at corners 1-5 at $Re = 50$. The sub-fluids are able to separate from the main fluid so that vortices could be observed at the corners, which enhance mass-convection.

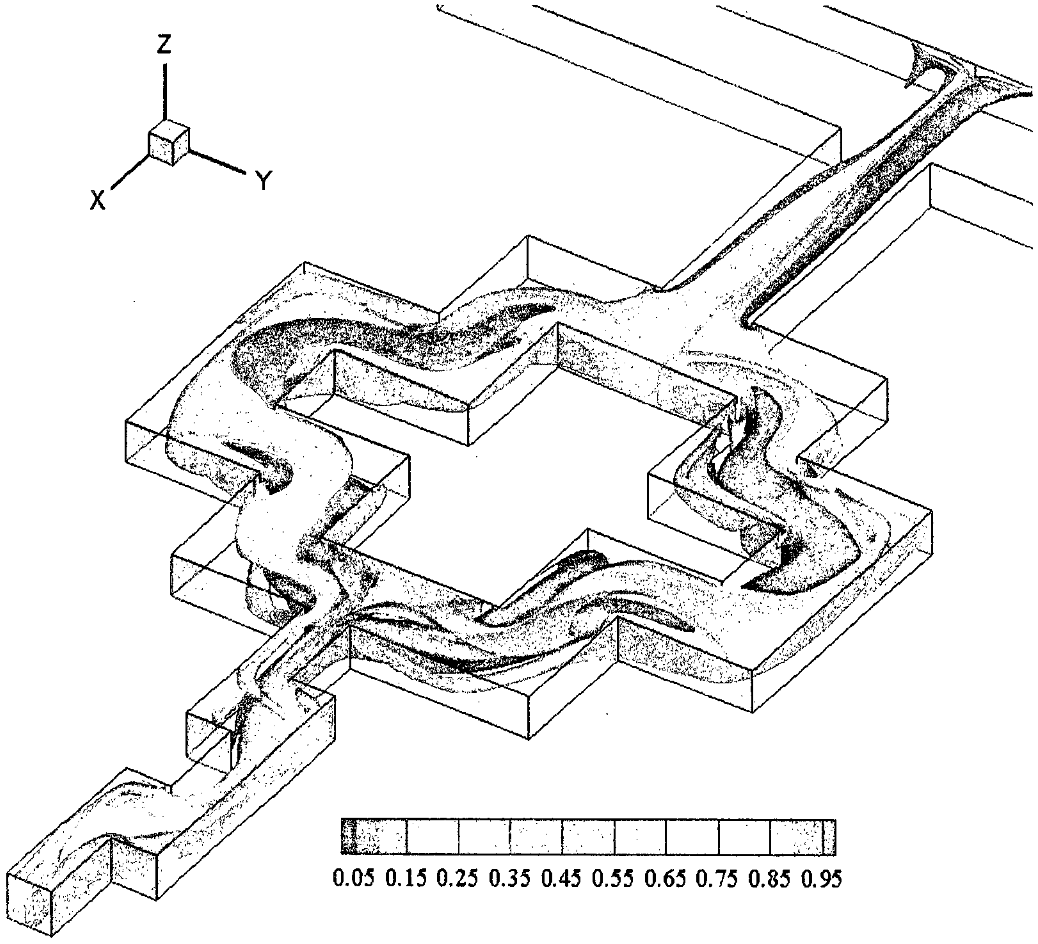

Figure 3.26: Iso-surface of concentration at *Re* = 50 in the first cell.

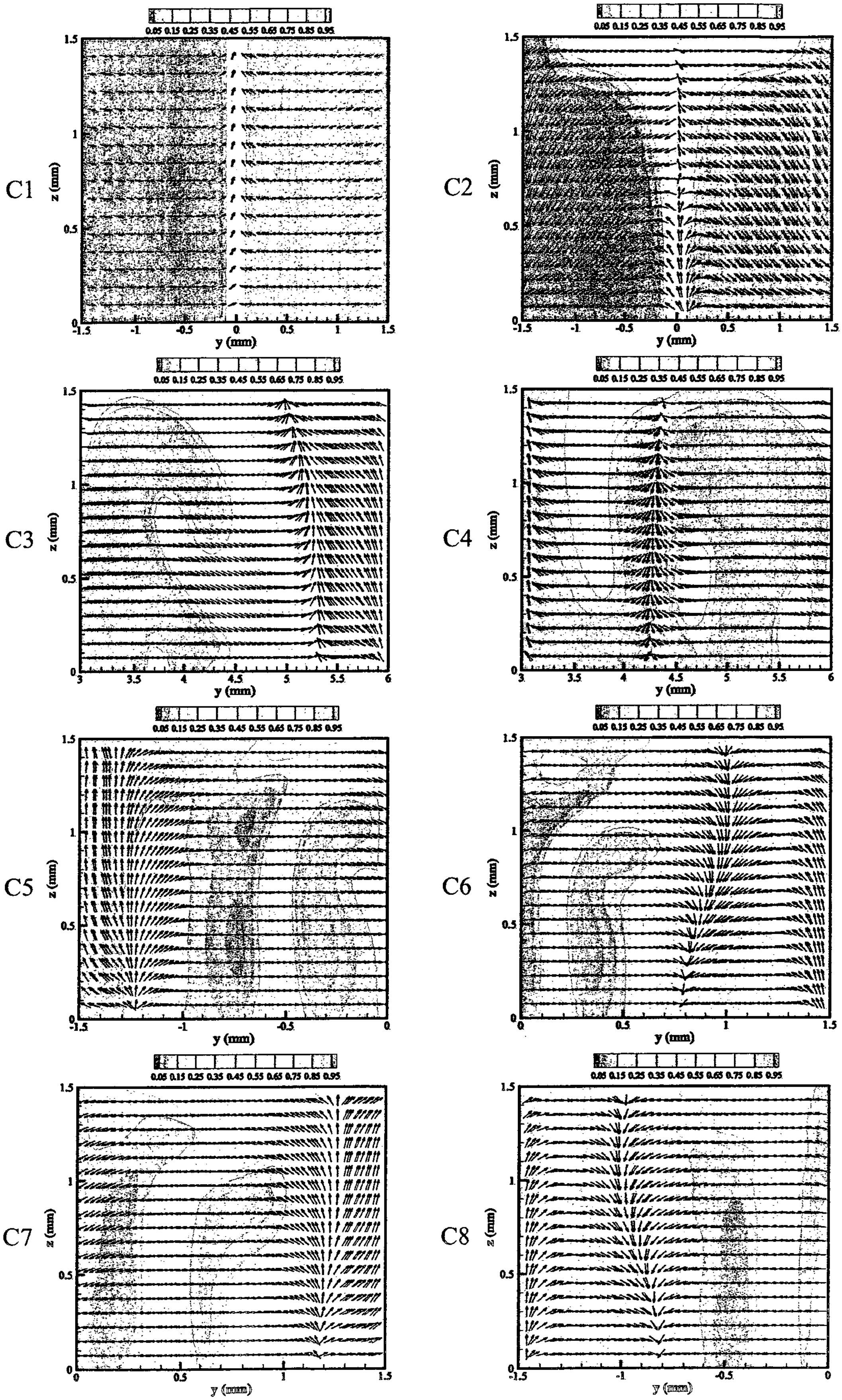

Figure 3.27: Concentration distributions and velocity vectors of eight cross-sections at *Re* = 50.

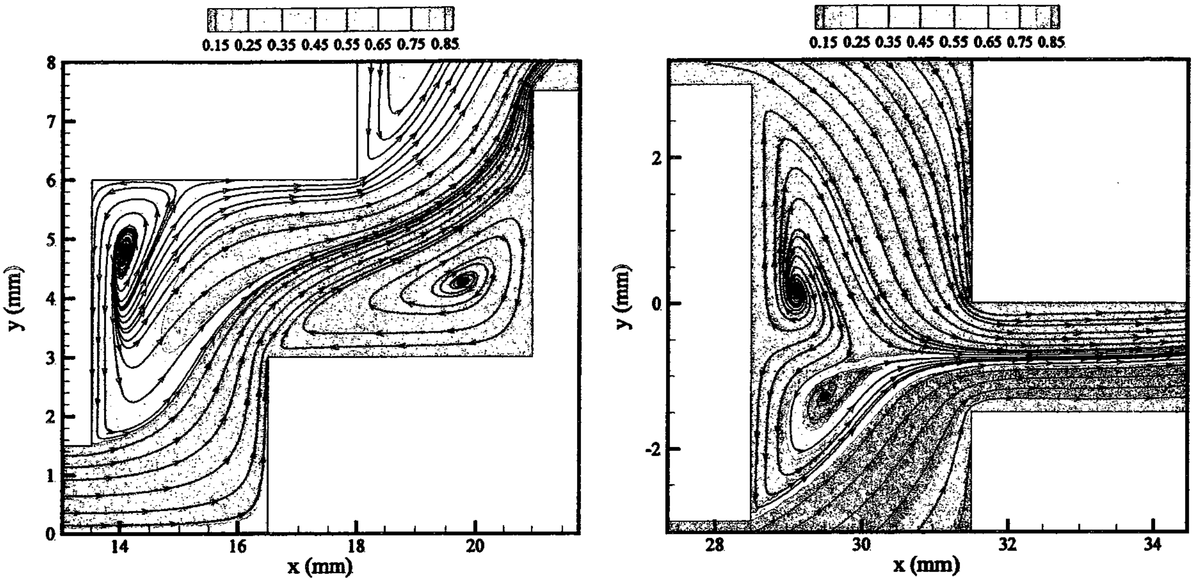

Corners 1&2

Corner 3

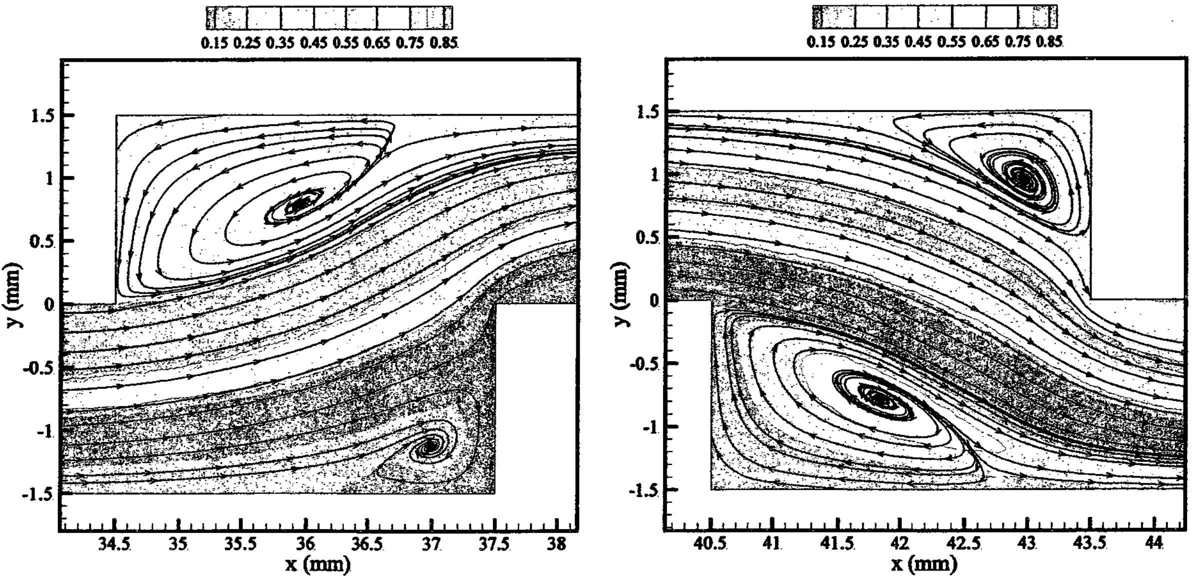

Corner 4

Corner 5

Figure 3.28: Concentration distributions and streamlines located at corners 1-5 along the symmetric plane at *Re* = 50 (refer to Fig. 3.7).

3.3 Summary

Throughout this chapter, experimental and numerical investigations are applied to a planar passive micromixer denoted as the CO micromixer. Qualitative and quantitative measurements are performed in order to observe the mixing process and obtain the mixing efficiency. The results show that the mixing efficiency decreases at $1 \leq Re \leq 10$ and increases at $10 \leq Re \leq 50$, which is considered to be caused by the change in mixing mechanism. At low *Re*, the mixing is mainly dependant on mixing diffusion. As *Re* increases, the diffusion time reduces, leading to inadequate mixing time. However, mass-convection is a major part in the mixing at high *Re*. Numerical simulation results are validated by the experiment and the comparison shows very good agreement. Hence, the numerical simulation could be trusted as an effective tool to assist in understanding the flow mixing. The simulation results show that the Dean vortex is generated in the channel at high *Re*, which enhances the mass-convection effect on mixing. The flow overlapping and folding enlarge the interface to accelerate mixing. The measured mixing efficiency ranges between 35% and 65% at $1 \leq Re \leq 50$.

Chapter 4

Interdigital-Circular Micromixer

Considering the low mixing efficiency, the modification of the CO micromixer is done in order to increase the mixing efficiency throughout this chapter. The interdigital inlet is used to increase the interface area and decrease the diffusion path. Due to the high pressure drop caused by the right corners in the CO micromixer, the circular mixing element is designed and applied, instead of the cross-omega element. The mixing investigation is performed by numerical simulation as the CFD work was verified in the previous chapter. The interdigital inlet and circular mixing element are systematically optimized by Design of Experiment (DOE) methodology to seek the optimal design dimensions.

4.1 Improvement

4.1.1 Summaries of the CO Micromixer

The CO micromixer uses the T-shaped inlet. The two working fluids are individually pushed into the channels by two syringe pumps. The two fluids flow in opposite directions, which induces the interaction of the fluids from two syringe pumps. The fluctuation of the interface causes mixing instability.

The flow separation principle is used in the CO micromixer in order to extend the mixing length and generate the vortices in the branches. However, the mixing efficiency in each branch of the cross unit is very low due to the split-and-recombine principle. One sub-stream with a higher concentration (≥ 0.5) enters one branch and the other with a lower concentration (≤ 0.5) enters the other branch. This induces uneven concentration distribution, such that the average concentration of fluids in each branch is not equal to 0.5.

In the CO micromixer, the right corners are used to generate the vortices for mass-convection enhancement. The pressure drop is also increased, which restricts practical applications.

Considering the problems mentioned above, the interdigital structure inlet is applied to achieve a parallel supply of working fluids and the circular-section mixing element is used, instead of cross-omega element, to decrease the pressure drop.

4.1.2 Interdigital-Circular Micromixer (IC)

Based on the investigation of the CO micromixer, improvements should be made on two parts: inlet structure and mixing element. The T-shape inlet causes an oscillation of the interface, which induces the uneven distribution in each branch after the main flow is separated into two substreams. In the improved micromixer, the two working fluids are supplied in parallel mode, which could reduce the interaction of the two pumps. Also, the split-and-recombine principle is applied to the CO micromixer. The flow with high concentration (> 0.5) enters one branch and the flow with low concentration (< 0.5) enters the other branch after being separated, which induces low mixing efficiency in the cross unit. The symmetrical interdigital inlet is applied to supply an average concentration of 0.5 in each branch. Also, the multi-lamination flow profile reduces the diffusion path, and each branch is filled with the flow of average concentration of 0.5. Also, the pressure drop is large in the CO micromixer due to the right corners. The circular-sector mixing element is used to achieve the split-and-recombine principle so that the pressure drop could be reduced.

Figure 4.1 shows the interdigital-Circular micromixer with 3 blue and 4 red species. The focusing regime is selected as a rectangular structure. The total width of inlet D_t and the downstream straight channel width W are fixed at 0.9 mm and 0.2 mm, respectively. The micromixer length, L, is set at 5 mm. The tested Reynolds numbers are calculated at the entrance of the downstream straight channel (Plane 1) in order to maintain the same mass flow rate among different cases. U-shaped baffles are positioned in the channel to divide the main flow into substreams. The symbol D_a represents the channel width of substreams, where odd values of a represent each channel width of red species and even values of a represent each channel width of blue species. The symbol D_u represents the width of each branch of the U-shaped baffle. The closing angle of the focusing chamber γ is fixed at 120°.

4.1.3 Numerical Simulation

Since the numerical simulation has been validated as a useful tool to predict the mixing quality and fluid characteristics in the previous section, CFD software is applied to assist in the improvement and optimization. Grid independence is performed to determine the proper grid size. Figure 4.2 shows the grid system and the concentration and velocity distributions at the intersection of the outlet and the symmetric plane. Both concentration and velocity distributions do not show large differences as the number of grids surpasses 1.1 M. Therefore, the number of 1.1 M grids is selected for further investigation.

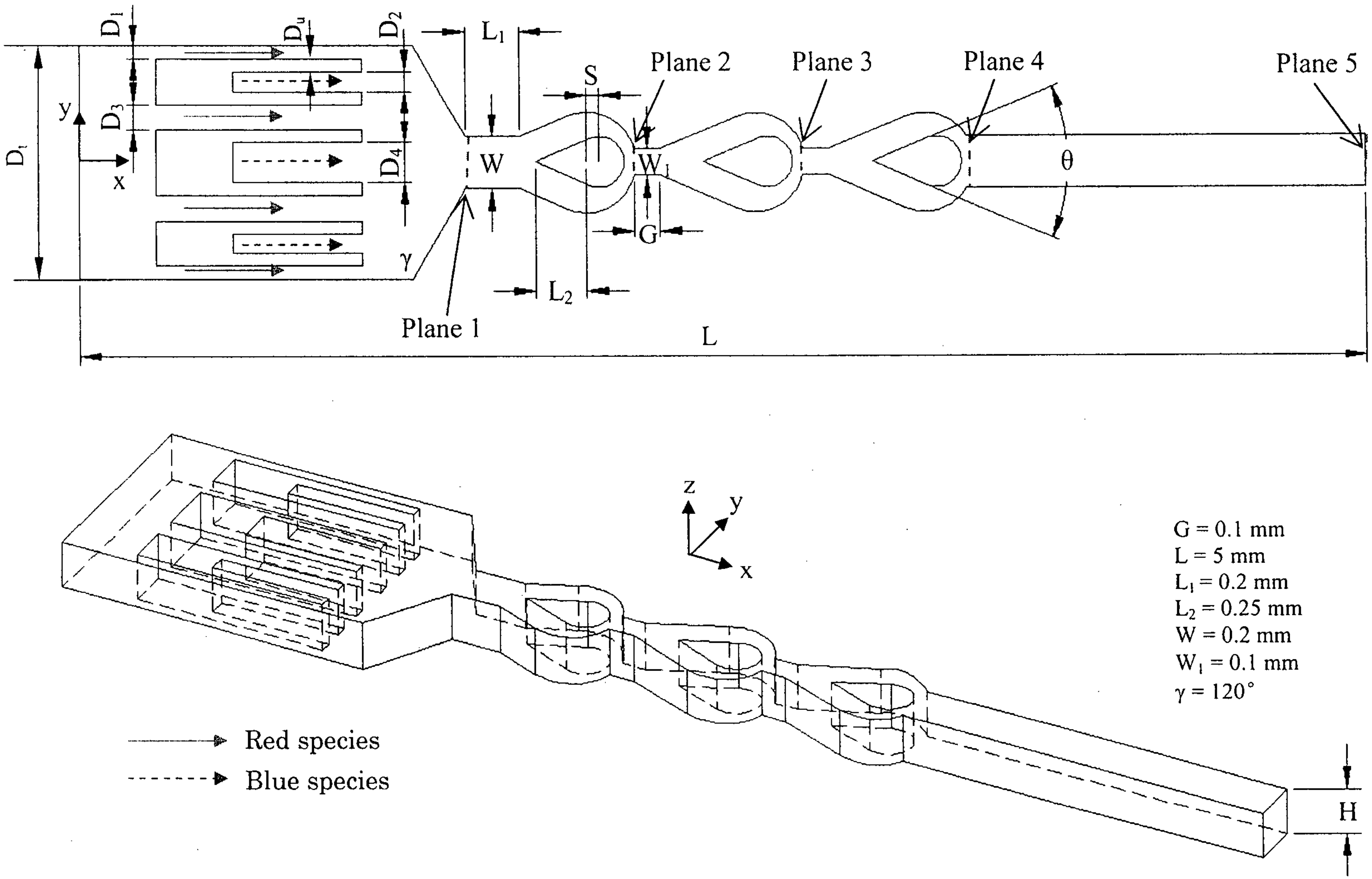

Figure 4.1: Schematic of IC-micromixer with three mixing elements and 3 blue and 4 red symmetric interdigital inlet.

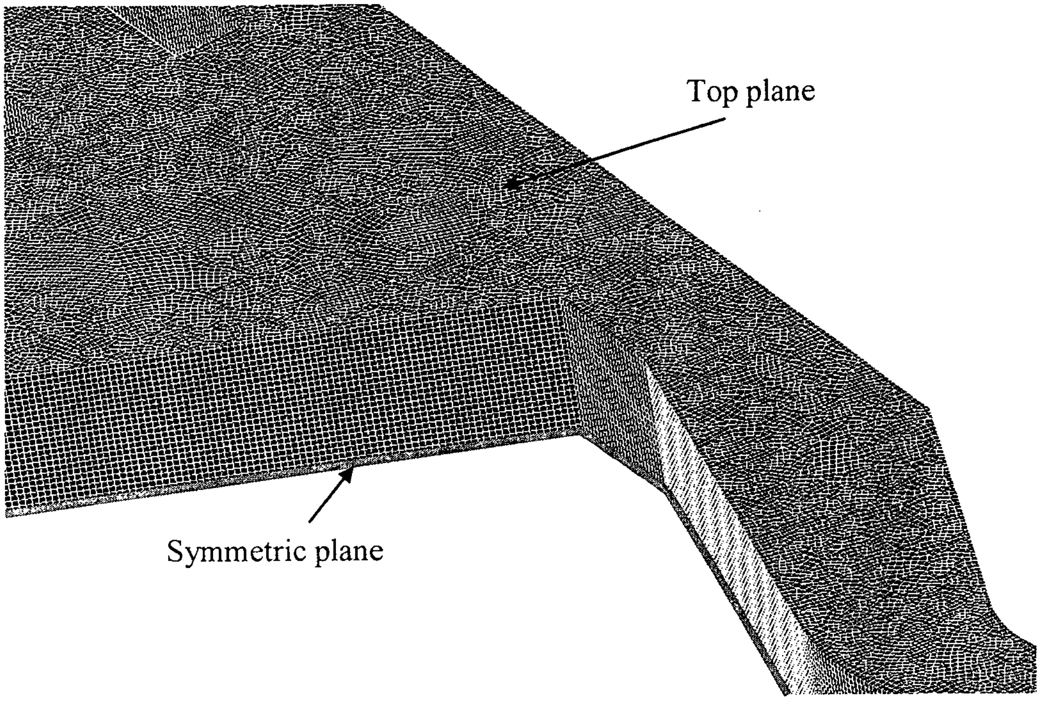

(a) Grid system of a quarter model

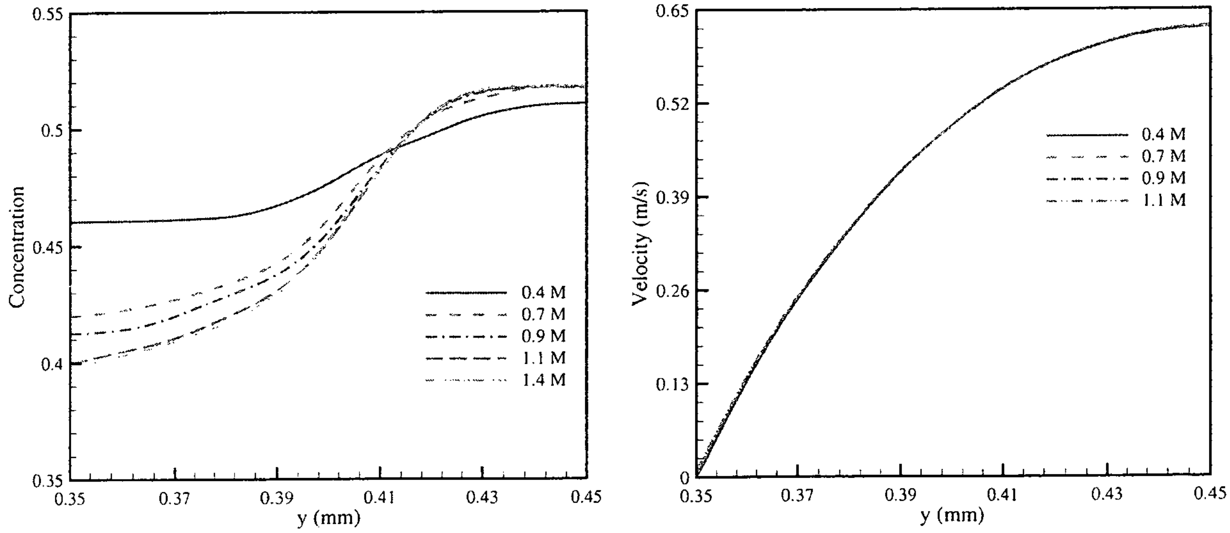

(b) Concentration and velocity distributions at the intersection between the outlet and symmetric plane.

Figure 4.2: Grid system and grid independence of the quarter model.

4.2 Optimization

4.2.1 Optimization of Interdigital Inlet

Five interdigital inlets with the straight downstream channel are designed and simulated to study the effect of the number of interdigital substreams on the mixing efficiency. Each species has uniform substream channel width. These five micromixers are named by the number of blue substreams and the number of red substreams. Considering the fabrication and cost, the minimum channel width is set at 50 μm. The total width of substreams of each species is fixed at 0.3 mm and the total width of the U-shaped baffles is also fixed at 0.3 mm. Hence, the maximum number of blue species and red species are 5 and 6, respectively. The dimensions of these five interdigital inlets are listed in Tab. 4.1. Figure 4.3 shows the mixing efficiency and pressure drop of the five micromixers at $5 \leq Re \leq 60$. The mixing efficiency increases with an increase in the number of substreams over the entire *Re* range due to the reduced diffusion path. The pressure drop also increases as the lamellar width decreases, as expected. The maximum pressure drop at $5 \leq Re \leq 60$ is less than 1.4 kPa in all five micromixers. Figure 4.4 displays the concentration distribution of five micromixers located at the downstream entrance (Plane 1) and the outlet. Only a quarter of the cross-section is shown due to the symmetric structure. A large part of the fluid tends to be green, which represents ideal mixing. More fluid achieves ideal mixing as the lamellae width decreases, which is caused by the reduced diffusion path between two adjacent species and the increased interface area. At $Re = 50$, the interface is distorted near the top wall as a result of the focusing effect. The fluid is compressed by centrifugal forces induced by the focusing chamber before entering the downstream channel. It is worth noting that the fluid near the

Table 4.1: Dimensions of five interdigital micromixers with different lamellar numbers (units in μm)

Blue species number	Red species number	Channel width of each blue species	Channel width of each red species	The branch width of U-shape baffle
1	2	300	150	150
2	3	150	100	75
3	4	100	75	50
4	5	75	60	37.5
5	6	60	50	30

Table 4.2: Dimensions of three interdigital micromixers with uneven channel width (units in μm)

Case No.	D_1	D_2	D_3	D_4	$D_5(D_3)$	$D_6(D_2)$	$D_7(D_1)$	D_u
1	50	55	100	190	100	55	50	50
2	50	75	100	150	100	75	50	50
3	50	100	100	100	100	100	100	50

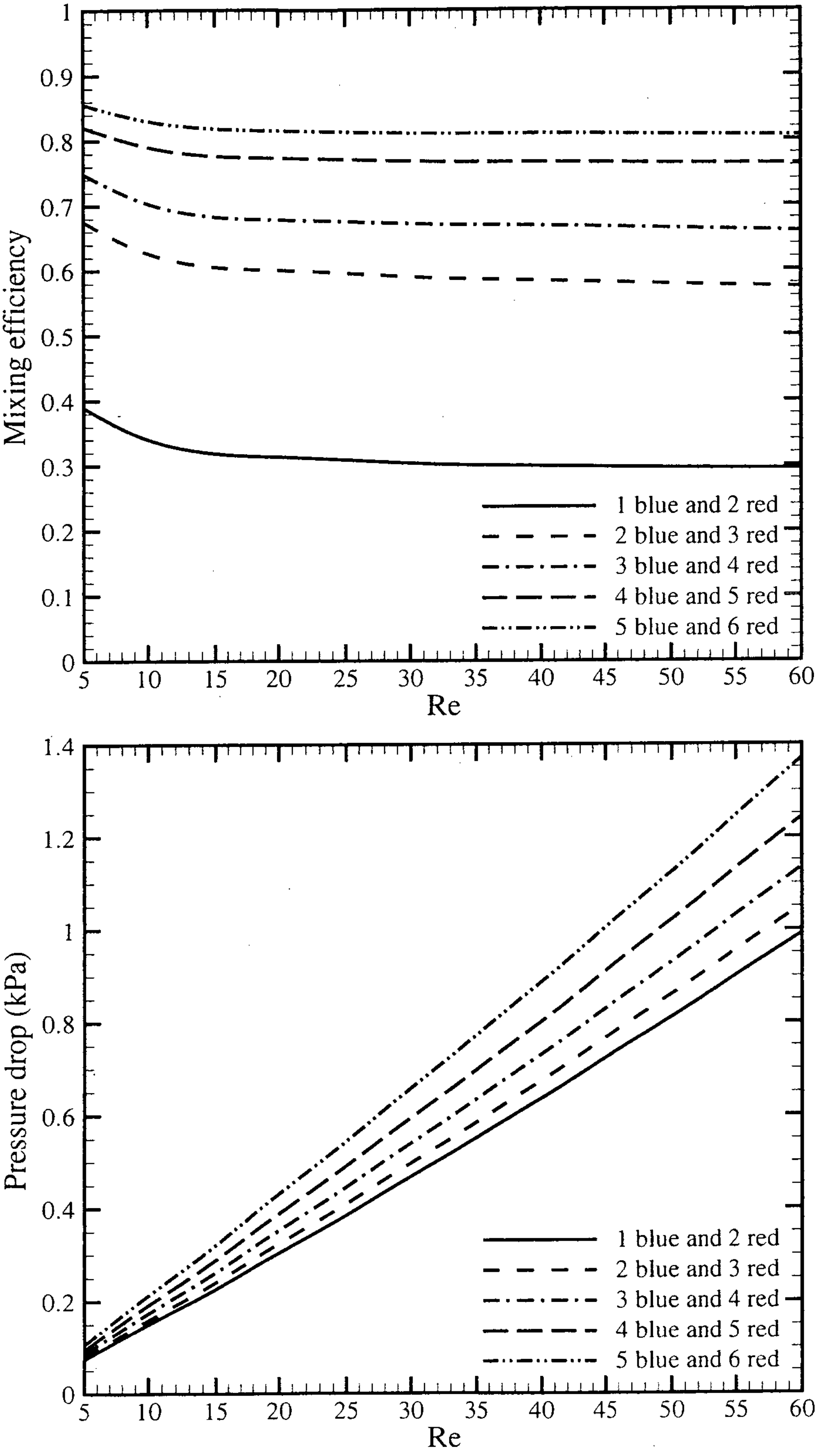

Figure 4.3: Mixing efficiency and pressure drop of five interdigital micromixers with different channel numbers.

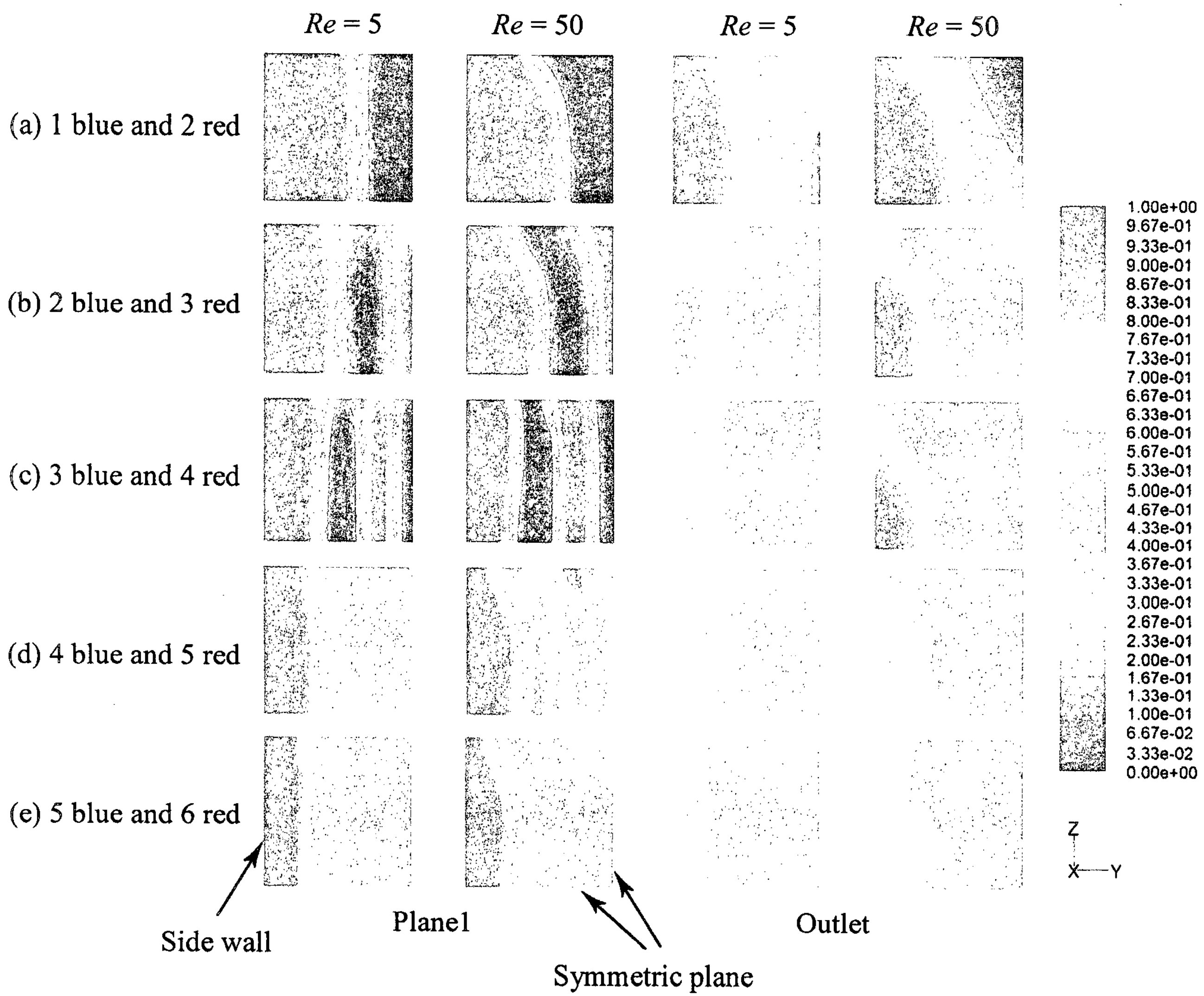

Figure 4.4: Concentration distributions of five interdigital micromixers at Plane 1 and outlet at $Re = 5$ and 50.

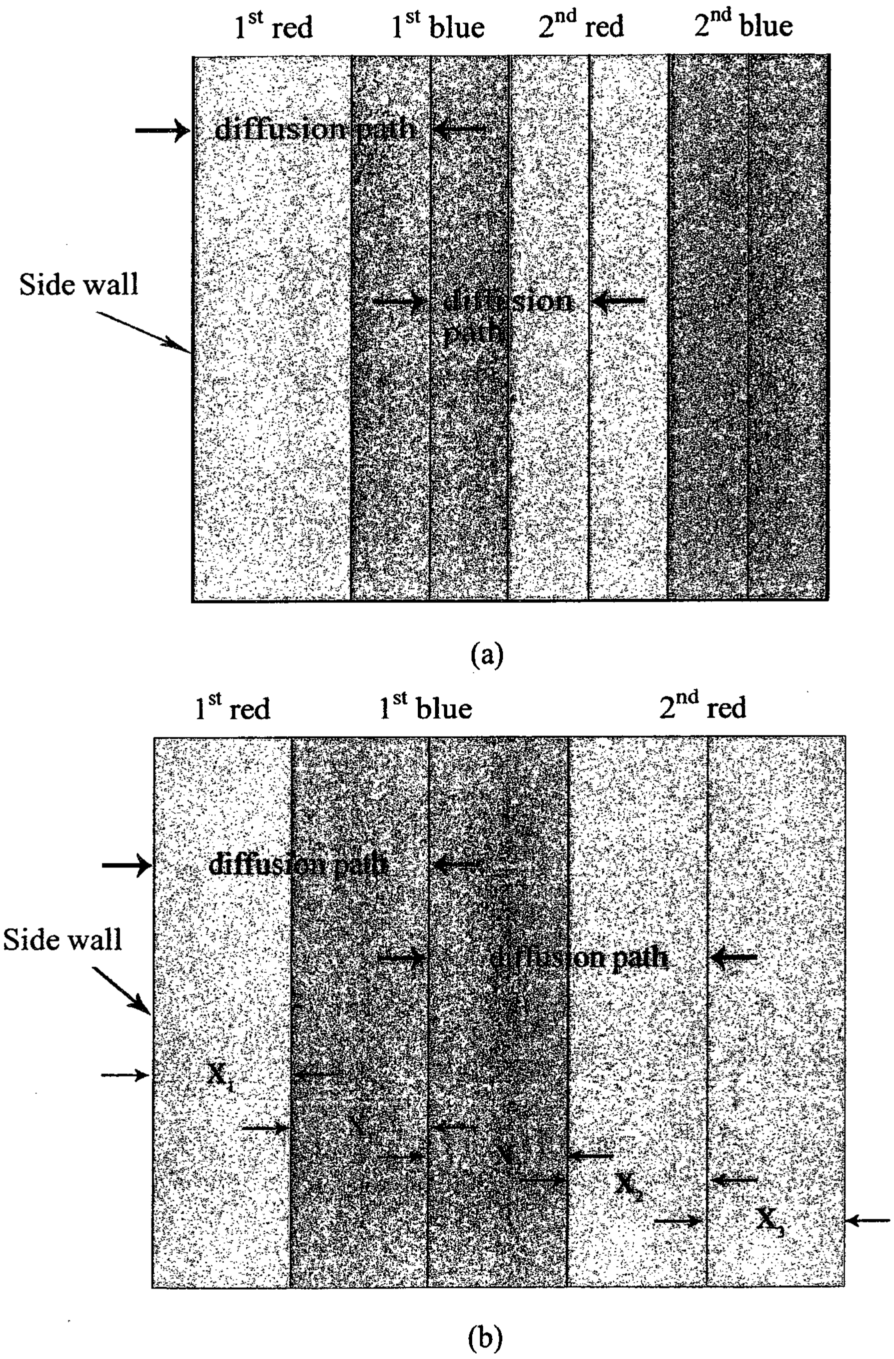

Figure 4.5: Mixing principle of the interdigital micromixer with even and uneven channel width distribution.

side wall is difficult to mix in all five micromixers. Figure 4.5 shows the mixing principle of the interdigital micromixer. The diffusion path between the 1st red and 1st blue species near the side wall is larger than those in the middle if each species has uniform channel width. When the fluid located at the center of the cross-section achieves ideal mixing, a portion of fluid near the side wall is inadequately mixed.

The species near the side walls only diffuse in one direction, as shown as 1st red species in Fig. 4.5a. However, other species diffuse in two directions, as shown as 1st blue, 2nd red and 2nd blue species. If the even channel width is applied to each species, the diffusion path of fluid near the side wall is larger than at other locations. Fluids near the side walls are therefore difficult to mix since the diffusion path is larger than the fluids in the middle of the channel. Uneven channel width is applied to the interdigital design in order to enhance the mixing near the side walls. Enlarging the central lamellar width can decrease the diffusion path of fluid near the side walls. The mixing principle of the micromixer with uneven channel width is shown in Fig. 4.5b. The channel width of each species is calculated as follows:

$$D_1 = x_1,\ \ D_2 = x_1 + x_2,\ \ D_3 = x_2 + x_3,\ \ldots,\ \ D_a = x_{a-1} + x_a$$

$$2i \times D_u = 0.3$$

$$D_1 + D_3 + D_5 + \cdots + D_a = D_2 + D_4 + D_6 + \cdots D_{a-1} = 0.3$$

$$a = 2i + 1, \qquad i = 1,2,3\cdots\cdots$$

where i is the number of blue substreams. Considering the pressure drop and manufacturing cost, the minimum channel width is set at 50 μm, such that an additional limiting condition is:

$$D_i \geq 50\mu\text{m}$$

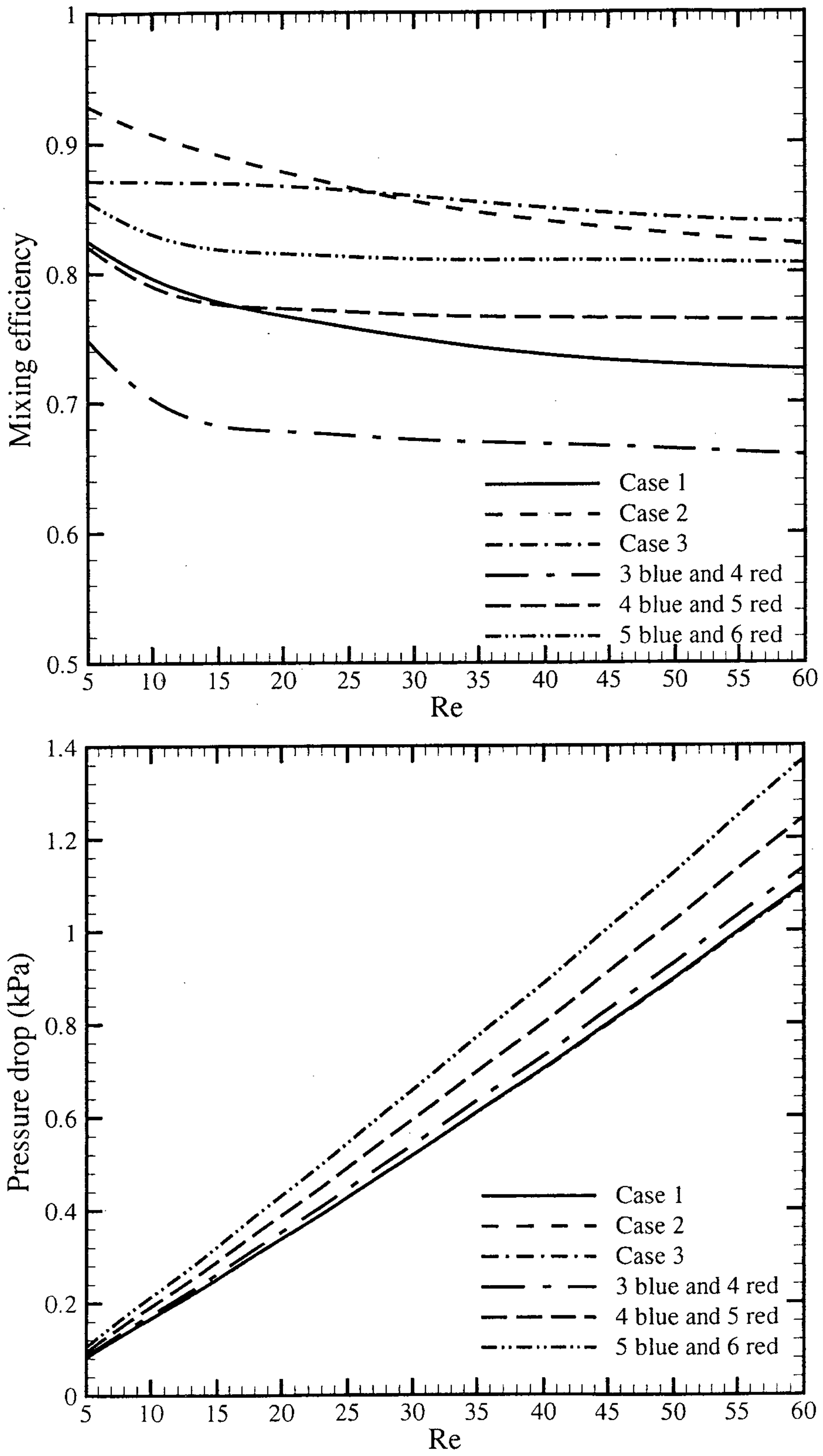

Figure 4.6: Mixing efficiency and pressure drop of even and uneven interdigital micromixers.

In this study, 3 blue and 4 red species are selected to investigate the effect of uneven channel width, such that i is set at 3. Many solutions may be obtained from the above equations. Three cases are proposed for further investigation. The dimensions of these three micromixers are listed in Tab. 4.2. Figure 4.6 shows the mixing efficiency and pressure drop of six interdigital micromixers. The micromixers with uneven lamellar width are named as case numbers 1, 2 and 3, as shown in Tab. 4.2. The three improved micromixers have almost the same pressure drop. Compared to the micromixer of 3 blue and 4 red species with even lamellar width, the three micromixers with uneven lamellar width have better mixing efficiency and lower pressure drop. It is worth noting that case 2 and case 3 have even better mixing efficiency and lower pressure drop than the micromixer of 5 blue and 6 red species. However, the mixing efficiency of case 1 is worse. Figure 4.7 shows the concentration distribution of three improved cases with uneven lamellar width. At the outlet, the fluids located at the right side in case 1 at $Re = 5$ are light blue. When Re reaches 50, the fluids located at S-1 in case 1 shows very poor mixing due to the large center lamellar width. For the given mixing length, adequate mixing may not be achieved. The poor mixing area moves from the side wall to the center. The concentration distributions for case 2 and case 3 at $Re = 5$ and 50 show good mixing judging from the color. Only small portions of the fluid show low mixing efficiency. The interdigital micromixer with uneven channel width can enhance the mixing. Therefore, the uneven lamellar interdigital inlet is applied and case 2 is selected as the inlet of the IC micromixer for future investigations.

4.2.2 Optimization of Circular-sector Mixing Element

In order to optimize the mixing element, the Taguchi method and Response Surface

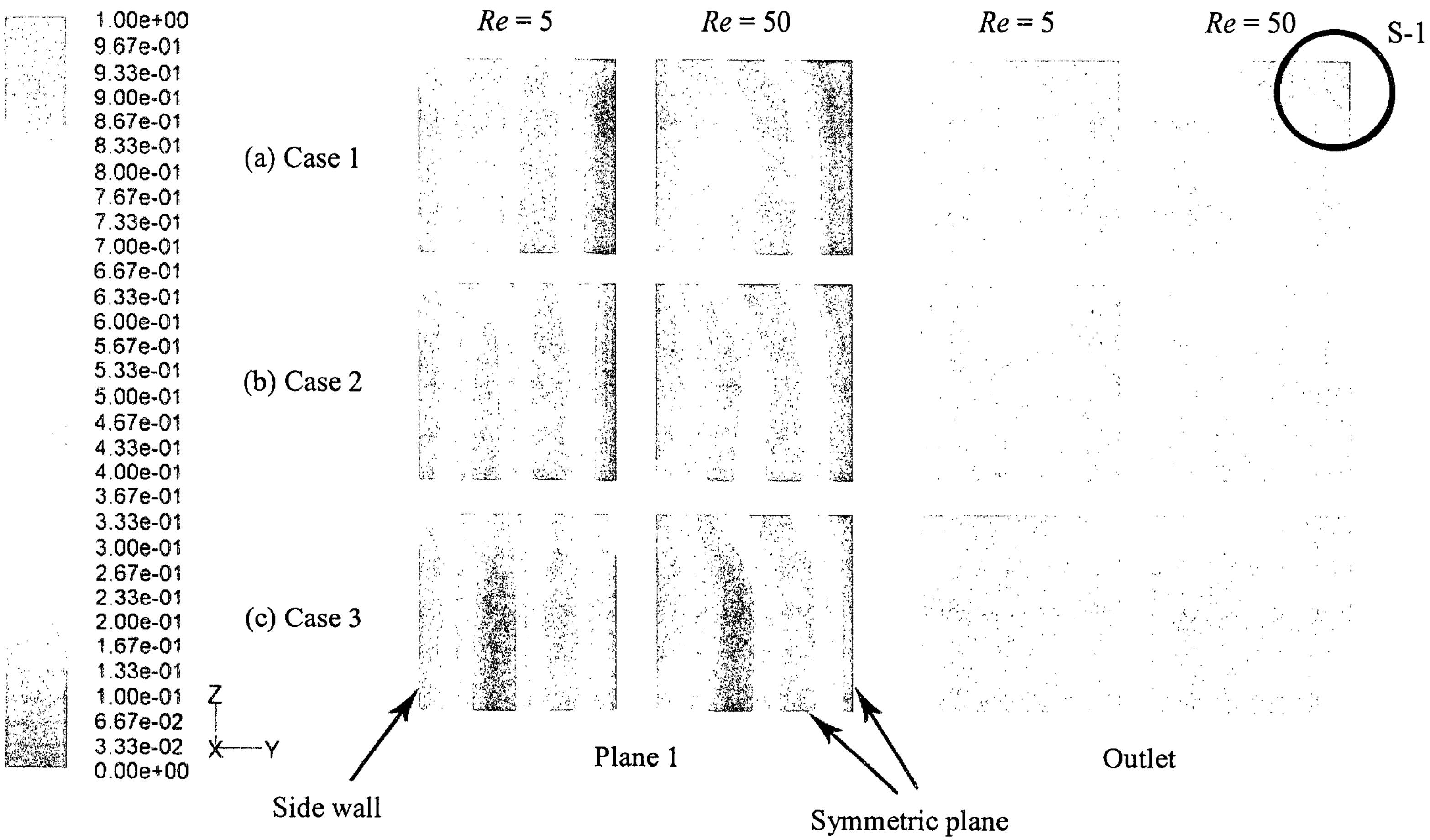

Figure 4.7: Concentration distributions of three interdigital micromixers with uneven channel width distribution.

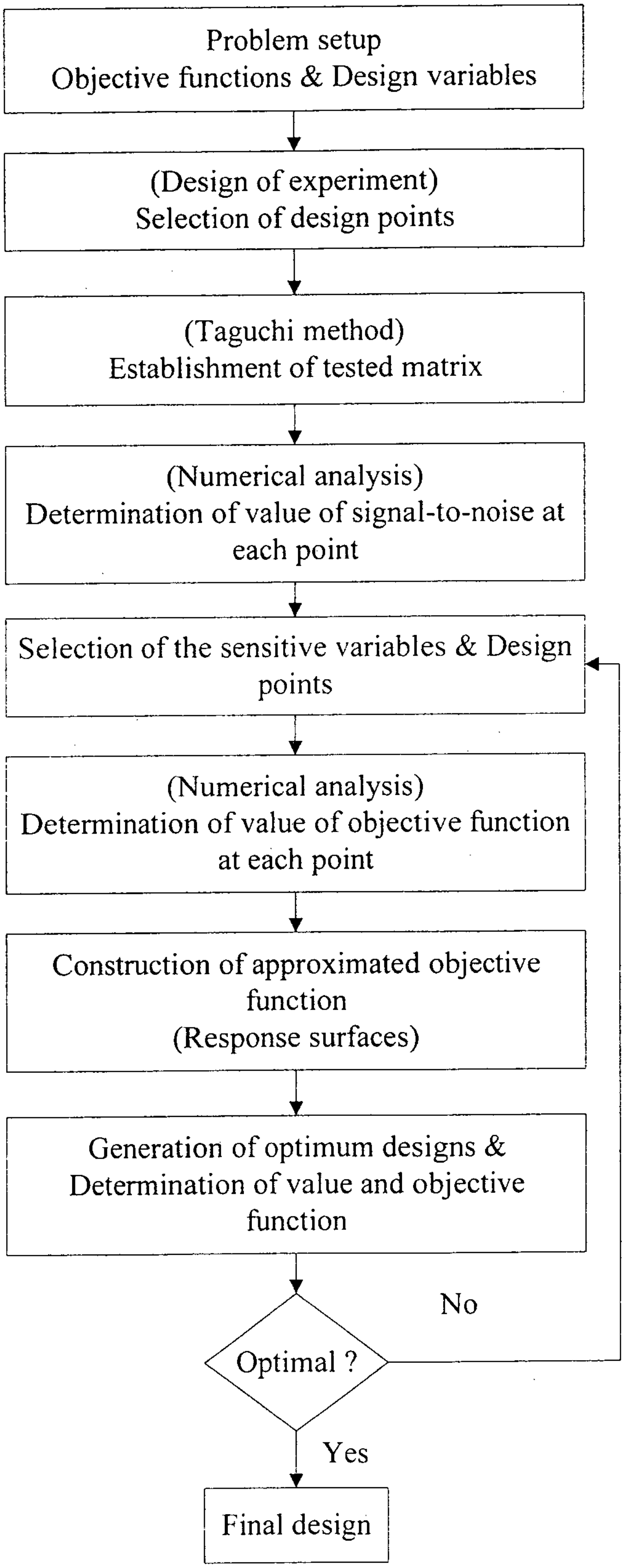

Figure 4.8: Analysis flowchart used to achieve the systematic optimization.

Methodology (RSM) are applied to determine the optimal design dimensions. The optimization procedure is described in the flowchart, as shown in Fig. 4.8. The process starts with the selection of design parameters, their range of variation, and the objective function. Once the design parameters are selected, the Design of Experiment (DOE) method is used to create the experimental table which corresponds to different geometries representing the design space. These geometries will then need to be evaluated by CFD in order to compute the objective function. First, the flow field in all configurations is computed and the most sensitive design parameters to the objective function are determined by the Taguchi method. However, the Taguchi method is not able to determine the optimal point. A new experimental table is built and Response Surface Methodology can be used to determine the optimal point. The response surface enables the user to evaluate the objective function without carrying out expensive CFD evaluations of each configuration.

One of the key aspects affecting the success of the proposed design methodology is the choice of design parameters and their ranges of variation. First, sensitivity analysis needs to be performed in order to establish the most important design parameters to use for the detailed study. Three parameters, open angle (θ), displacement of obstacles (S), and depth of microchannels (H), are selected, and three different levels are determined and listed in Tab. 4.3. In the micromixer development, the mixing efficiency is the most important parameter used to evaluate the micromixers. Hence, the mixing efficiency is selected as the objective function. The definition of mixing efficiency has been given in Eq. 3.13.

An experiment table of nine designs is generated by using the Orthogonal Array (OA) L_9 of the Taguchi Method, as shown in Tab. 4.4. The flow in these nine cases is analyzed by CFD at $Re = 10$ in the mixing channel to compute the objective function (mixing efficiency). Taguchi's Signal-to-Noise (S/N) is used to evaluate the influence of design parameters on the mixing efficiency. To obtain the S/N ratios based on the simulation results, the square of standard deviation of the concentration at the outlet of micromixer model is calculated by,

$$\sigma^2 = \frac{1}{n}\sum_{i=1}^{N}(c_i - c_\infty)^2 \tag{4.1}$$

where c_i is the concentration distribution of one of the fluid species at the i^{th} cell of the mesh at the outlet, c_∞ is the concentration of complete mixing, and n is the number of cells defined by the mesh at the outlet. The signal-to-noise (η) could be evaluated by:

$$\eta = \frac{S}{N} = -10\log\sigma^2 \tag{4.2}$$

Table 4.5 shows the S/N results of nine models. To evaluate the contribution that each level of a design parameter has on the S/N ratio of the mixing efficiency, the mean of the S/N ratios of the experiments in the OA L_9 where the level of the design parameter is present is calculated. For example, the second level of parameter B (the 2nd parameter), B2, is present in the 2nd, 5th, and 8th experiments in OA L_9, so the mean of the S/N ratios of these experiments is calculated. The results are displayed in Fig. 4.9 and Tab. 4.6, where the positive slope of the curves indicates that increasing the corresponding parameter value results in a higher mixing efficiency, and vice versa. The results show that the open angle and displacement of obstacles are more sensitive than the depth of microchannels to the mixing efficiency. Hence, the open angle and displacement of

Table 4.3: Design parameters and levels used in the optimization

Levels	Parameters		
	A(θ)	B(S/W)	C(H/W)
1	35°	-0.25	0.5
2	40°	0	0.75
3	45°	0.25	1

Table 4.4: Orthogonal array L_9 (design matrix)

Cases	Parameters		
	A	B	C
1	1	1	1
2	1	2	2
3	1	3	3
4	2	1	2
5	2	2	3
6	2	3	1
7	3	1	3
8	3	2	1
9	3	3	2

Table 4.5: The S/N and mixing efficiency of nine cases

Case	σ	S/N	Mixing efficiency	Pressure drop (Pa)
1	0.341	9.357	0.319	798
2	0.340	9.360	0.319	395
3	0.321	9.870	0.358	395
4	0.344	9.277	0.313	410
5	0.351	9.104	0.315	268
6	0.329	9.669	0.343	838
7	0.331	9.602	0.338	284
8	0.339	9.388	0.321	749
9	0.322	9.843	0.356	442

Table 4.6: The average S/N of each of nine design parameters

Parameter	Average of S/N (dB)
A1	9.529
A2	9.350
A3	9.611
B1	9.412
B2	9.284
B3	9.794
C1	9.471
C2	9.493
C3	9.525

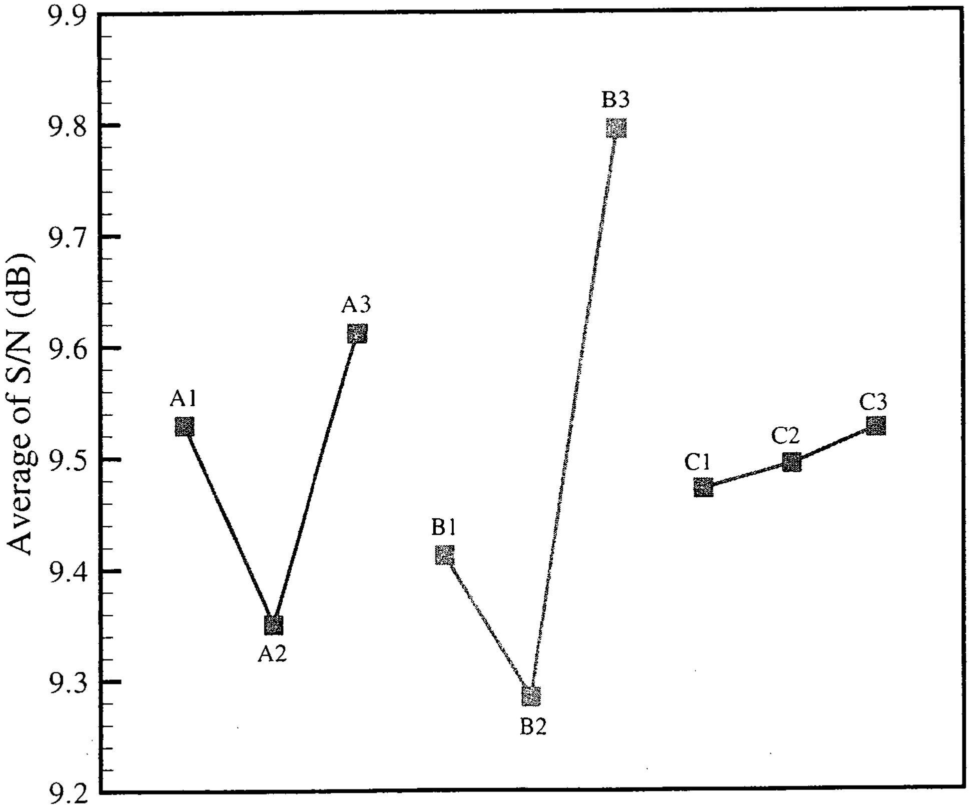

Figure 4.9: The average S/N of three design parameters at three levels.

obstacles are selected to be further investigated to determine the optimal point. The depth of microchannels is set to 0.2 mm.

The response surface methodology is an optimization method that is comprised of a series of mathematical and statistical processes. It includes the construction of the response surface by interpolating data and optimization of the objective function on the response surface. In the present work, RSM is used to obtain the optimal point. The optimization problem is defined as the maximization of an objective function, $M(x)$, within $x_i^{lower} \le x_i \le x_i^{upper}$, where x is a vector of design parameter and x_i^{lower} and x_i^{upper} are the lower and upper bounds of each design parameter, respectively. Numerical analyses at the prescribed design points are performed and the results are used to construct a response surface. In this study, the response model is assumed to be a second order polynomial that can be expressed as:

$$M(x) = \beta_0 + \sum_{i=1}^{n} \beta_i x_i + \sum_{i=1}^{n} \beta_{ii} x_i^2 + \sum_{i<j}^{n} \beta_{ij} x_i x_j \tag{4.3}$$

where n is the number of design parameters and x and β indicate the design parameter and the coefficient, respectively. Unknown coefficients of the polynomial are obtained from a standard least-squares regression method by using calculated response at design points.

The new variable levels are shown in Tab. 4.7. The natural variables (real design parameters) are normalized into code variables by,

$$x_i = \frac{\xi_i - Value_{i,center}}{\left| Value_{i,\max} - Value_{i,center} \right|} \tag{4.4}$$

where ξ is the natural variable, x is the coded variable, and $Value_{center}$ is the value of

Table 4.7: The design parameters used for response surface model

Design parameter		lower	center	upper
Coded variable (x)		-1	0	1
Natural variables	S/W (ξ_1)	-0.25	0	0.25
	θ (ξ_2)	35°	40°	45°

Table 4.8: The tested matrix and response of response surface model

Case	Natural variables		Coded variables		Response
	ξ_1	ξ_2	x_1	x_2	y
10	-0.25	35°	-1	-1	0.3222
11	-0.25	40°	-1	0	0.3059
12	-0.25	45°	-1	1	0.3379
13	0	35°	0	-1	0.3293
14	0	40°	0	0	0.3150
15	0	45°	0	1	0.3331
16	0.25	35°	1	-1	0.3580
17	0.25	40°	1	0	0.3554
18	0.25	45°	1	1	0.3592

center point. Hence, the range of coded variables of each design parameter is $-1 \le x_i \le 1$. Based on the RSM, the response surface equation could be obtained as:

$$\hat{y} = 0.3161 + 0.0178x_1 + 3.433\times10^{-3}x_2 - 3.62\times10^{-3}x_1x_2 + 0.01396x_1^2 + 0.01451x_2^2 \quad (4.5)$$

Variance and regression analyses are done to measure the uncertainty in the set of coefficients of the polynomial function. From the results of analyses for the response surface, the coefficient of multiple determinations, R^2, is determined to be 94.7%, and the adjusted coefficient of multiple determinations, R^2_{adj}, is determined to be 92.9%. Both coefficients are larger than 90%, such that the response values are considered to be accurately predicted by the response surface model.

Figure 4.10 shows the response surface within the range of design parameters. A lowest point could be observed. However, the maximum value is needed in the present problem. The maximum value appears at the point of (0.25, 45°). The corresponding response is 0.362, which is considered to be the optimal point. Hence, the final design with the optimal interdigital inlet and mixing element is built and investigated by numerical simulation.

Figure 4.11 shows the iso-surface of concentration in the optimal design with the interdigital inlet of 1 blue and 2 red at $Re = 1$ and 50. In the circular sector, the fluids flow side by side at $Re = 1$. The mixing mechanism is molecular diffusion only. Mixing is mainly dependent on the interdigital structure which increases the contact area. Furthermore, the channel width decreases along the mixing path, caused by the displacement in circular sectors, which reduces the diffusion path and has a focusing effect on the mixing. At $Re = 50$, the flow overlapping and folding characteristics could be observed in the circular sectors. A part of the species is compressed from the inner

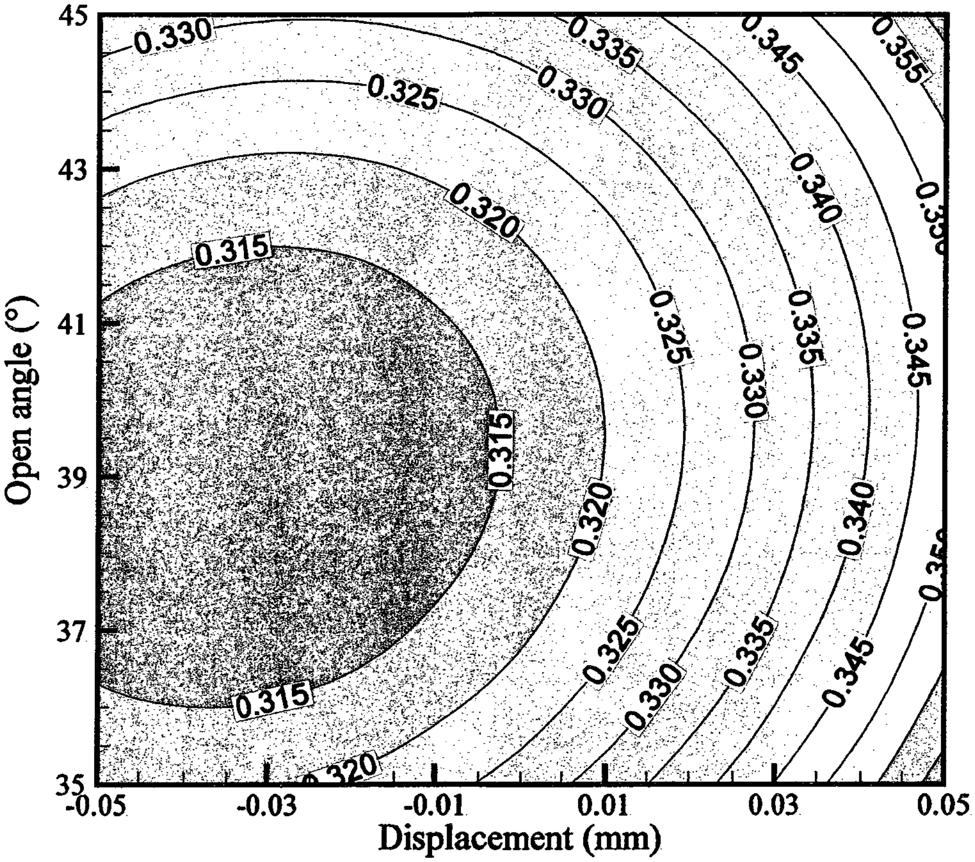

Figure 4.10: Response surface of optimization.

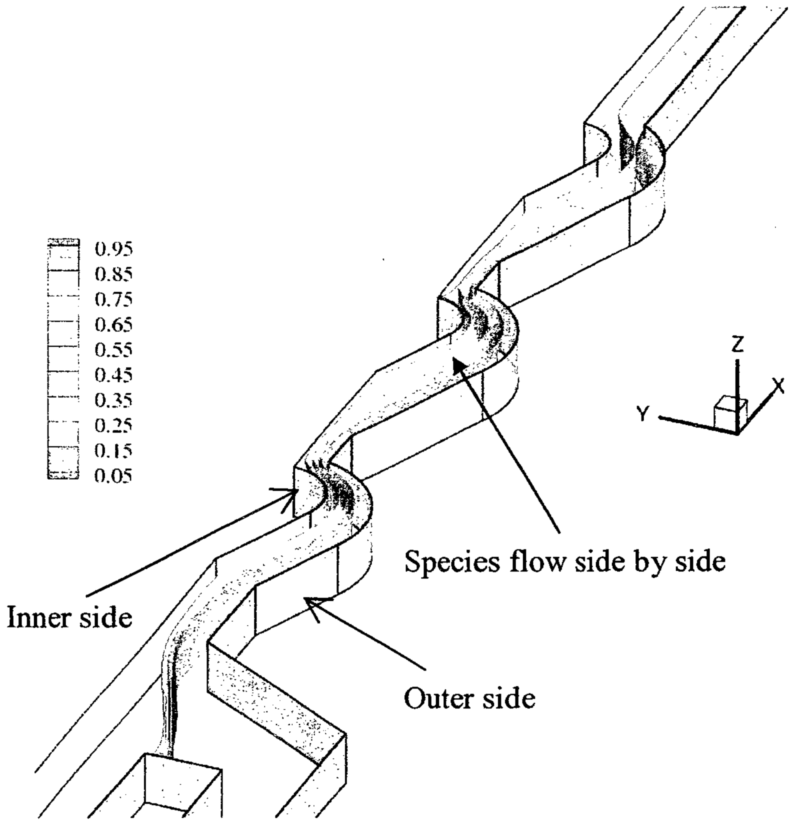

(a) *Re* = 1

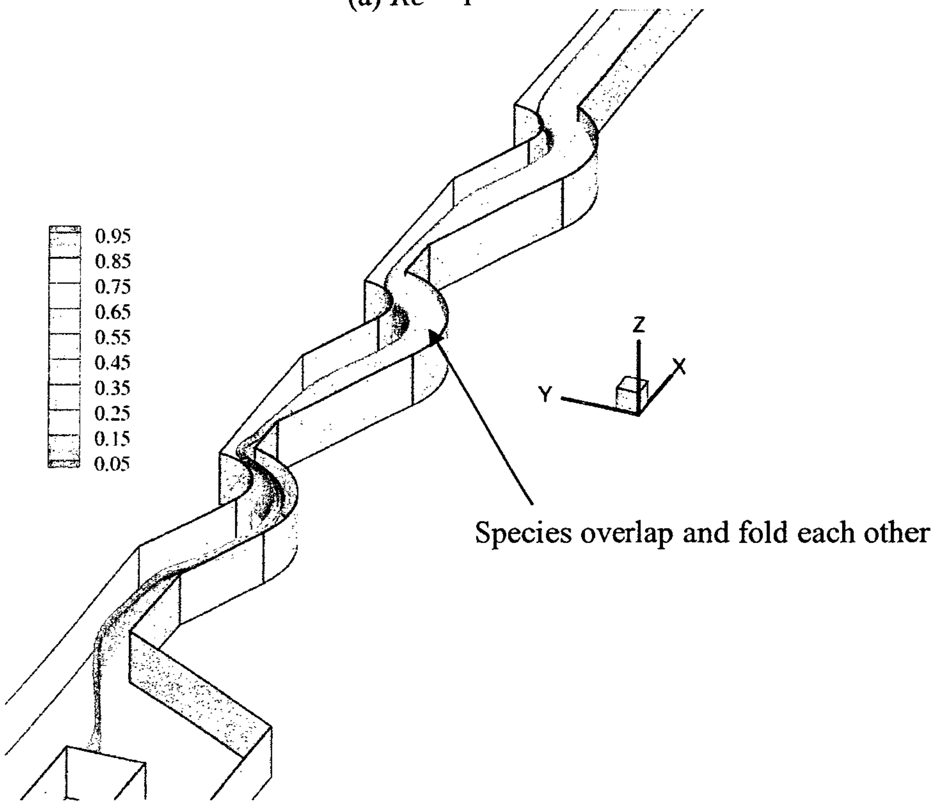

(b) *Re* = 50

Figure 4.11: Iso-surface of concentrations.

side to the outer side due to centrifugal forces. Mixing is enhanced in the circular sectors due to the Dean vortices which twist fluid and increase the contact area. The mixing mechanism becomes a combination of diffusion and convection.

Figure 4.12 shows the mixing efficiency along the mixing length at *Re* = 10. In Fig. 4.12(a), the displacement is kept at 0.25 and the open angles are set to 30°, 45° and 60° for Case 3, Case 17 and Case 18, respectively. The mixing efficiency increases as the opening angle increases. This phenomenon is caused by mass-convection enhancement. With increasing opening angle, the channel radius of curvature decreases, which leads to enhanced Dean vortex. The stirring effect on the flow increases leading to the mass-convection enhancement. Therefore, better mixing could be achieved in the micromixers with larger opening angles. Figure 4.12(b) shows the mixing efficiency under the condition that the opening angle is 60° and displacement is set at -0.25, 0, and 0.25 in Case 3, Case 15 and Case 18, respectively, at *Re* = 10. The difference between Case 3 and Case 15 is not obvious, which shows that the mixing efficiency is not affected by the displacement at $S \leq 0$. The apparent difference is shown in Case 18, indicating that the mixing efficiency is influenced by the displacement at $S \geq 0$. Therefore, the opening angle of 60° and the displacement of 0.25 are chosen as the optimal design dimensions.

4.3 Interdigital Micromixer with Circular-sector

Three mixing elements are applied in the final design. At high *Re*, the Dean vortex could be generated in the circular-sector mixing elements, which is able to achieve better mixing than the straight channel. Six cross-sections in the first cell, as shown in Fig. 4.13, are selected to observe the concentration distributions. Figures 4.14-15 show the concentration distributions at six cross-sections in the first mixing element at *Re* = 5

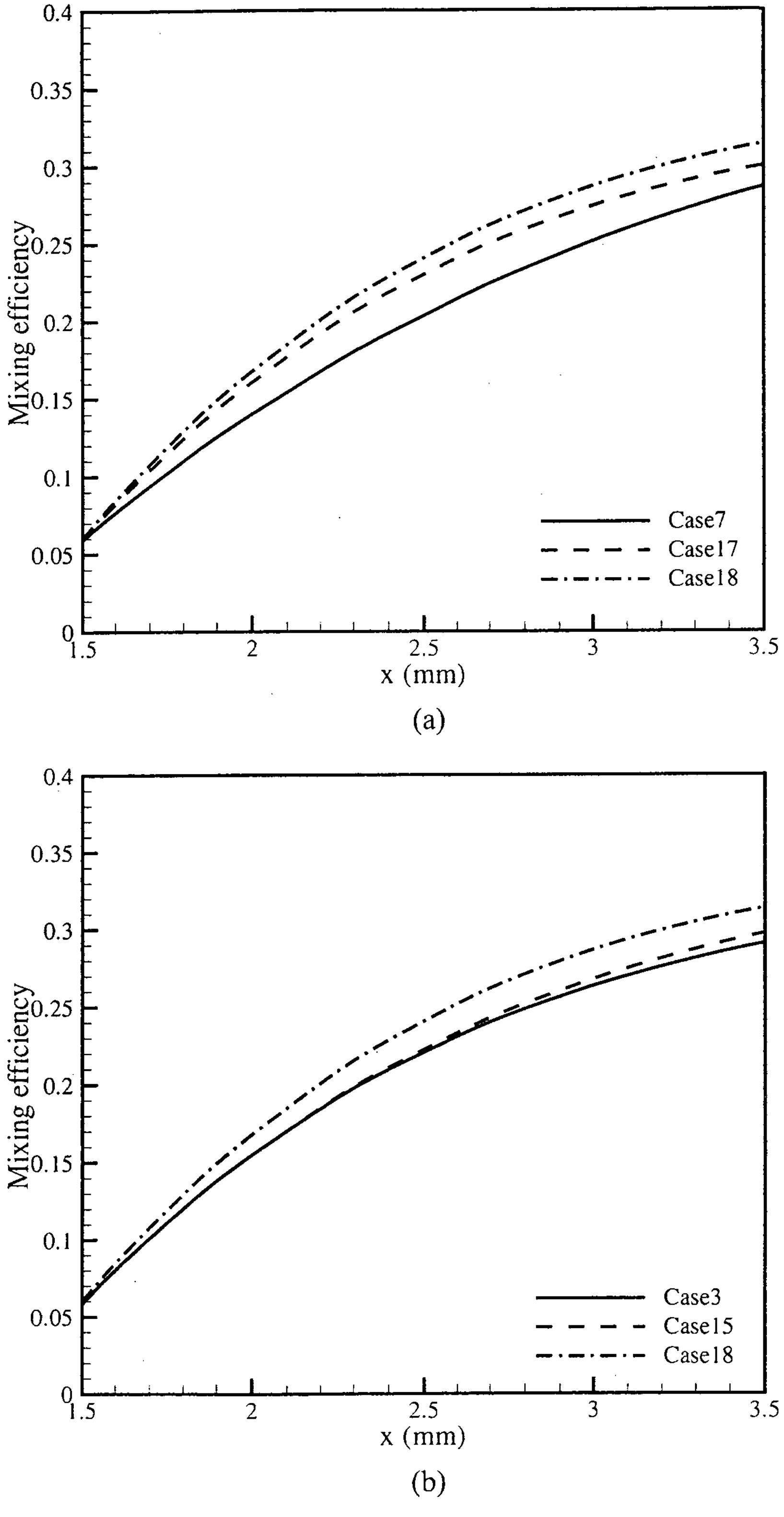

(a)

(b)

Figure 4.12: The mixing efficiency along the mixing length at *Re* = 10.

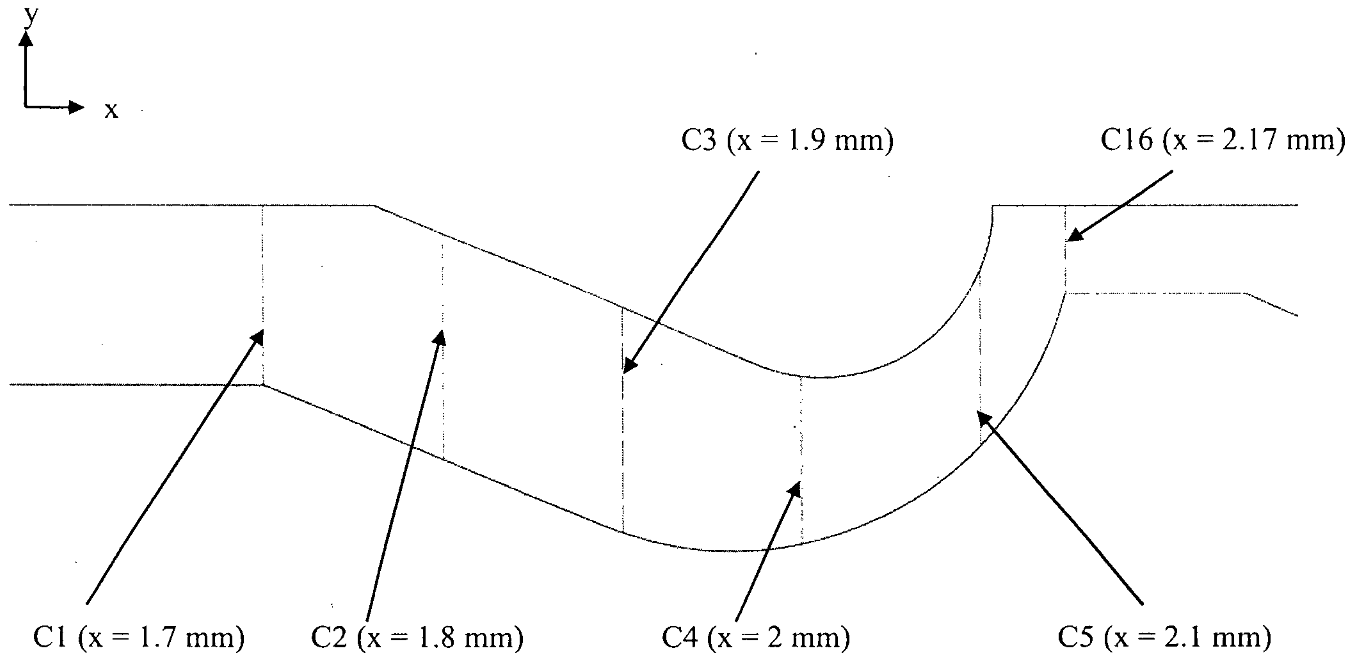

Figure 4.13: Locations of six cross-sections in the first cell.

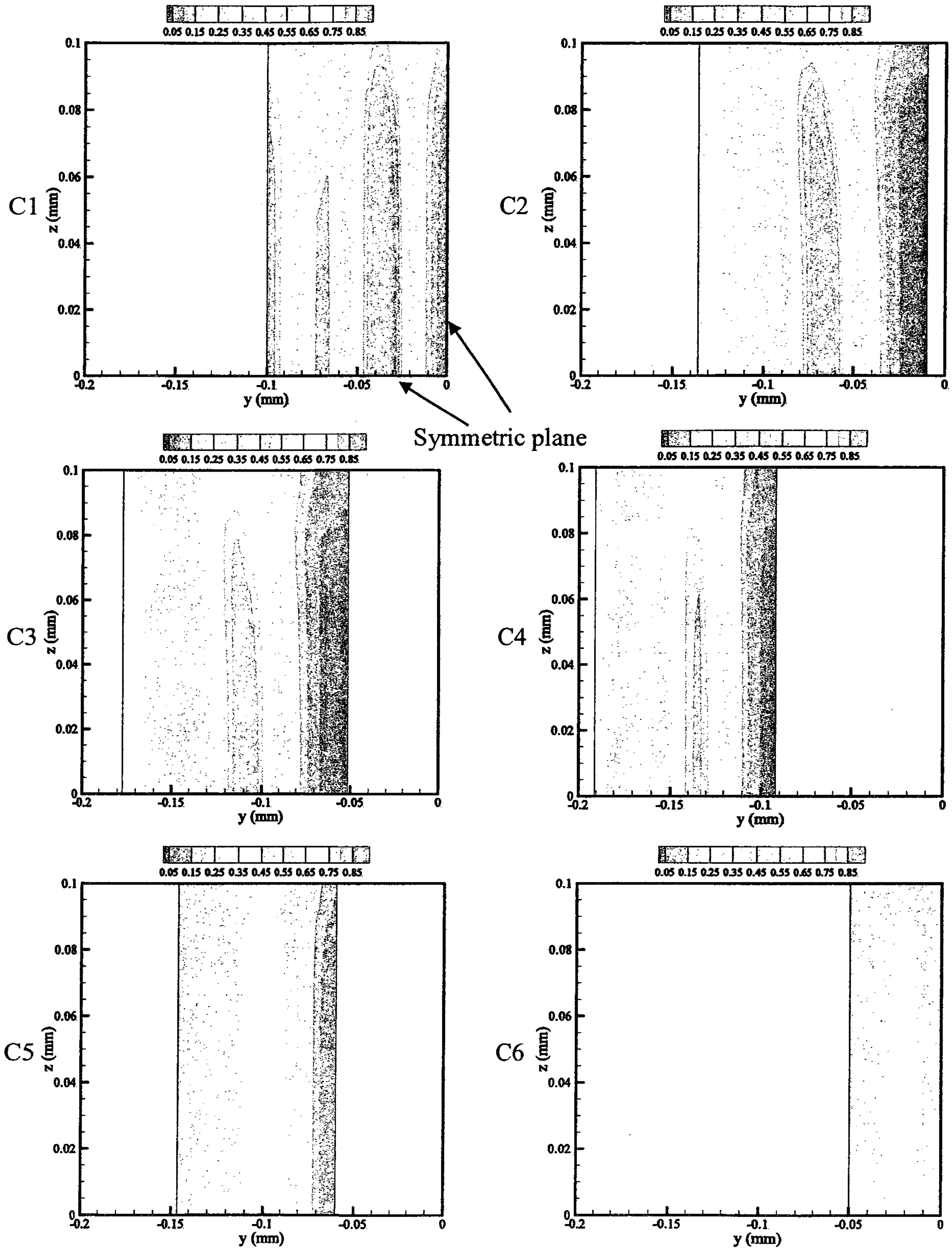

Figure 4.14: Concentration distributions in the six cross-sections at *Re* = 5.

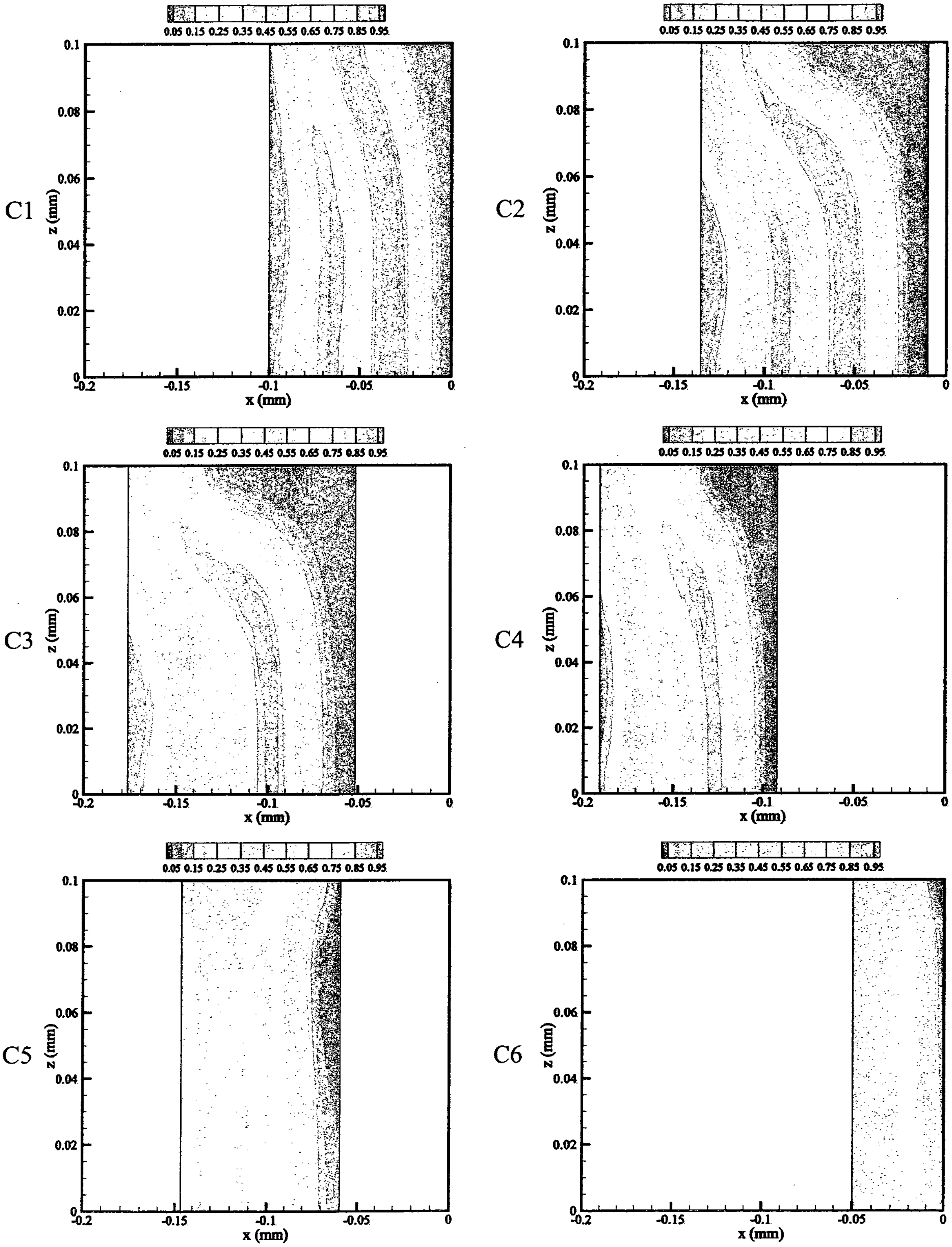

Figure 4.15: Concentration distributions in the six cross-sections at $Re = 50$.

and 50. At all six cross-sections, the interface of species is almost straight at *Re* = 5. The flow is compressed and enters the narrow channel. Since the velocity is small, the Dean vortex could not be generated and viscous forces are dominant. Compared with *Re* = 5, the flow distortion is observed and the interface of species is no longer straight at *Re* = 50. As the velocity increases, the Dean vortex becomes stronger. The flow located in the horizontal symmetric plane has larger velocity since the pressure-driven flow has parabolic velocity distribution, which induces the movement of center flow to the outer wall due to the stronger centrifugal force. At C2 and C3, the flow located at the outer wall is compressed by the flow from the center of the channel and moves up. Then, the flow originally located near the top surface is compressed to the inner wall. Hence, a Dean vortex is created which causes the flow folding observed in the cross-sections of C2 and C3. At C4 and C5, The curvature of channel is changed and the direction of Dean vortex changes to counter-clockwise, which causes the interface to become straight. The mass-convection is enhanced to increase the mixing efficiency.

Figure 4.16 shows the mixing efficiency along the mixing length. The mixing efficiency at $1 \leq Re \leq 100$ could reach larger than 70% within one mixing element. After three mixing elements, the present micromixer could obtain more than 85% mixing efficiency. Figure 4.17 shows the mixing efficiency and pressure drop of the optimal design. The mixing efficiency decreases at $1 \leq Re \leq 30$, which is caused by the reduced residual time as *Re* increases. The effect of the vortex is less than the effect of diffusion.

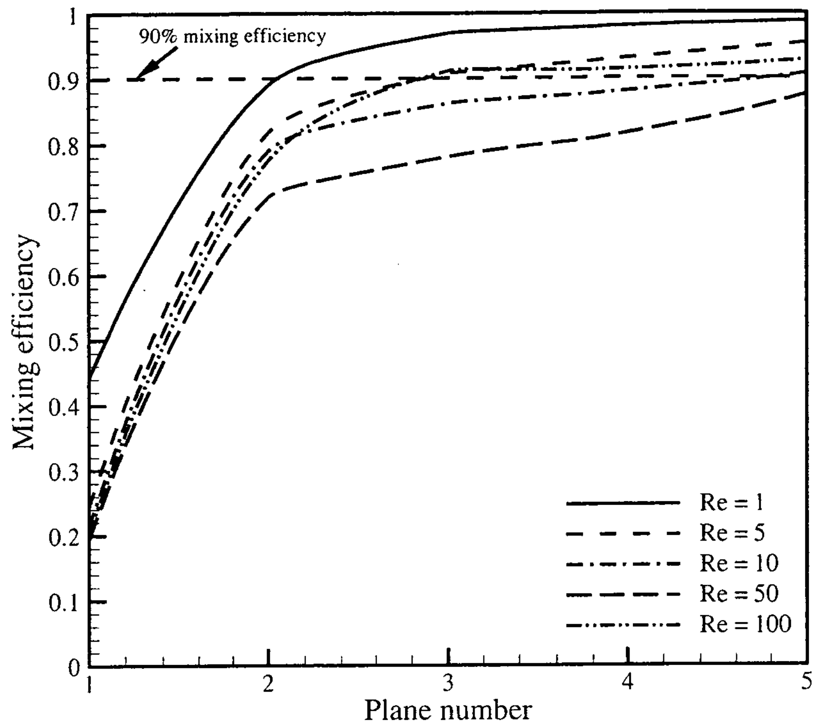

Figure 4.16: The mixing efficiency of optimal design along the mixing length at $1 \le Re \le 100$.

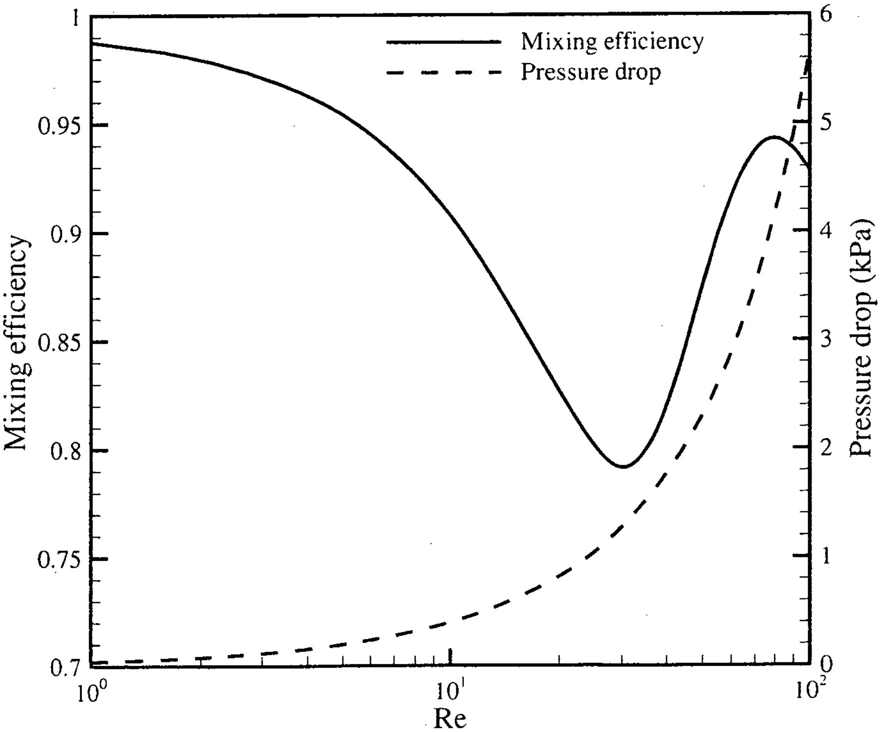

Figure 4.17: The mixing efficiency and pressure drop of optimal design at $1 \le Re \le 100$.

Diffusion is the dominant mixing mechanism at $1 \leq Re \leq 30$. At $Re \geq 30$, the effect of the vortex becomes the dominant mechanism. Even if the diffusion time is reduced, the contact area is increased and the flow stretching and folding are enhanced by the vortex. The final mixing affected by both mechanisms increases. At $Re \geq 80$, the mixing efficiency decreases again, which means the extremely reduced residual time leads to a sharp decrease in mass-diffusion. The mass-diffusion becomes the dominant mixing mechanism again. In summary, $Re = 30$ marks the transition from diffusion-dominance to convection-dominance. The minimum mixing efficiency is approximately 79%. The IC micromixer has the potential to achieve good mixing with low pressure drop within a short mixing length.

4.4 Summary

Throughout this chapter, a modified planar passive micromixer, the IC micromixer, is investigated by numerical simulation. The interdigital inlet and circular-sector mixing element are applied. The simulation results show that the layout of the interdigital substreams influences the mixing efficiency. Then uneven interdigital inlet is designed in order to reduce the diffusion path near the side walls. The high mixing efficiency and low pressure drop could be observed compared to the uniform substream channel width. Hence, the uneven interdigital inlet is determined to be optimal and applied to the micromixer. The DOE methodology is used to optimize the mixing element. The displacement and opening angle have a significant effect on the mixing. The combination of the uneven interdigital inlet and the optimal mixing element is applied as the optimal design. The results show that the mixing efficiency could be improved to more than 75% at $1 \leq Re \leq 100$ within the mixing length of 5 mm. The IC micromixer achieves better mixing efficiency compared to the CO micromixer.

Chapter 5

Interdigital-Obstacle Micromixer

Since the minimum mixing efficiency of the IC micromixer is approximate 79%, it could not achieve good mixing over a wide range. An Interdigital-Obstacle micromixer is designed and tested by numerical simulation. The circular-section obstacles are placed in the straight channel and the interface of flow fluctuates among the gaps of obstacles, which induces the enhancement of mass-convection. The optimization is also performed in order to determine the best design dimensions. At the end of this chapter, the hybrid micromixer, denoted as the ICO micromixer, is designed to combine the advantages of the IC and IO micromixers.

5.1 Design of Interdigital-Obstacle Micromixer

The IC micromixer introduced in the previous section applies split-and-recombine and Dean vortices principles to achieve high mixing quality. The lowest mixing efficiency of 79% occurs at *Re* = 30. In order to acquire high mixing efficiency or increase the lower limit of mixing efficiency, a new micromixer is proposed and is denoted as "IO", which represents the interdigital-obstacle micromixer. The circular-sector obstacles are placed in the straight microchannel and the interdigital structure is recommended as the inlet, as explained in the previous section. In order to

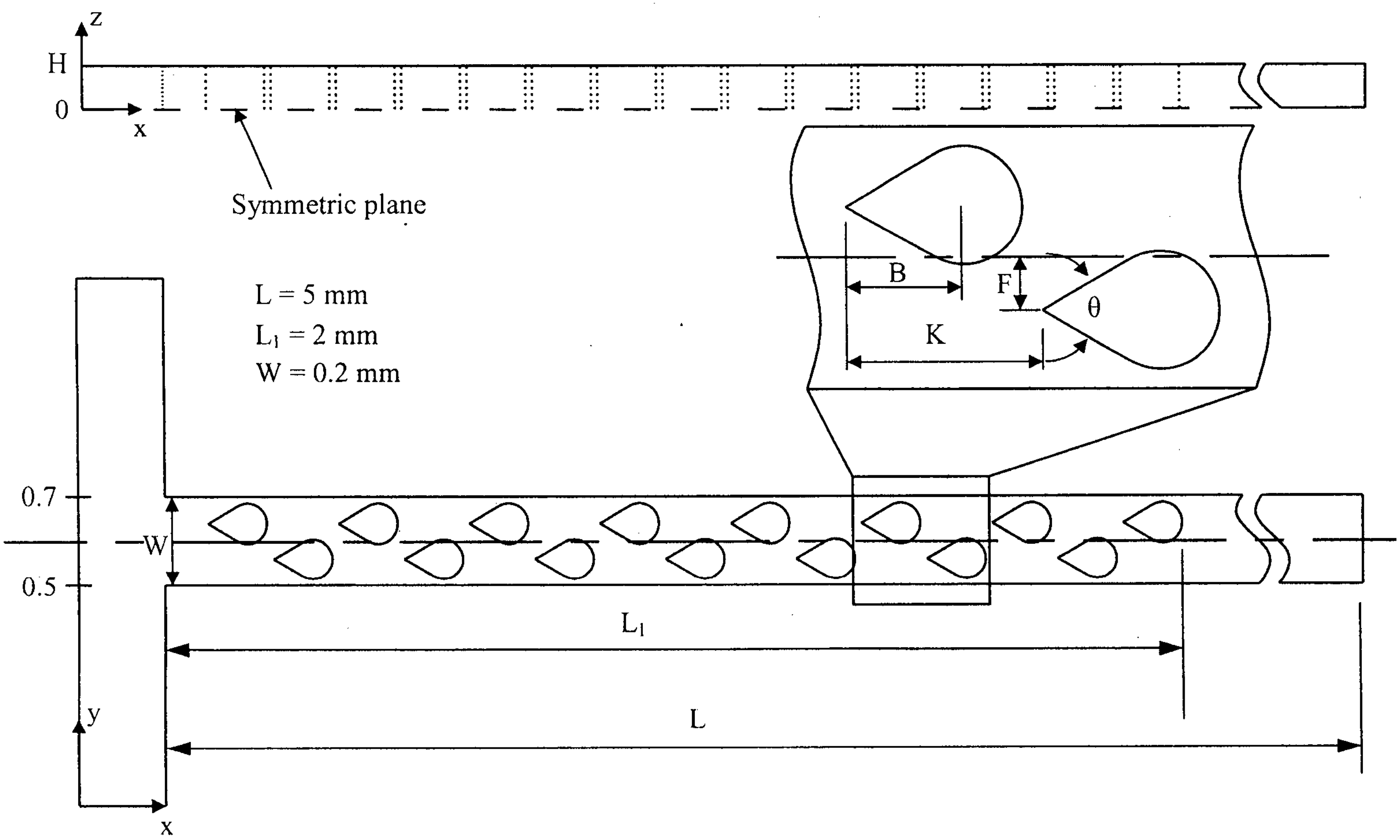

Figure 5.1: Schematic of the micromixer with obstacles (units in mm).

clearly trace the interface, the T-shaped inlet is applied to investigate the effect of the mixing element on the mixing. The schematic is shown in Fig. 5.1. The tested Reynolds numbers are calculated at the entrance of the downstream channel. The two species flow through the gap of adjacent obstacles and the meander-like interface could be caused by the obstacles in order to enlarge the mixing length. The cross-section of two inlets is 0.3 mm × 0.2 mm. The total length of micromixer L is fixed at 5 mm. The length of the microchannel containing obstacles, L_1, is fixed at 2 mm.

5.2 Numerical Simulation

The simulation method of the IO micromixer is the same as that used for the IC micromixer. A half model is meshed due to the symmetric structure. Grid independence is performed prior to the investigation. Figure 5.2 shows the velocity and concentration distributions at the intersection of the symmetric plane and exit. The results show that there is no obvious change with the grid number after 0.5 M grids. Hence, the grid number of 0.5 M is selected for the further investigations.

5.3 Optimization of Mixing Element

Since the interdigital inlet has been investigated in the previous section, only the mixing element is optimized in this section. The T-shaped is applied in order to observe the mixing process clearly. The DOE methodology is applied and five design parameters are selected to achieve the optimization. These five parameters are the offset (F), the

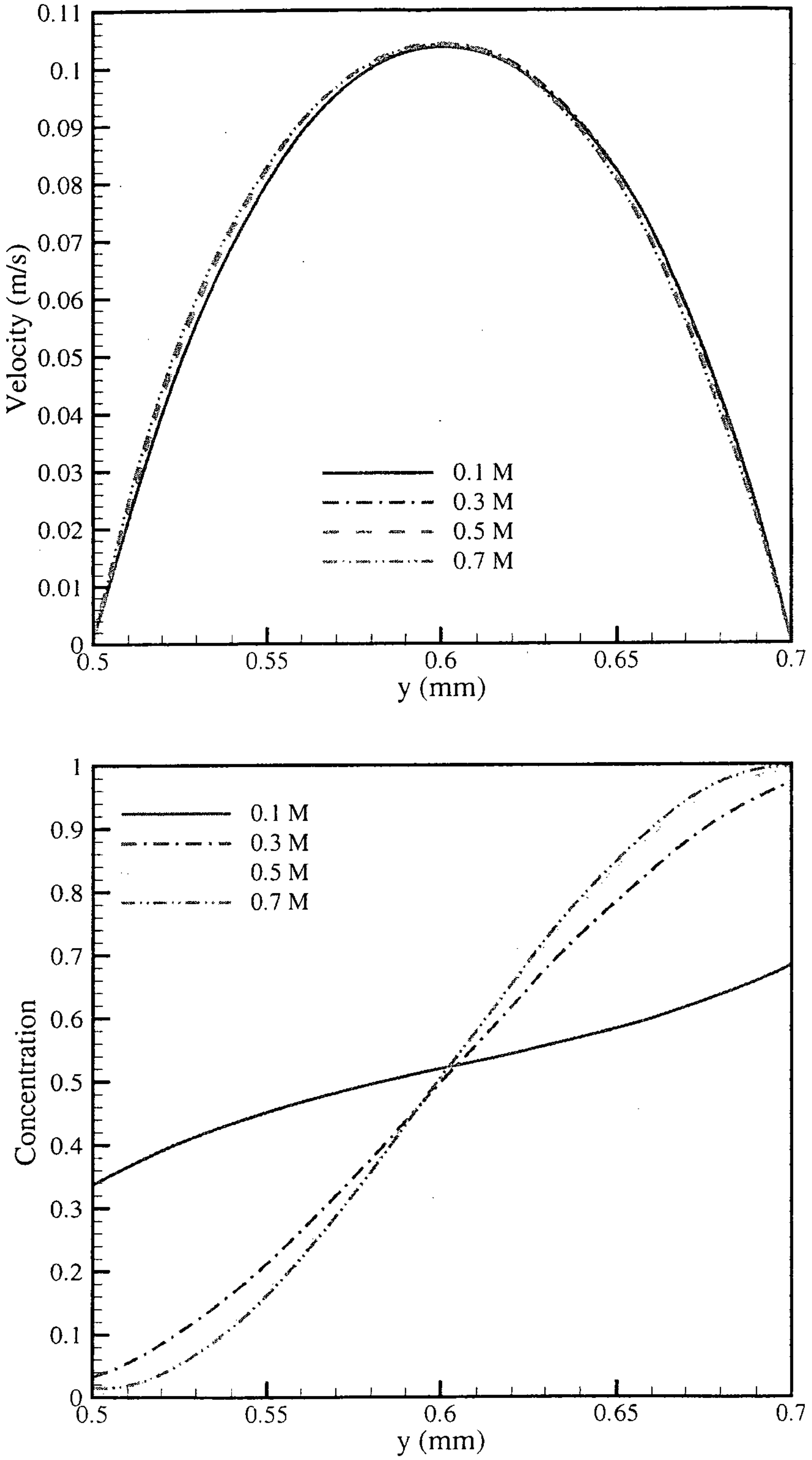

Figure 5.2: Velocity and concentration distributions at the intersection of the symmetric plane and exit.

displacement (K), the opening angle (θ), the obstacle length (B), and the depth of the microchannel (H). The Taguchi method is applied to classify the sensitivities of design parameters. The mixing efficiency is selected as the objective function. The ranges of design parameters are listed in Tab. 5.1. Three levels are selected for each design parameter and the orthogonal array L_{18} is built using the Taguchi method, as shown in Tab. 5.2. The mixing efficiency and pressure drop for the eighteen cases are listed in Tab. 5.3, and the average S/N for each parameter is calculated, as shown in Tab. 5.4. Figure 5.3 shows the average S/N for each parameter at *Re* = 10. The offset and obstacle length have the largest influence on the mixing efficiency, and the opening angle and the depth of the channel have the second most important effect on the mixing efficiency. However, the displacement of obstacles has a small influence. Considering the effect of design parameters on the mixing efficiency and the calculation task, three design parameters, the offset, the obstacle length and the opening angle, are selected to achieve further optimization. The displacement and the depth of the channel are selected as 0.5 and 0.75, respectively. A new test matrix is built in Tab. 5.5. Since three design parameters are selected in the present optimization, RSM methodology, called Box-Behnken, is applied for the optimization of three parameters. The response testing matrix and results are listed in Tab. 5.6. According to the second order response model of three design parameters, the response equation is represented as:

$$y = \beta_0 + \beta_1 x_1 + \beta_2 x_2 + \beta_3 x_3 + \beta_{12} x_1 x_2 + \beta_{13} x_1 x_3 + \beta_{23} x_2 x_3 + \beta_{11} x_1^2 + \beta_{22} x_2^2 + \beta_{33} x_3^2 \quad (5.1)$$

Table 5.1: Design parameters and levels used in optimization

Levels	Parameters				
	A(F/W)	B(K/W)	C(θ)	D(B/W)	E(H/W)
1	0.2	0.5	30°	0.25	0.5
2	0.15	0.75	45°	0.35	0.75
3	0.1	1	60°	0.45	1

Table 5.2: Orthogonal array L_{18} (design matrix)

Case	Parameters				
	A	B	C	D	E
1	1	1	1	1	1
2	1	2	2	2	2
3	1	3	3	3	3
4	2	1	1	2	2
5	2	2	2	3	3
6	2	3	3	1	1
7	3	1	2	1	3
8	3	2	3	2	1
9	3	3	1	3	2
10	1	1	3	3	2
11	1	2	1	1	3
12	1	3	2	2	1
13	2	1	2	3	1
14	2	2	3	1	2
15	2	3	1	2	3
16	3	1	3	2	3
17	3	2	1	3	1
18	3	3	2	1	2

Table 5.3: The S/N and mixing efficiency of eighteen cases

Case	σ	S/N	Mixing efficiency	Pressure drop (Pa)
1	0.442	7.082	0.115	761
2	0.415	7.637	0.154	474
3	0.384	8.323	0.187	402
4	0.441	7.114	0.115	521
5	0.393	8.110	0.166	517
6	0.438	7.175	0.125	722
7	0.445	7.036	0.108	333
8	0.430	7.333	0.140	1043
9	0.436	7.215	0.123	400
10	0.284	10.944	0.367	3660
11	0.433	7.267	0.123	230
12	0.432	7.281	0.135	744
13	0.438	7.175	0.124	1872
14	0.424	7.459	0.141	438
15	0.359	8.900	0.292	4396
16	0.450	6.937	0.132	666
17	0.444	7.043	0.111	849
18	0.441	7.105	0.115	345

Table 5.4: The average S/N of each of the eighteen design parameters

Parameter	Average S/N (dB)
A1	8.089
A2	7.656
A3	7.112
B1	7.715
B2	7.475
B3	7.667
C1	7.437
C2	7.391
C3	8.029
D1	7.187
D2	7.534
D3	8.135
E1	7.182
E2	7.912
E3	7.762

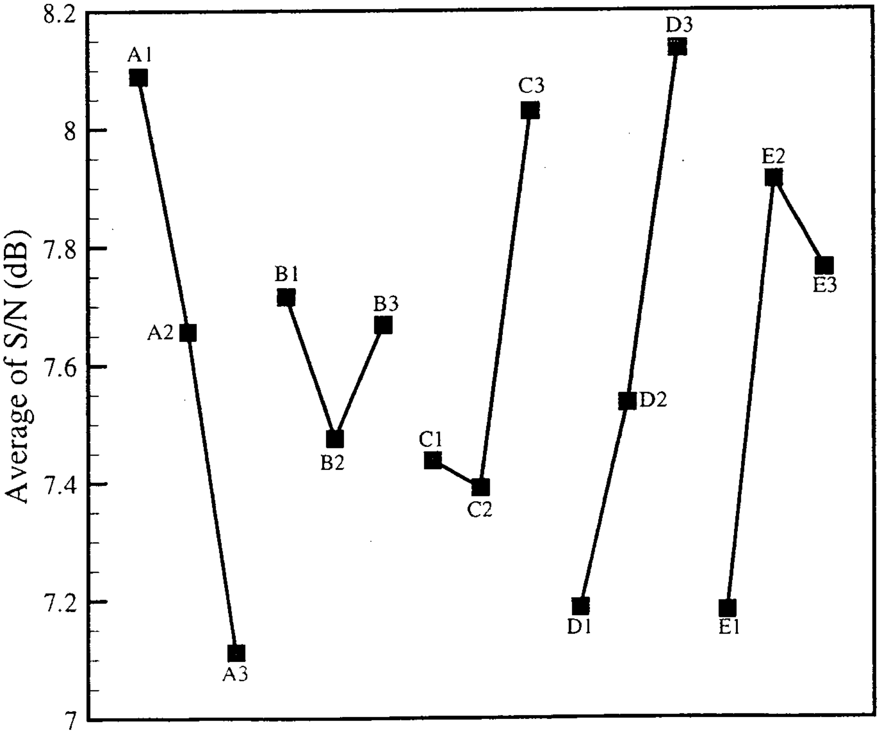

Figure 5.3: The average S/N for each design parameter at *Re* = 10.

Table 5.5: The design parameters used for the response surface model

Design parameter		lower	center	upper
Coded variable (x)		-1	0	1
Natural variables	F/W (ξ_1)	0.1	0.15	0.2
	B/W (ξ_2)	0.25	0.35	0.45
	θ (ξ_3)	30°	45°	60°

Table 5.6: The tested matrix and response of response surface model

Case	Natural variables			Coded variables			Response
	ξ_1	ξ_2	ξ_3	x_1	x_2	x_3	y
19	0.1	0.25	45°	-1	-1	0	0.1058
20	0.1	0.45	45°	-1	1	0	0.1331
21	0.2	0.25	45°	1	-1	0	0.1300
22	0.2	0.45	45°	1	1	0	0.1923
23	0.1	0.35	30°	-1	0	-1	0.1134
24	0.1	0.35	60°	-1	0	1	0.1377
25	0.2	0.35	30°	1	0	-1	0.1279
26	0.2	0.35	60°	1	0	1	0.2485
27	0.15	0.25	30°	0	-1	-1	0.1133
28	0.15	0.25	60°	0	-1	1	0.1264
29	0.15	0.45	30°	0	1	-1	0.1096
30	0.15	0.45	60°	0	1	1	0.1991
31	0.15	0.35	45°	0	0	0	0.1163

Table 5.7: Coefficients of response model

Coefficient	Value
β_0	1.163E-01
β_1	2.607E-02
β_2	1.982E-02
β_3	3.095E-02
β_{12}	8.737E-03
β_{13}	2.408E-02
β_{23}	1.910E-02
β_{11}	2.190E-02
β_{22}	2.100E-03
β_{33}	1.871E-02

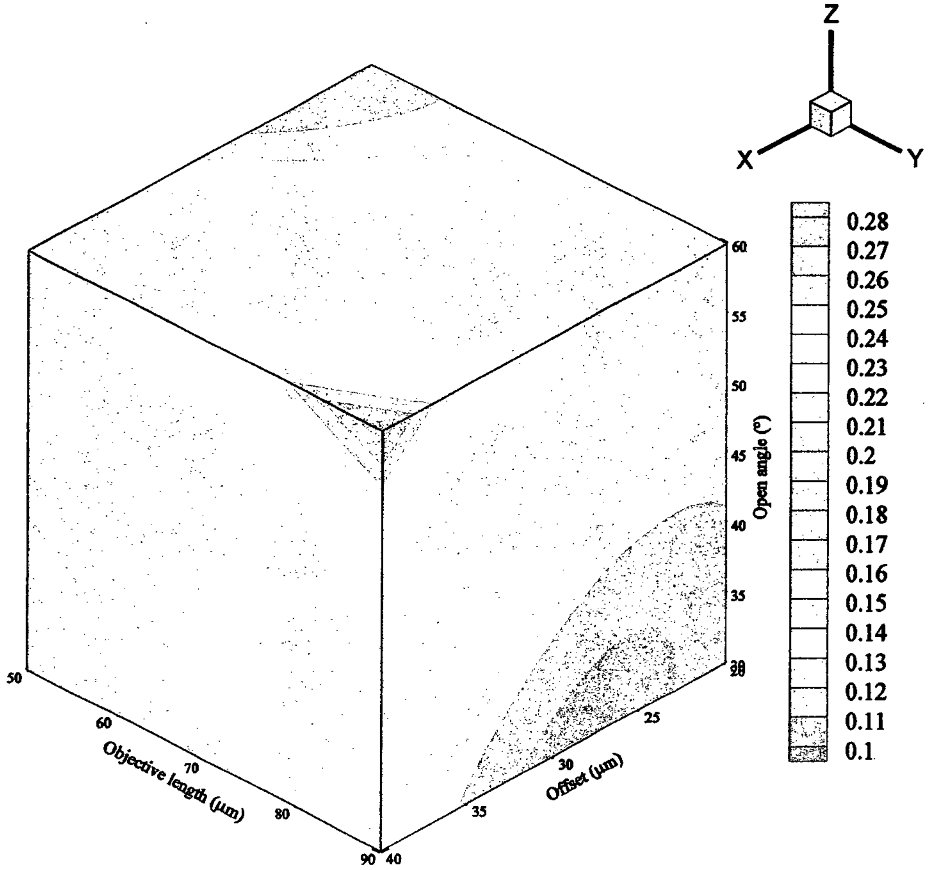

Figure 5.4: Response box colored by the objective function value at *Re* = 10.

Variance and regression analyses are done to measure the uncertainty in the set of coefficients of the polynomial function. From the results of analyses for the response surface, the coefficient of multiple determinations, R^2, is determined to be 97.8%, and the adjusted coefficient of multiple determinations, R_{adj}^2, is determined to be 97.1%. Both coefficients are larger than 90%. The response values are considered to be accurately predicted by the response surface model. Figure 5.4 shows the response box colored by the objective function. The results show that the optimal point (offset, obstacle length, opening angle) is located at (0.2, 0.45, 60°), corresponding to (40 μm, 90 μm, 60°).

In order to investigate the effect of each design parameter on the mixing, two design parameters are kept uniform and the third one is varied from the lower to upper limit. The advection-diffusion equation is analyzed to assist in understanding the mixing process in order to explain the mixing phenomenon. Under steady-state conditions, the advection-diffusion equation contains six components: advection and diffusion in the x, y and z directions. It follows that:

$$V_x \frac{\partial C}{\partial x} + V_y \frac{\partial C}{\partial y} + V_z \frac{\partial C}{\partial z} = D\left(\frac{\partial^2 C}{\partial x^2} + \frac{\partial^2 C}{\partial y^2} + \frac{\partial^2 C}{\partial z^2}\right) \tag{5.2}$$

where V_x, V_y, and V_z are the velocity vectors in x, y and z directions, respectively, C is the concentration, and D is the natural diffusion of the species. The advection items are $V_x \frac{\partial C}{\partial x} + V_y \frac{\partial C}{\partial y} + V_z \frac{\partial C}{\partial z}$ and the diffusion items are $D\frac{\partial^2 C}{\partial x^2} + D\frac{\partial^2 C}{\partial y^2} + D\frac{\partial^2 C}{\partial z^2}$ in the x, y and z directions respectively. When the velocity direction is perpendicular to the diffusion direction (concentration gradient), the advection has no effect on mixing since the advection item is equal to zero. At low Reynolds numbers, the flow creeps through the obstacles. Since the velocity is very small, the terms of advection are small, which represents a weak advection effect. The mixing performance is not affected by the advection. Diffusion is the dominant mixing mechanism, and mixing is mainly dependent on the mixing time and contact area between the two species. As the Reynolds number increases, the effect of diffusion on mixing tends to decrease due to the reduced mixing time. However, compared to the reduced effect of mass-diffusion on the mixing, mass-advection becomes stronger since the velocity increases.

The opening angle is first investigated. The offset and obstacle length are kept at 40 μm and 90 μm, respectively. The opening angle is selected to be 30°, 45° and 60°. Three more cases are designed to do the analysis of parameters on the mixing. These three cases are named Case 32 (40 μm, 90 μm, 30°), Case 33 (30 μm, 90 μm, 45°) and Case 34 (40 μm, 50 μm, 60°). Figures 5.5 and 5.6 show the contours of optimal design and Case 32 in the symmetric plane, respectively. The opening angles are 60° and 30° in the optimal design and Case 32, respectively. The mixing performance of the optimal design is obviously better than that of Case 32. Since the mixing time (residual time) is the same in both cases, the difference is caused by the effect of mass-advection. In the optimal design, the two species enter the domain among the obstacles. The meander-like path could be

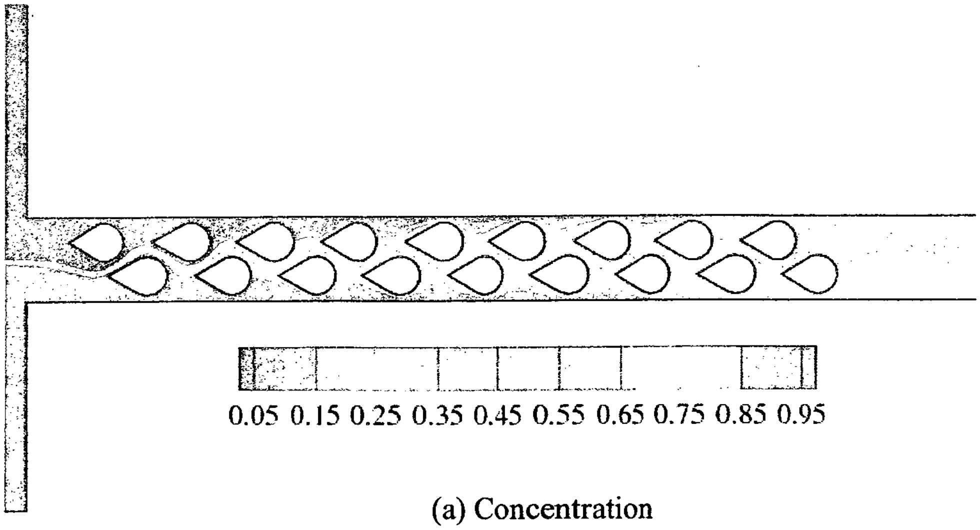

(a) Concentration

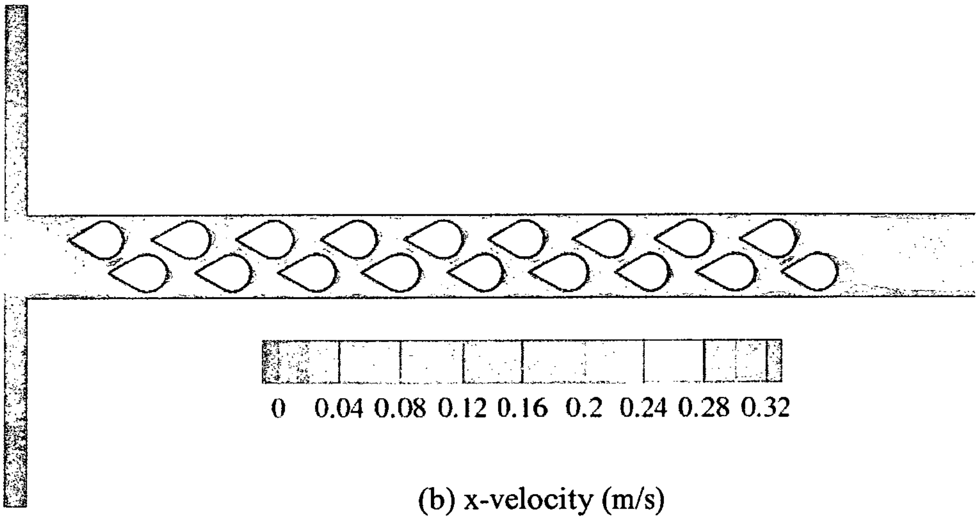

(b) x-velocity (m/s)

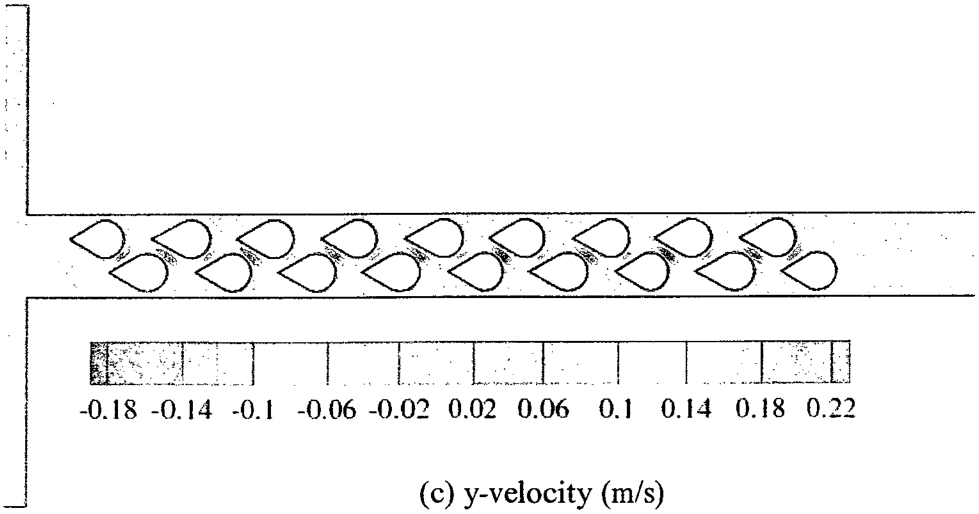

(c) y-velocity (m/s)

Figure 5.5: Contours of optimal design at *Re* = 10.

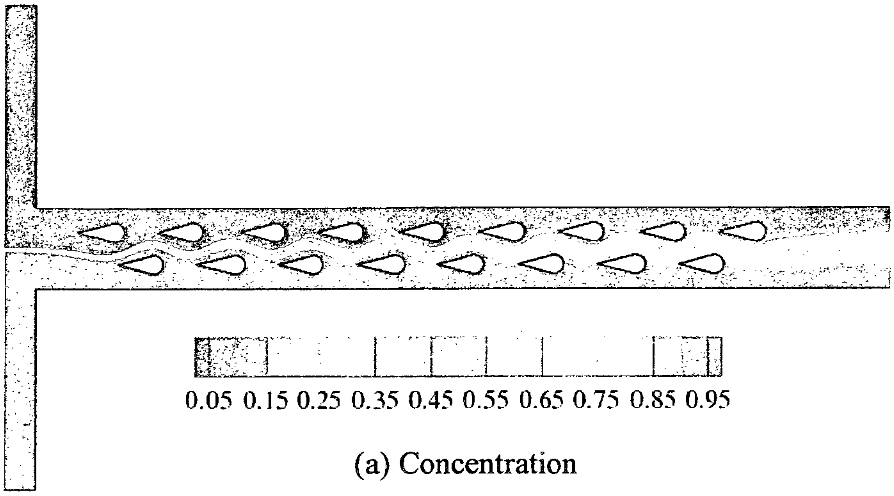

(a) Concentration

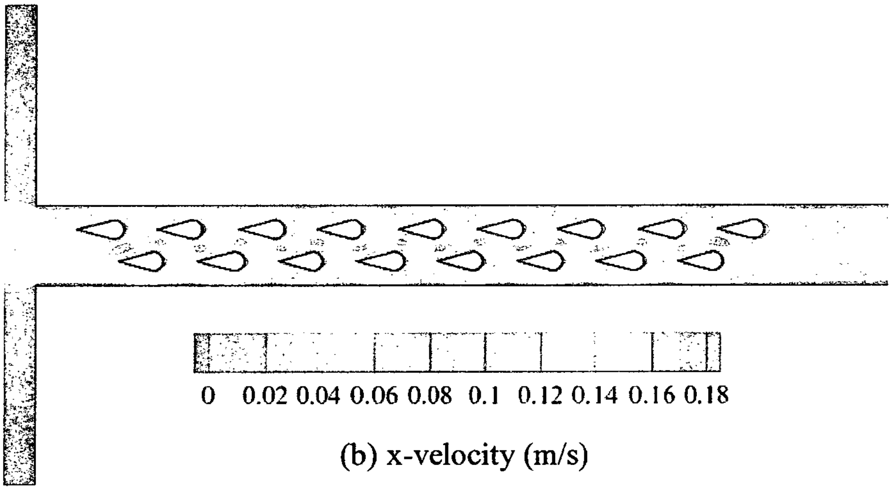

(b) x-velocity (m/s)

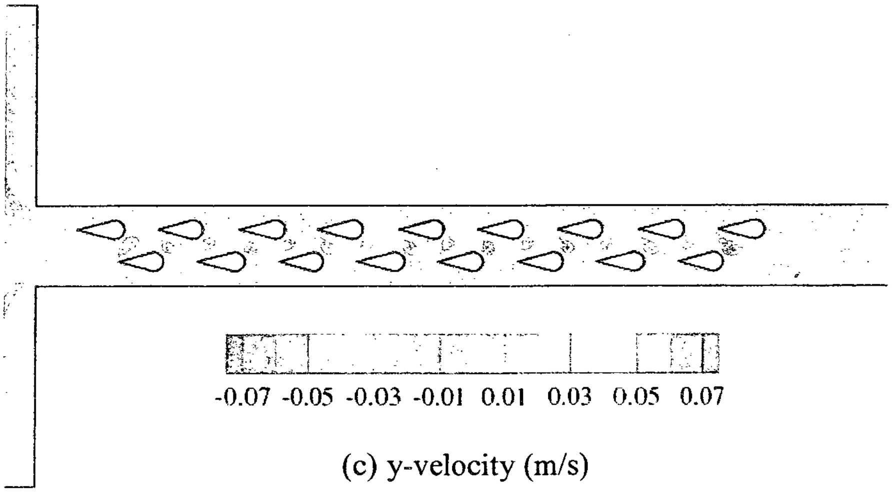

(c) y-velocity (m/s)

Figure 5.6: Contours of Case 32 at $Re = 10$.

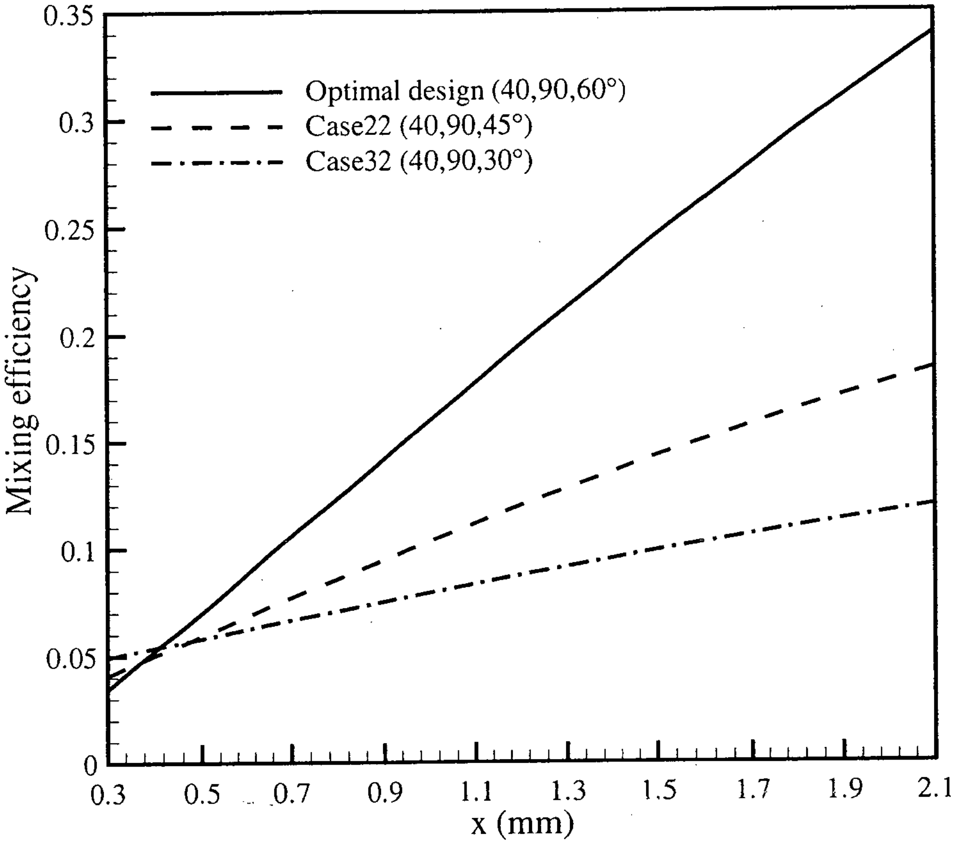

Figure 5.7: The mixing efficiency along the mixing length at *Re* = 10 used to investigate the effect of opening angle on mixing performance.

observed, which generates the transverse motion. The species pass through the obstacles in Case 32 more smoothly than in the optimal design because of the larger space among the obstacles. Due to the larger opening angle, a larger y-velocity occurs at the location of interface in the optimal design than Case 32. The larger effect of advection caused by the y velocity in the optimal design leads to better mixing efficiency. Figure 5.7 shows the mixing efficiency along the mixing length for three cases at *Re* = 10. The mixing efficiency increases as the opening angle increases since mass-advection is enhanced by the larger opening angle.

Figure 5.8 shows the contours of concentration, x-velocity, and y-velocity in Case 34 at *Re* = 10. The offset and opening angle are the same as the optimal design. The obstacle length is set at 50 μm. Similar phenomenon may be observed. The large space among the obstacles leads to smaller transverse motion. Mass-advection is reduced as the obstacle length increases. Also, the large space results in a long diffusion path, which is propitious to the mass-diffusion process. Figure 5.9 shows the mixing efficiency along the mixing length at *Re* = 10. The mixing efficiency increases with decreasing obstacle length since shorter obstacles create smaller transverse motion.

Figure 5.10 and 5.11 show the contours of Case 22 and 20, respectively. In these two cases, the obstacle length and the opening angle are kept at 70 μm and 45°, respectively. The offset of both cases are set at 40 μm and 20 μm, respectively. Since the distance of obstacles in Case 20 is very small, the flow characteristics are different from those observed in Case 22. In Case 22, the interface is located among the obstacles. The meander-like path could be observed, which accelerates mass-advection. However, the flow is cut into two portions due to the small space among the obstacles in Case 20. The transverse motion of flow occurs near the side. Figure 5.12 shows the mixing efficiency along the mixing length at *Re* = 10 for three cases to investigate the effect of offset on the mixing. As the offset increases, the mixing efficiency increases since the mixing occurs among the obstacles and transverse motion occurs at the same location, which enhances mass-advection. It is worth noting that Case 20 has better mixing efficiency than Case 22 and Case 33 over the first eleven obstacles. Eight cross-sections are selected along the mixing length to investigate the phenomenon, as shown in Fig. 5.13. Figure 5.14 shows the concentration distributions of eight cross-sections for Case 20 at *Re* = 10. The concentration gradient is shown on both the left and right sides. As shown in Fig. 5.11, the y-velocity is small and could not generate efficient mass-convection. Since the velocity near the top surface is smaller than at the center of channel ($z = 0$), the species near the top surface have more adequate time to get mixed, which induces better mixing near the top surface than at the center. Figure 5.15 shows the concentration distributions in Case 22. The difference in the mixing process between two cases could be seen. In Case 22, mixing mainly occurs among the gaps of obstacles. The large velocity at the center of the channels leads to the efficient mass-advection, which accelerates the mixing in the center. In summary, the mixing in Case 20 is mainly dependent on diffusion. Along

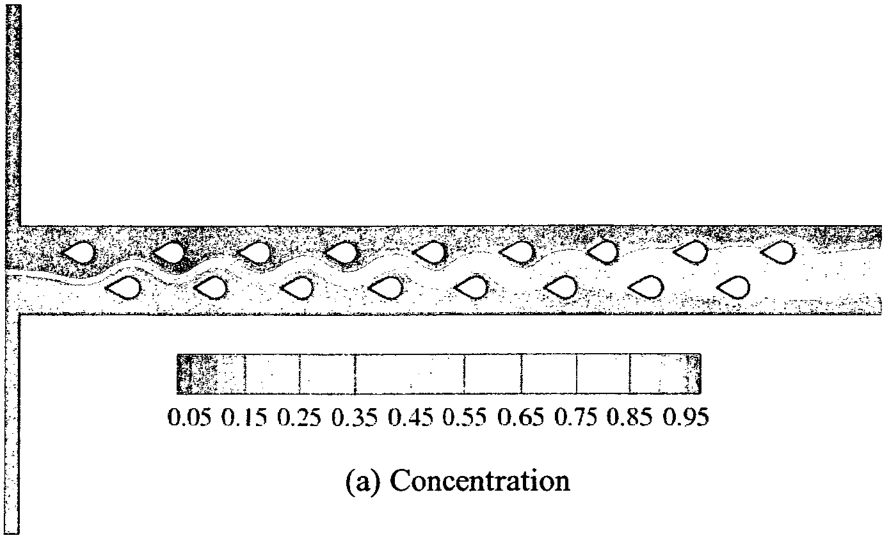

(a) Concentration

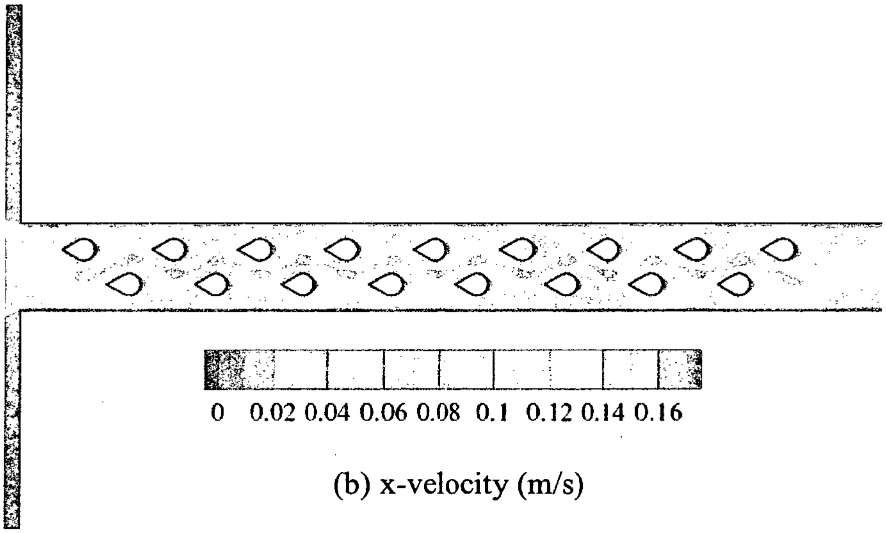

(b) x-velocity (m/s)

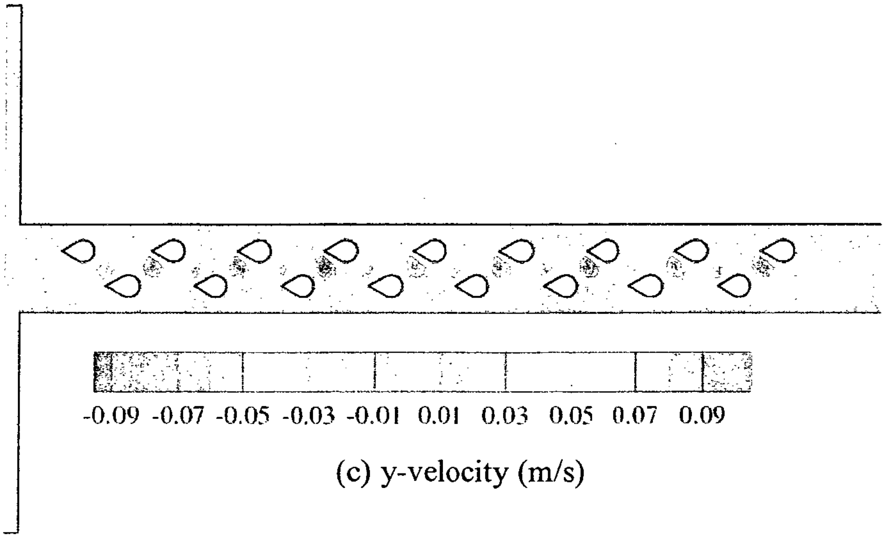

(c) y-velocity (m/s)

Figure 5.8: Contours of Case 34 at *Re* = 10.

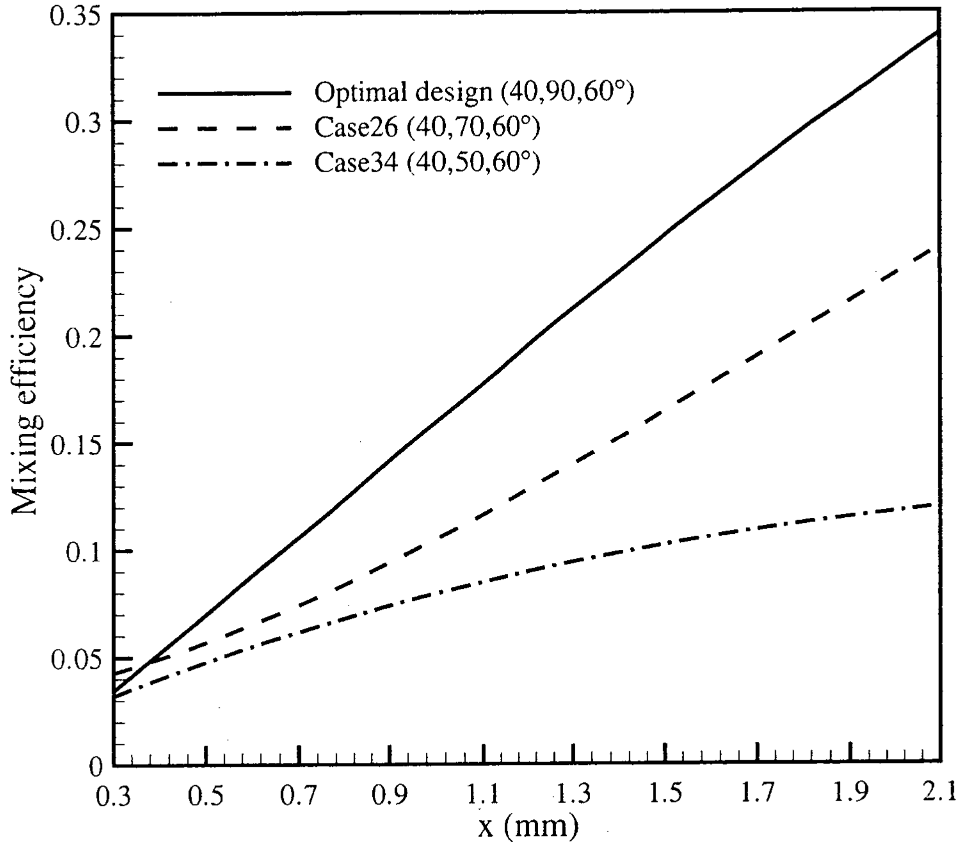

Figure 5.9: The mixing efficiency along the mixing length at $Re = 10$ used to investigate the effect of obstacle length on the mixing performance.

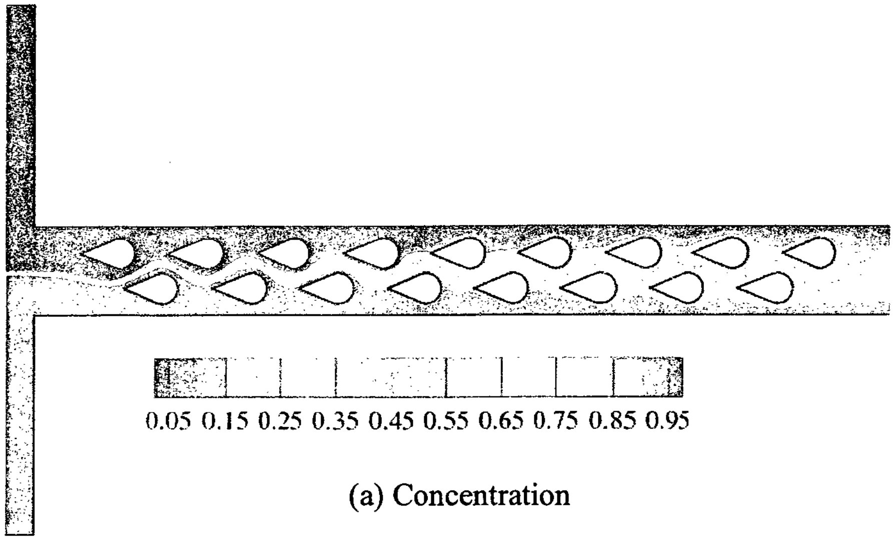

(a) Concentration

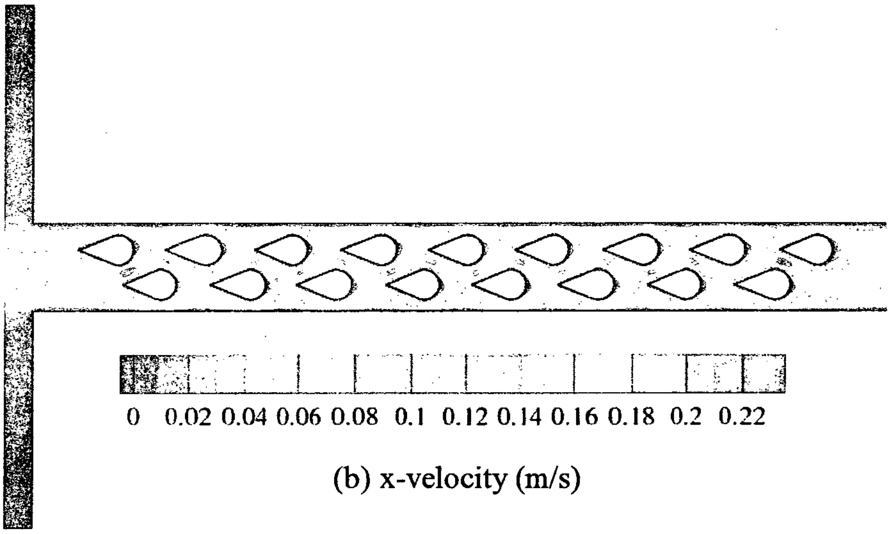

(b) x-velocity (m/s)

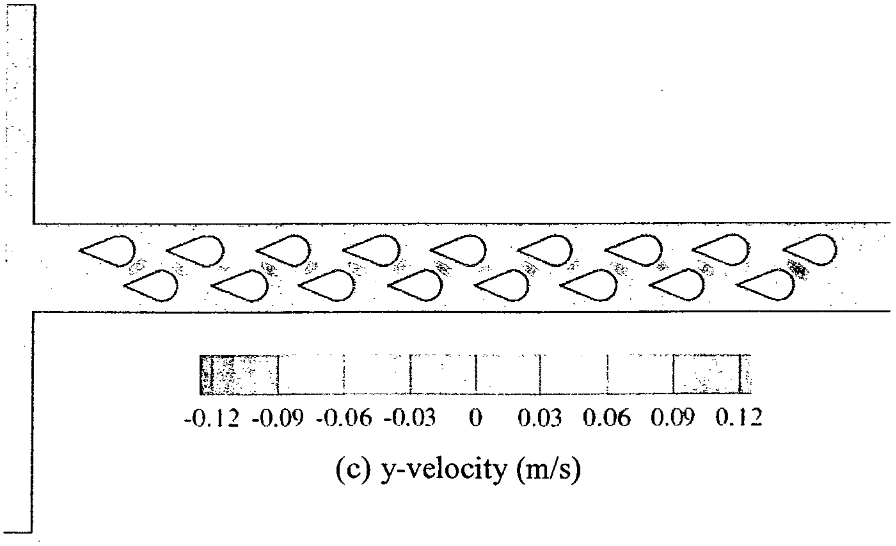

(c) y-velocity (m/s)

Figure 5.10: Contours of Case 22 at *Re* = 10.

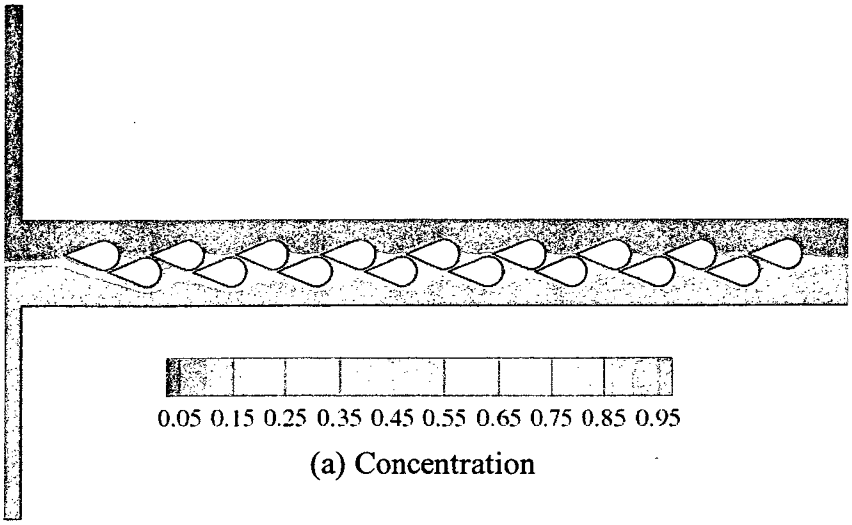

(a) Concentration

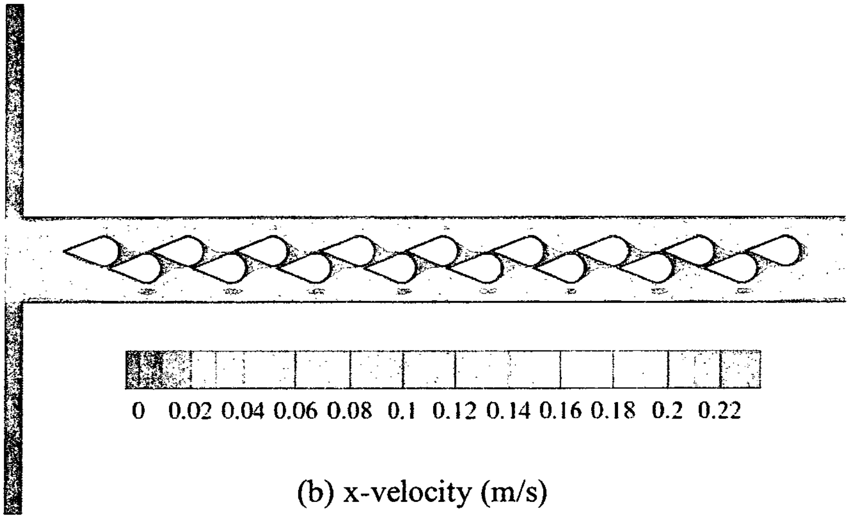

(b) x-velocity (m/s)

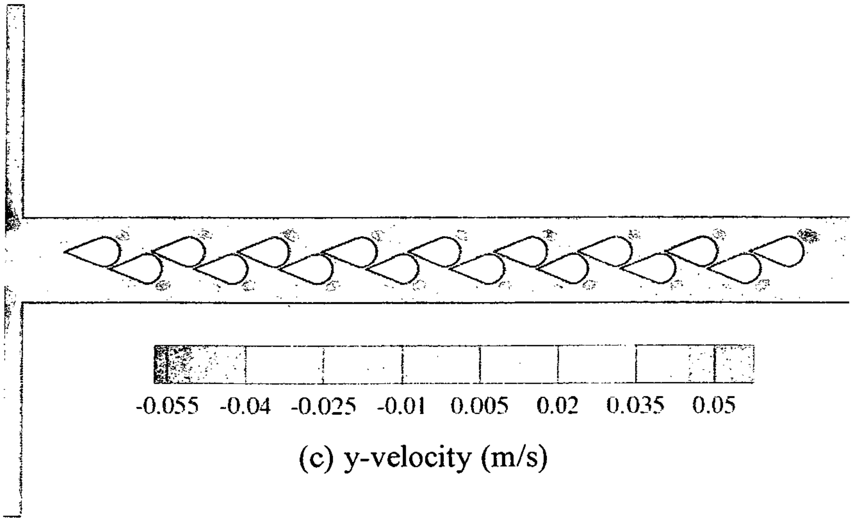

(c) y-velocity (m/s)

Figure 5.11: Contours of Case 20 at *Re* = 10.

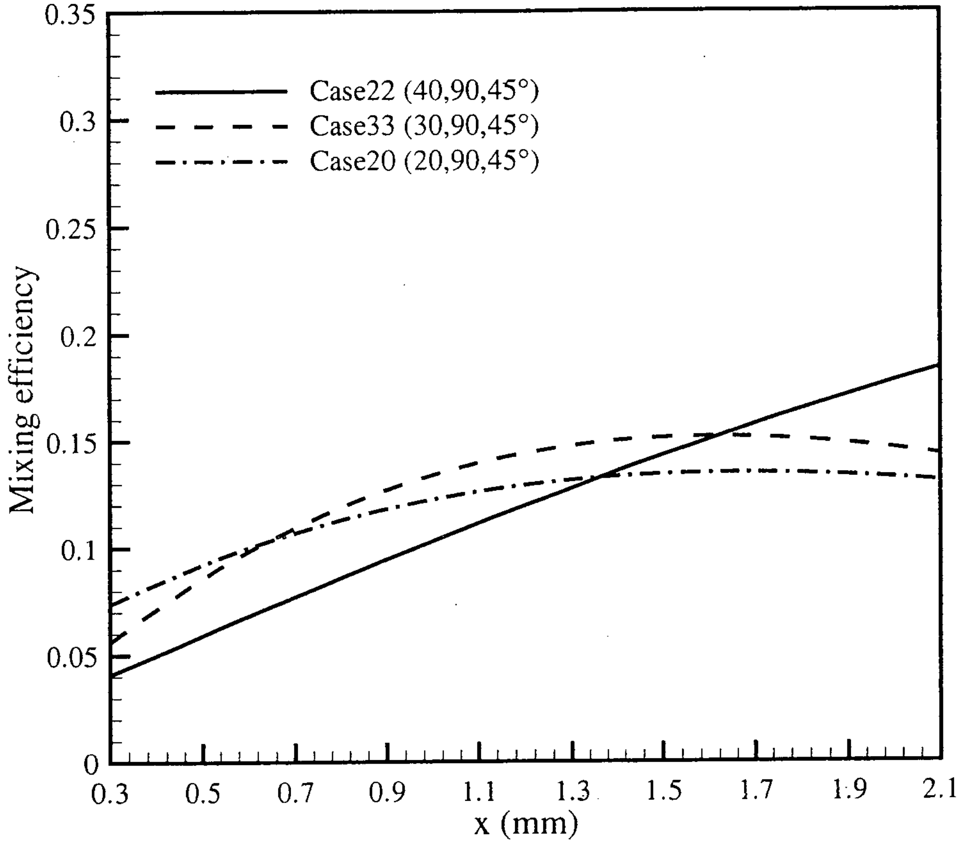

Figure 5.12: The mixing efficiency along the mixing length at *Re* = 10 used to investigate the effect of offset on the mixing performance.

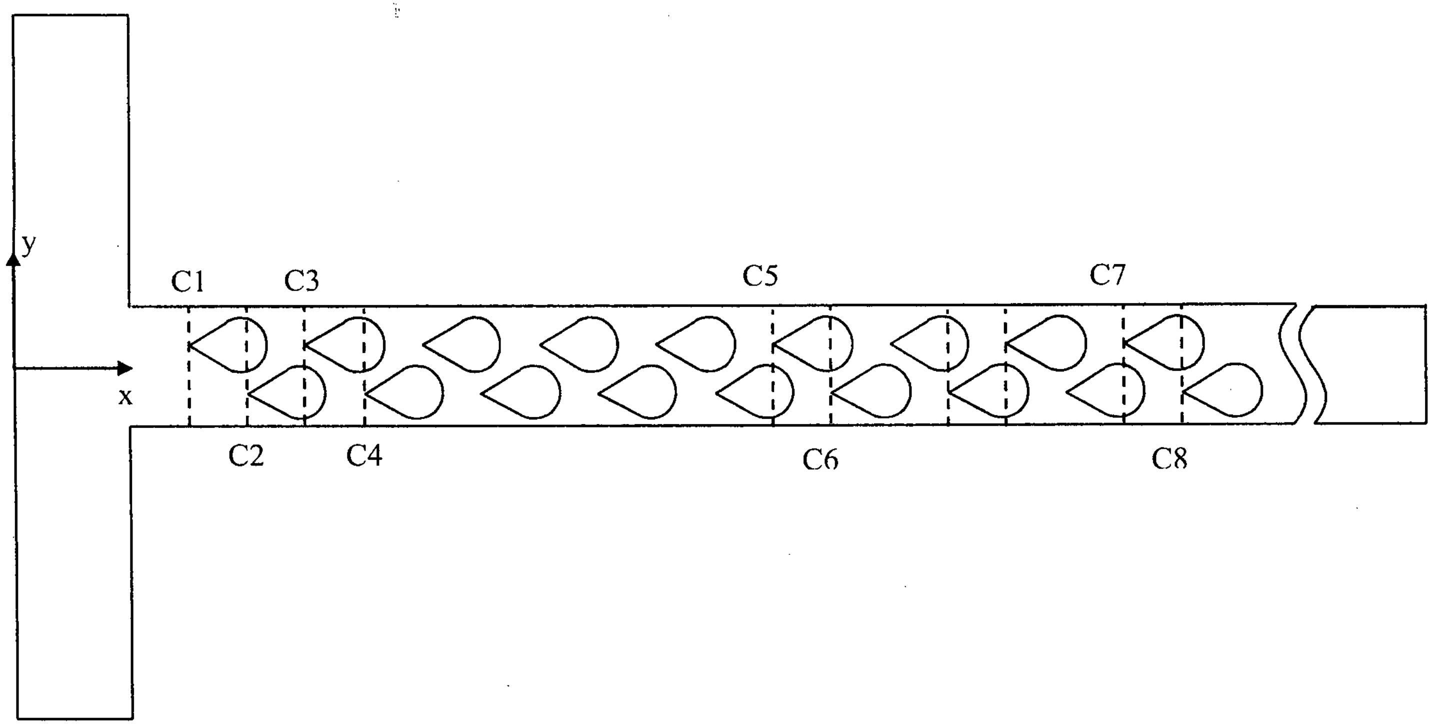

Figure 5.13: Eight cross-sections along the mixing length selected for the investigation of the mixing process.

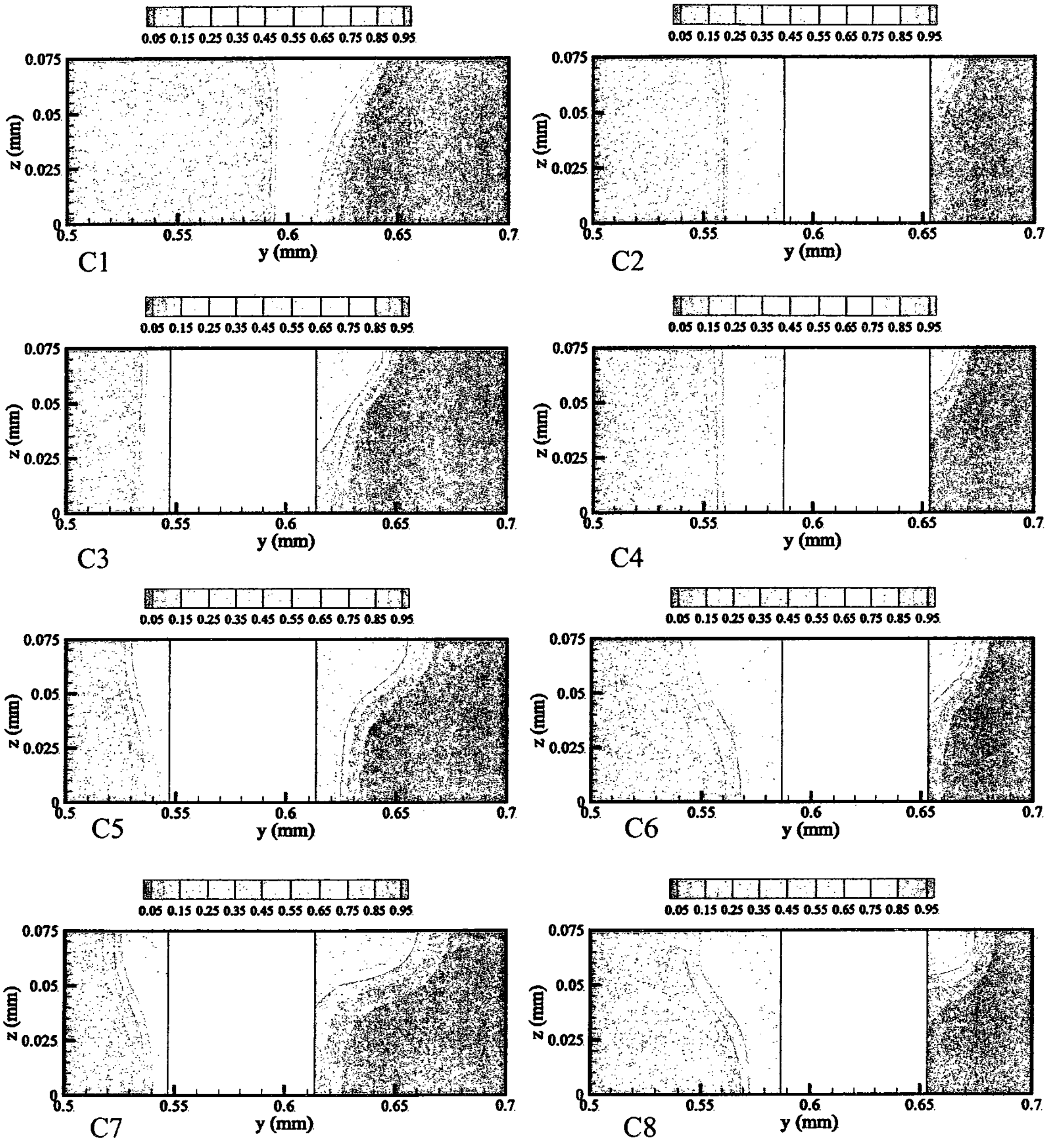

Figure 5.14: Concentration distributions at eight cross-sections along the mixing length for Case 20 at *Re* = 10.

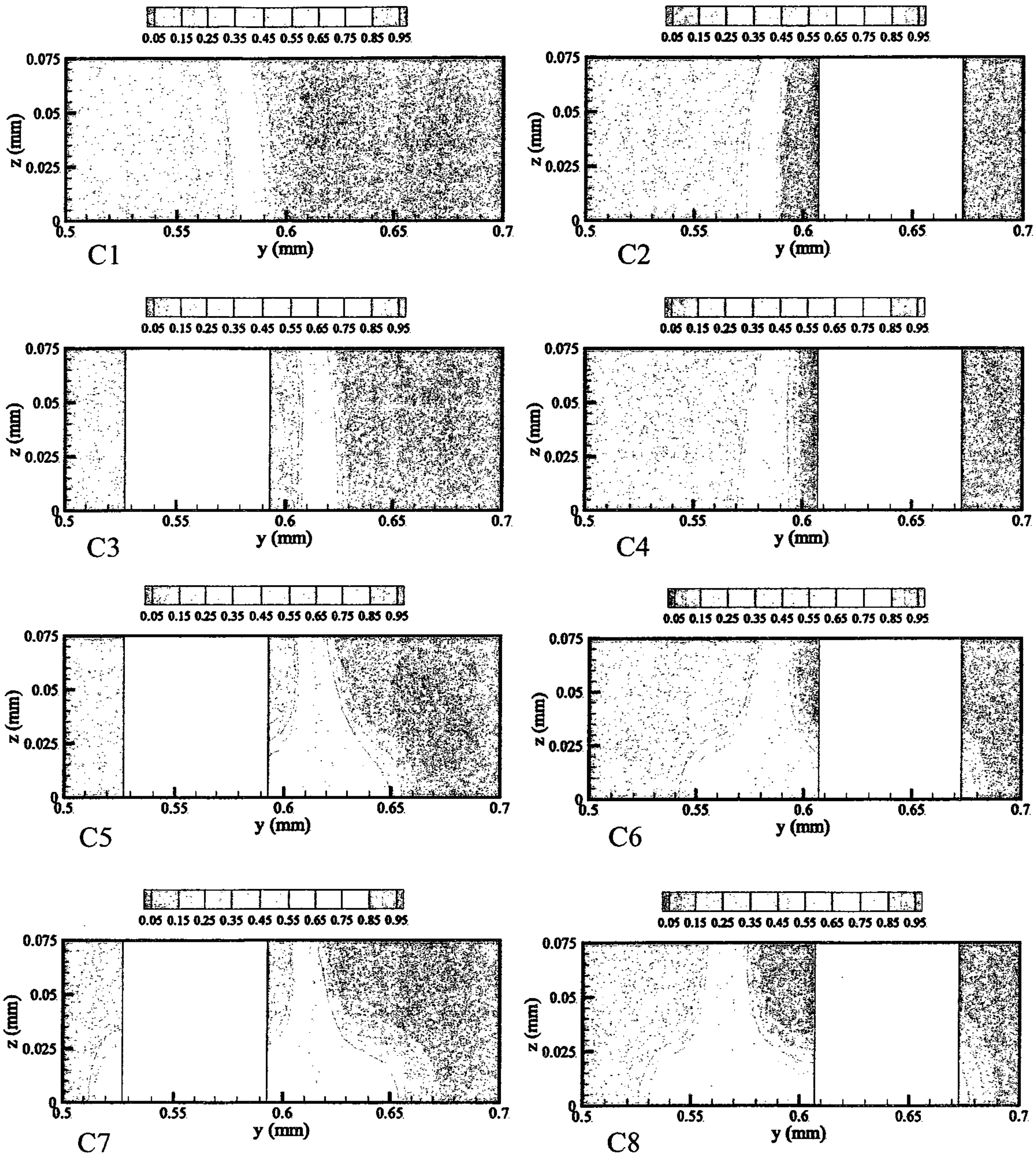

Figure 5.15: Concentration distributions at eight cross-sections along the mixing length in Case 22 at $Re = 10$.

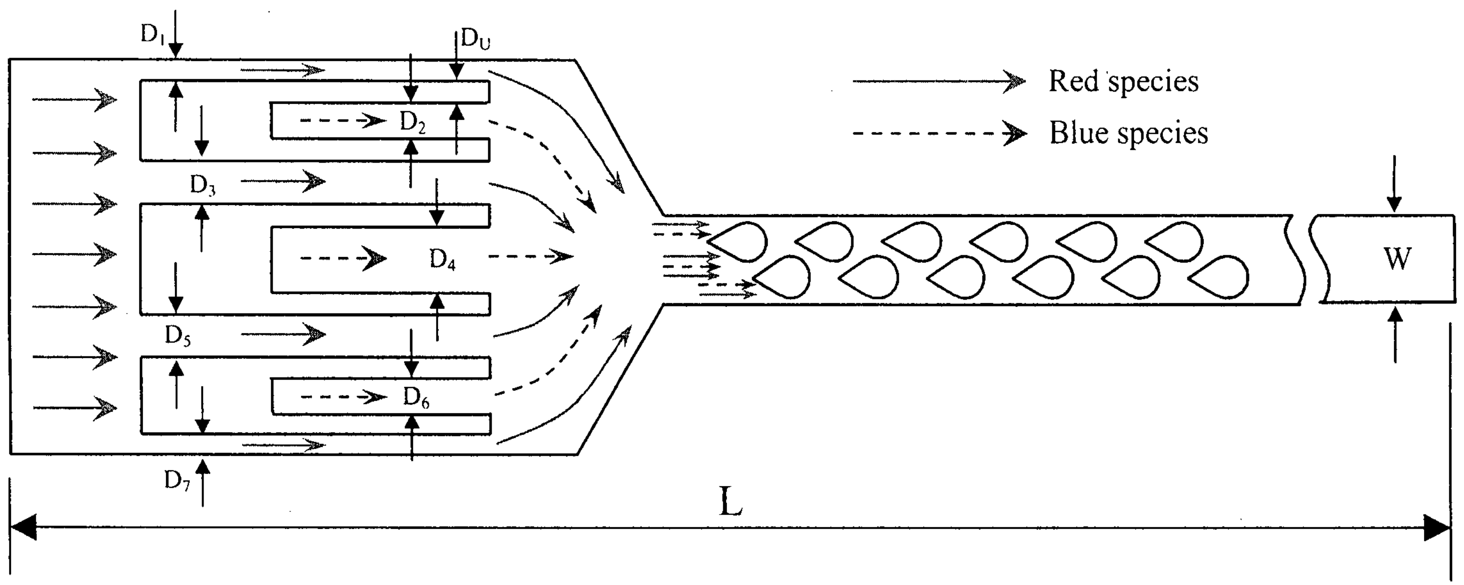

Figure 5.16: Schematic of the IO micromixer.

with the mixing length, the concentration gradient becomes small, and the mixing speed is reduced. However, mass-advection is the key mixing mechanism in Case 22, and maintains fast mixing in the channel. In Case 20, before C5, diffusion causes more efficient mixing than does advection since the species between the gaps of obstacles take a longer time to mix than in Case 22 judging from Fig. 5.10(b) and 5.11(b). Hence, the mixing efficiency in Case 20 is higher than Case 22 before C5.

5.4 Optimal Design with Interdigital Inlet

The interdigital inlet is applied to the optimal obstacle design. The structure of the interdigital structure remains the same as the one selected in the previous section, as shown in Figure 5.16. The purpose of the interdigital-inlet application is to reduce the diffusion path. The range of Reynolds numbers varies from 1 to 100. Figure 5.17 shows the mixing efficiency along the mixing length in the final design. The mixing process along the mixing length is almost the same at $5 \leq Re \leq 100$ and differences are observed at $Re = 1$. At $x \geq 2.4$ mm, the mixing efficiency is beyond 90% in the tested range of Reynolds numbers. The mixing efficiency and pressure drop of the final design is shown in Fig. 5.18. The mixing efficiency almost reaches beyond 95% at $1 \leq Re \leq 100$. However, the mixing efficiency decreases at $1 \leq Re \leq 5$, increases at $5 \leq Re \leq 30$, and decreases again at $30 \leq Re \leq 100$. This is caused by the change in mixing mechanism. At $Re \leq 5$, mixing is dependent on mass-diffusion. As Re increases, the mixing time is reduced and the flow does not have adequate time to achieve good mixing. After *Re* becomes larger than 5, mass-advection takes the dominant role in mixing. Although the diffusion time is shortened, the combined effects of mass-diffusion and mass-advection still produce increasing mixing efficiency. At $Re \geq 30$, the diffusion time is extremely lessened. Mass-diffusion is once again the main mixing mechanism, which induces decreased mixing efficiency. The mixing efficiency of the IO micromixer is larger than 95%, which is expected. However, the pressure drop is larger than 20 kPa at $Re \geq 50$. Hence, the IO micromixer is suitable for applications at $Re \leq 50$.

5.5 Interdigital-Circular-Obstacle Micromixer

Considering the high pressure drop in the IO micromixer and low mixing efficiency in the IC micromixer, a hybrid micromixer, denoted as ICO micromixer, is developed. Figure 5.19 shows the schematic of the ICO micromixer. It combines two IC mixing elements and eight circular-section obstacles. The total mixing length is kept the same as the IC and IO micromixers, and the depth of microchannel is fixed at 0.2 mm. Figure 5.20 shows the comparison of the three micromixers proposed in this study. The mixing efficiency of the ICO micromixer is almost the same as the IO micromixer, but the pressure drop is lower than the IO micromixer. Although the pressure drop of the ICO micromixer is higher than the IC micromixer, better mixing efficiency could be observed at $1 \leq Re \leq 100$ for the ICO micromixer. Hence the ICO micromixer effectively reduces

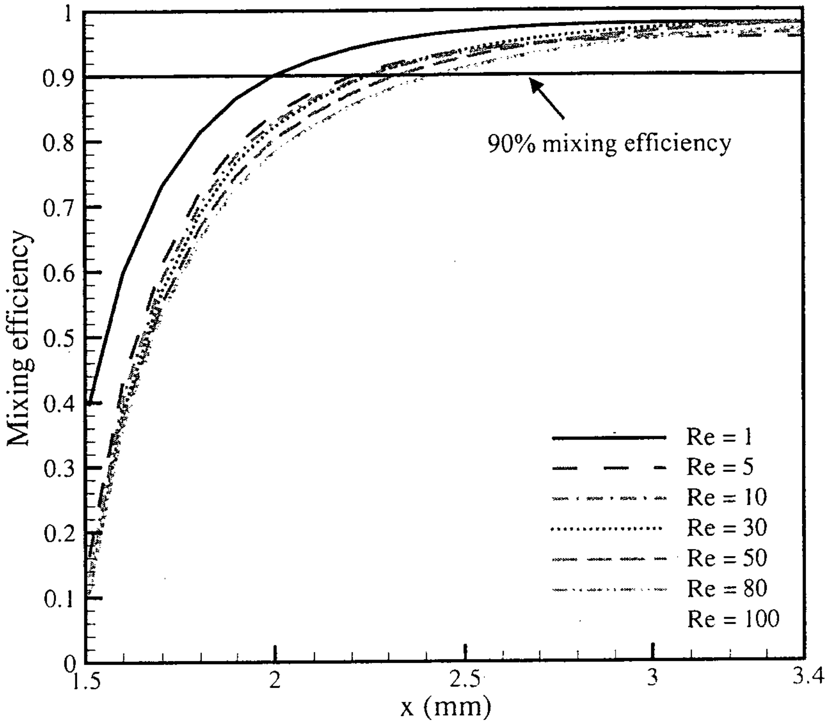

Figure 5.18: The mixing efficiency of the final design along the mixing length.

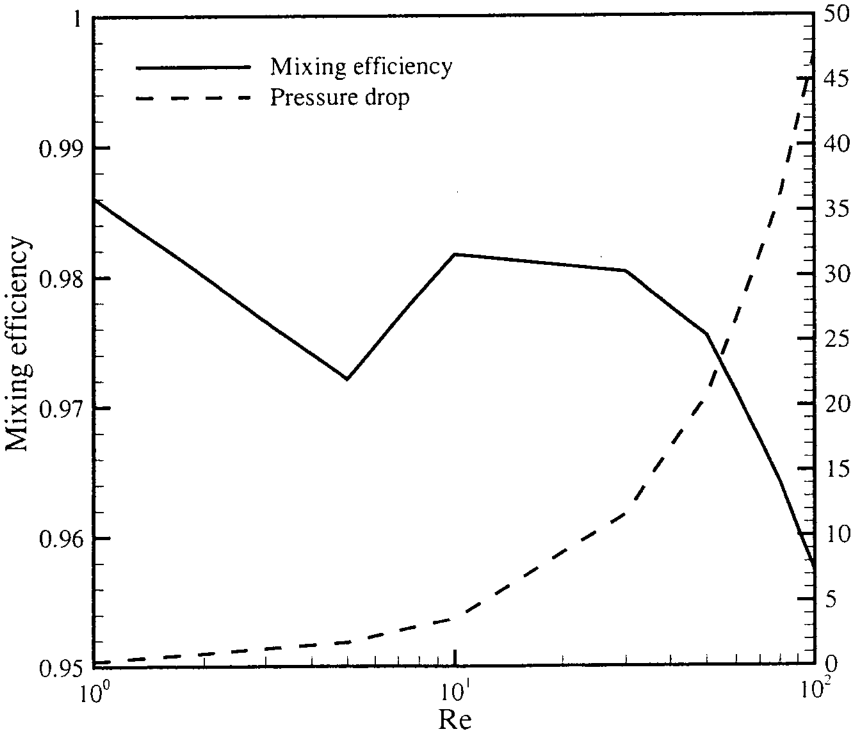

Figure 5.17: The mixing efficiency and pressure drop of the final design at $1 \leq Re \leq 100$.

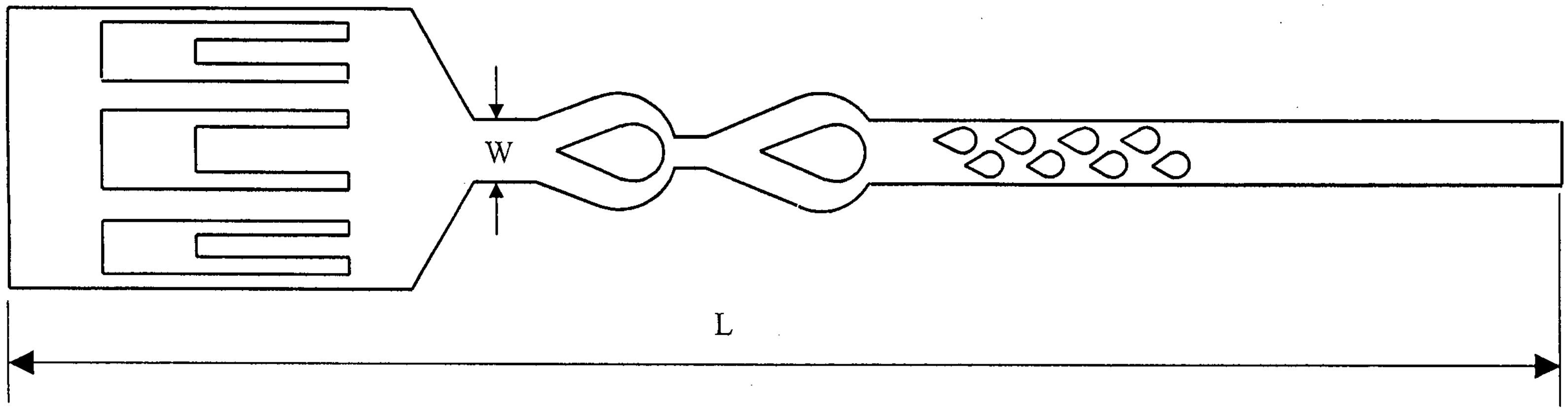

Figure 5.19: Schematic of the ICO micromixer.

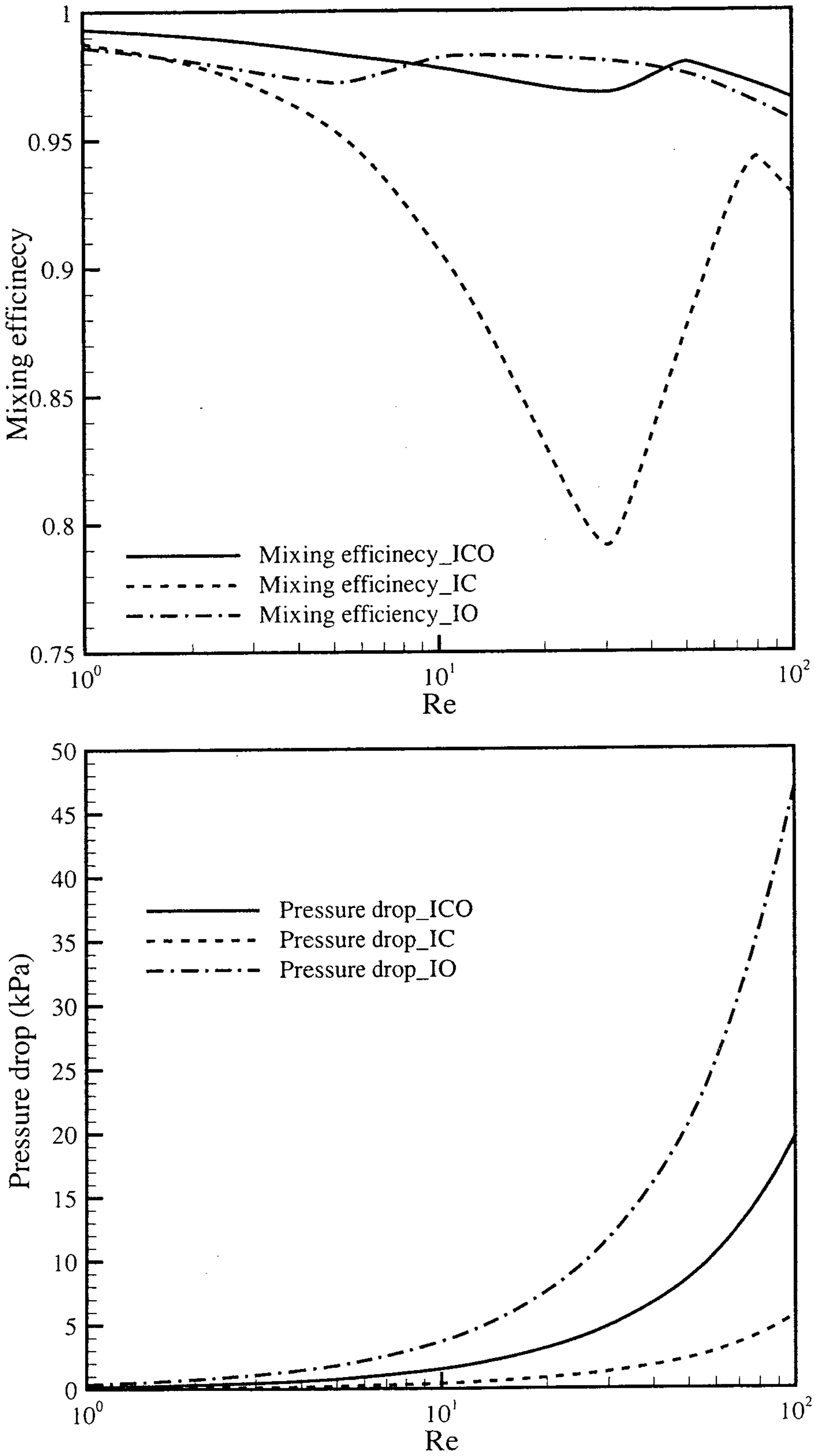

Figure 5.20: The mixing efficiency and pressure drop comparison of the three micromixers proposed in this study.

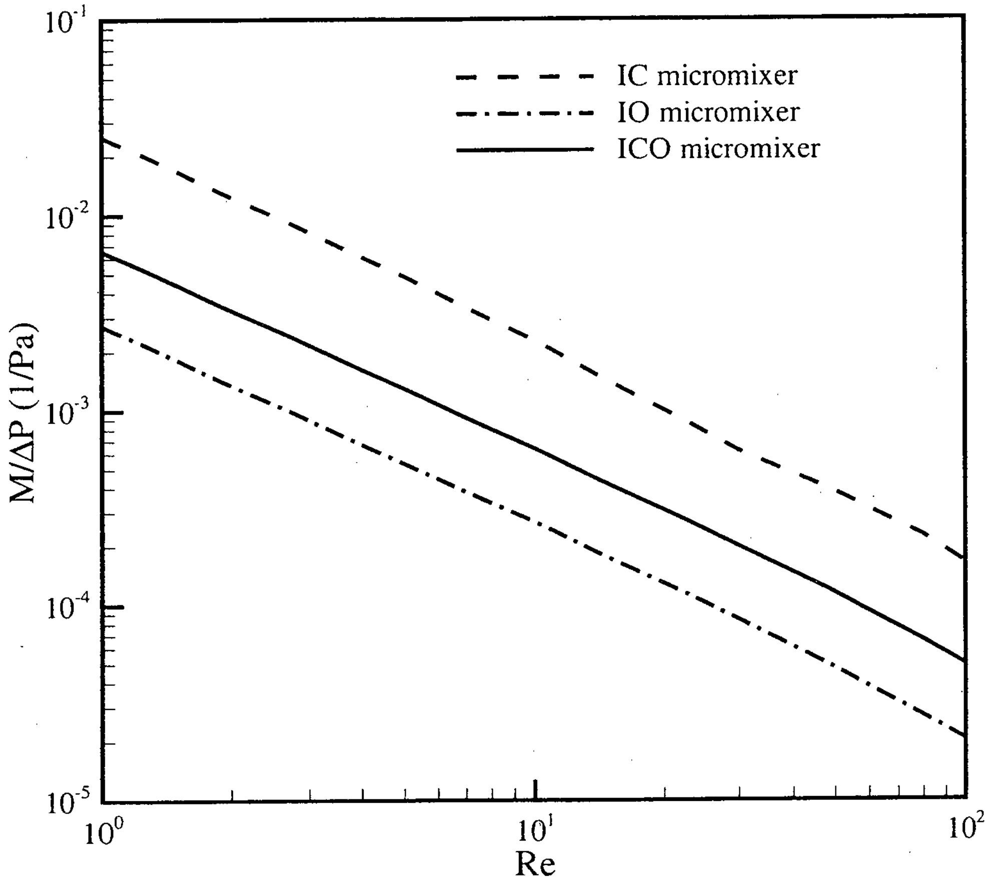

Figure 5.21: The ratios of mixing efficiency to pressure drop.

the pressure drop and maintains good mixing efficiency. Figure 5.21 shows the ratio of mixing efficiency to pressure drop of three micromixers. This ratio represents the energy utilization, which is the amount of mixing efficiency obtained with a pressure drop of one Pascal. The energy utilization of the ICO micromixer is higher than the IO micromixer, but lower than the IC micromixer. Taking into account three factors in micromixer development, high mixing efficiency, low pressure drop and high energy utilization, the ICO micromixer is considered as the best among the proposed three micromixers.

5.6 Summary

In order to increase the mixing efficiency up to 90%, a micromixer named the IO micromixer is investigated by numerical simulation. Circular-sector obstacles are positioned in the straight microchannel. The interdigital inlet is also applied to decrease the diffusion path. The simulation results show that the fluctuation of the interface among the gaps of obstacles could enhance the mixing. The DOE methodology is used to optimize the mixing element. Five parameters are selected for optimization. The sensitivities of parameters to the mixing efficiency are determined by the Taguchi method and three most important parameters are chosen for further optimization through RSM. The results show that the mixing efficiency reaches more than 95% in the range of *Re* from 1 to 100. However, the maximum pressure drop is up to 50 kPa at *Re* = 100. In order to obtain good mixing efficiency and low pressure drop, a combination of the IC and IO micromixers is designed. Compared to the IC and IO micromixers, the ICO micromixer successfully maintains good mixing efficiency and reduces the pressure drop.

Chapter 6

Conclusions and Future Directions

6.1 Conclusions

In this study, three micromixers, denoted as CO, IC and IO, were proposed and investigated by experiment and numerical simulation in order to quantify the mixing efficiency. The CO micromixer with cross-omega mixing element and T-shaped inlet was tested first by μ-IF and numerical simulation. To reduce the effect of numerical diffusion (ND) on the mixing evaluation in CFD work, a very fine mesh was applied to the first mixing cell. A very good match was obtained between CFD and experiment at $1 \leq Re \leq 50$ in the first cell. The results showed that the mixing efficiency decreased at $1 \leq Re \leq 10$ and increased at $10 \leq Re \leq 50$. This was considered to be caused by the change in mixing mechanism. Mass-diffusion was the dominant mixing mechanism at $Re \leq 10$. As Re increased, the mixing time was reduced which led to a decrease in mixing efficiency. At $Re \geq 10$, mass-advection became the key mixing mechanism which resulted in flow overlapping and folding. The interface was enlarged so that mixing was enhanced.

Through the understanding of the CO micromixer, a modification was made in order to improve the mixing efficiency and reduce the pressure drop. The IC micromixer was designed and investigated by numerical simulation since the numerical simulation was verified to be a valid tool to estimate the mixing in the CO micromixer investigation. The circular-section mixing element and interdigital structure inlet were used to decrease the diffusion path and reduce the pressure drop. Optimization of the IC micromixer was performed to obtain the optimal design dimensions using DOE methodology. The Taguchi method and Response Surface Model were utilized to determine the dimensions most sensitive to mixing and then the optimal design. In the optimal IC micromixer, the mixing efficiency decreased at $Re \leq 30$, and increased at $Re \geq 30$, for the same reasons as the CO micromixer. Flow rotation and overlap occurred at high *Re*, which induced the increased interface and enhanced the effect of mass-advection. The minimum mixing efficiency was determined as approximately 77% at $Re = 30$.

The IO micromixer was developed based on the IC micromixer. The critical value of *Re* in the IC micromixer was determined as 30 and the corresponding mixing efficiency was lower than 90%. In order to obtain the mixing efficiency larger than 90% at $1 \leq Re \leq 100$, circular-section obstacles were placed in the straight channel to distort the flow. Optimization was also performed and the interdigital structure inlet was applied. The mixing efficiency reached higher than 95% at $1 \leq Re \leq 100$. However, the pressure drop was up to 47 kPa, which was too high to be applied in LOC or μ-TAS.

Based on the IC and IO micromixers, a hybrid micromixer, denoted as ICO, was developed in order to achieve good mixing efficiency and low pressure drop. This micromixer could achieve good mixing ($\geq 95\%$) with relatively low pressure drop (≤ 20 kPa) at $1 \leq Re \leq 100$.

6.2 Contributions

The major contributions of this research work are the realization of three innovative in-plane on-chip functional micromixers. A new cross-omega structure has been proposed and demonstrated for the mixer using the Ansys-Fluent simulation package. Also, the passive scaled-up microfluidic mixer has been successfully fabricated and characterized using μ-IF. The experimental results show a reasonably good correlation with the simulated results. The mixing performance shows patterns similar to the Taylor dispersion, which consists of both diffusion and convection. The effect of geometry on the mixing performance is also quite significant. DOE methodology is completed in the investigation of the IC and IO micromixers. Compared with the designs found in literature, the present designs could achieve better mixing efficiency, as shown in Fig. 6.1. Due to its in-plane feature, the passive microfluidic mixer can be easily integrated into disposable LOC.

6.3 Challenges and Future Work

6.3.1 Challenges

Throughout the investigations of the present thesis, some challenges need to be overcome in the future work. First, two syringe pumps are used to supply the working

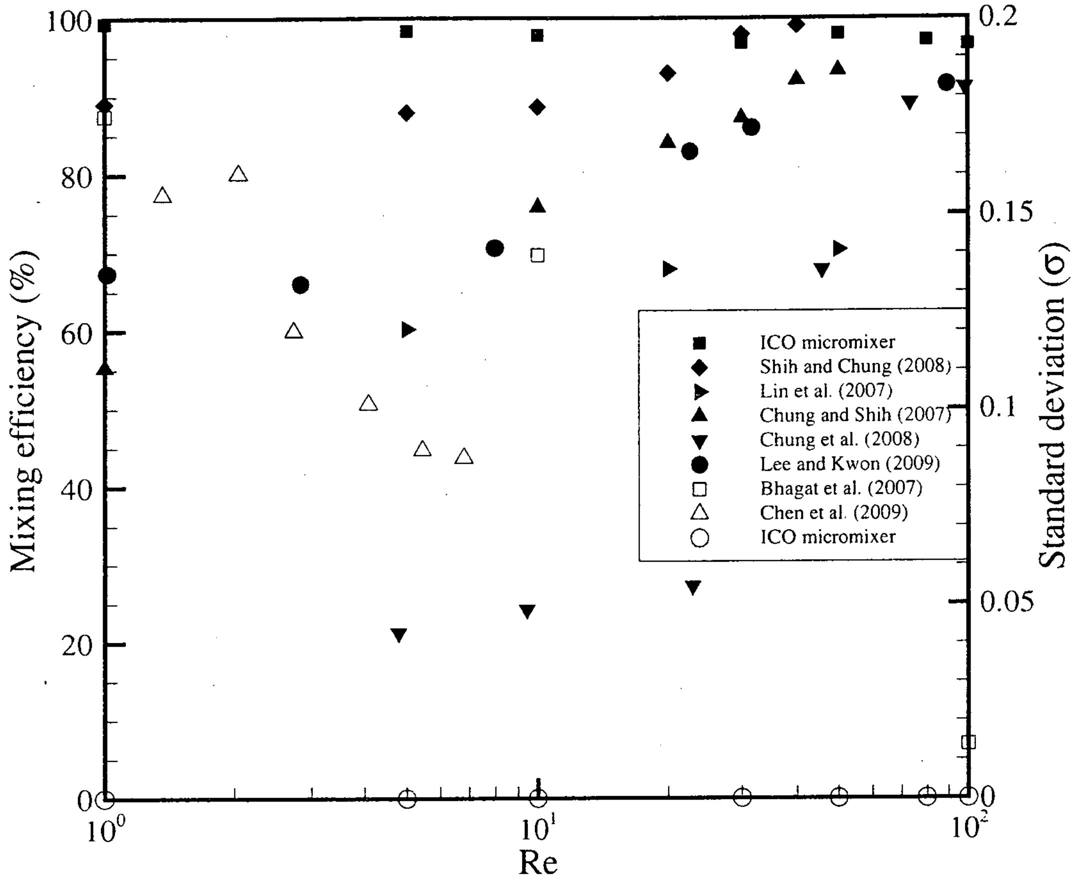

Figure 6.1: Comparison of mixing efficiency of proposed micromixer with literature designs. Solid symbols represent the mixing efficiency. Hollow symbols represent the standard deviation.

flows in this study. The available experimental range is limited due to the fluctuation of interface caused by the working principle of syringe pumps. Second, since μ-IF is an optical measurement, the light reflection near the walls could not be avoided and influences the measured signal near the walls. Third, the fabrication traces on the bottom of channels lead to the uneven light intensity distributions.

6.3.2 Future Work

A continuation of the current study could include some of the following improvements, and additions:

1. The numerical simulation was performed in the investigation of IC and IO micromixers. The μ-IF experiment should be completed in order to further validate the mixing quality obtained from CFD. The micro test-sections may be manufactured using polymer fabrication techniques (PMMA or PDMS), or glass etching. These methods provide a clear optical path for flow observation and light emission, without the fabrication traces. The μ-PIV experiment could be applied to measure the velocity distributions in order to further understand the mixing performance, while combining with concentration information.
2. With respect to the Induced Fluorescence technique, the current induced fluorescence technique applied the "Bino" mode to obtain the fluorescence signals over the channel depth. The results are adequate to evaluate the mixing efficiency. However, the concentration distributions in the transverse direction could not be obtained. The

scanning confocal technique is preferable to achieve the task. Through the use of scanning device integrated on the microscope, the concentration distributions along the channel depth could be obtained, which is good for understanding the mixing.

3. The present study only considered the constant diffusion coefficient. Since the diffusion coefficient is an important factor in the development of micromixers, the future work could extend to investigate the effect of variable diffusion coefficients on the mixing in order to determine the typical applications of the present designs within the given mixing length.
4. The two working fluids are miscible in the present work. However, in biological or chemical processes, the mixing of immiscible species is required, such as organic/inorganic substance. Different working fluids, like blood and protein, could be used to test the mixing quality of micromixers for immiscible species. Also, the physical mixing is only considered in the current work. Some applications of LOC platforms require the chemical reaction, such as medical diagnostics and cell activation. The chemical response time is independence on the mixing time. Hence, it is necessary to investigate the ability of micromixers to the applications with chemical reactions.
5. Gas phase may be generated during the chemical reactions, Two-phase flow is urgent to be investigated in the microchannels. The micro fluorescence technique could be used to trace the bubble generation and growth. The fluorescence technique also can

be used to measure the temperature of flows. It could extend to investigate the cooling performance of micro heat sink.

Publications from Thesis Work

Journal

Fan, Y. F. and Hassan, I., "Experimental and Numerical Investigation of a Scaled-up Passive Micromixer Using Fluorescence Technique", (in press) Journal of *Experiments in Fluids*, 2009.

Fan, Y. F. and Hassan, I., "Numerical Investigation of a Novel Passive Micromixer with Curved Microchannel and Slanted Grooves". Submitted to International Journal of *Numerical Methods for Heat and Fluid Flow*, 2009.

Conference

Fan, Y. F. and Hassan, I., "A New Passive Microfluidic Mixer: Design and Evaluation", *1st European Conference on Microfluidics-Microfluidics 2008-Bologna (MICROFLU2008)*, December 10-12, 2008.

Fan, Y. F. and Hassan, I., "The Numerical Investigation of a New Passive Micromixer with Improved Tesla Structure", *7th International Conference on Nanochannels, Microchannels, and Minichannels (ICNMM2009)*, June 22-24, 2009.

Fan, Y. F. and Hassan, I., "The Numerical Simulation of a Passive Interdigital Micromixer with Uneven Lamellar Width", *7th International Conference on Nanochannels, Microchannels, and Minichannels (ICNMM2009)*, June 22-24, 2009.

Fan, Y. F. and Hassan, I., "The Numerical Investigation of an Interdigital Micromixer with Circular-Sector Obstacles", *ASME 2009 Micro/Nanoscale Heat and Mass Transfer International Conference (MNHMT2009)*, December 18-21, 2009.

References

Agarwal, A., Sridharamurthy, S. S., Beebe, D. J., Jiang, H., "Programmable autonomous micromixers and micropumps", *Journal of Microelectromechanical Systems*, Vol. 14, 2005, 1409-1421.

Angele, K. P., Suzuki, Y., Miwa, J., Kasagi, N., "Development of a hig-speed scanning micro PIV system using a rotating disc", *Measurement Science and Technology*, Vol. 7, 2006, 1639-1646.

Bertsch, A., Heimgartner, S., Cousseau, P., Renaud, P., "Static micromixers based on large-scale industrial mixer geometry", *Lab on a Chip*, Vol. 1, 2001, 56-60.

Bessoth, F. G., deMello A. J., Manz, A., "Microstructure for efficient continuous flow mixing", *Anal. Commun.*, Vol. 36, 1999, 213 – 215.

Bhagat, A. A. S., Papautsky, I., "Enhancing particle dispersion in a passive planar micromixer using rectangular obstacles", *Journal of Micromechanics and Microengineering*, Vol. 18, 2008, p 085005 (9 pp.).

Bhagat, A. A. S., Peterson, E. T. K., Papautsky, I., "A passive planar micromixer with obstructions for mixing at low Reynolds numbers", *Journal of Micromechanics and Microengineering*, Vol. 17, 2007, 1017-24.

Bottausci, F., Cardonne, C., Meinhart, C., Mezic, I., "An ultrashort mixing length micromixer: the shear superposition micromixer", *Lab on a Chip*, Vol. 7, 2007, 396-8.

Branebjerg, J., Gravesen, P., Krog, J. P., Nielsen, C. R., "Fast mixing by lamination", *Proceedings of the IEEE Micro Electro Mechanical Systems (MEMS)*, 1996, 441-446.

Cao, J., Cheng, P., Hong, F. J., "A numerical study of an electrothermal vortex enhanced micromixer", *Microfluidics and Nanofluidics*, Vol. 5, 2008, 13-21.

Cerbelli, S., Giona, M., "On the estimate of mixing length in interdigital micromixers", *Chemical Engineering Journal*, Vol. 138, 2008, 523-37.

Cha, J., Kim, J., Ryu, S. K., Park, J., Jeong, Y., Park, S., Park, S., Kim, H. C., Chun, K., "A highly efficient 3D micromixer using soft PDMS bonding", *Journal of Micromechanics and Microengineering*, Vol. 16, 2006,1778-1782.

Chang, S., Cho, Y. H., "Static micromixers using alternating whirls and lamination", *Journal of Micromechanics and Microengineering*, Vol. 15, 2005, 1397-405.

Chen, C. K., Cho, C. C., "A combined active/passive scheme for enhancing the mixing efficiency of microfluidic devices", *Chemical Engineering Science*, Vol. 63, 2008, 3081-3087.

Chun, H., Kim, H. C., Chung, T. D., "Ultrafast active mixer using polyelectrolytic ion extractor", *Lab on a Chip*, Vol. 8, 2008, 764 – 71.

Chung, C. K., Shih, T. R., "A rhombic micromixer with asymmetrical flow for enhancing mixing", *Journal of Micromechanics and Microengineering*, Vol. 17, 2007, 2495-2504.

Chung, C. K., Shih, T. R., "Effect of geometry on fluid mixing of the rhombic micromixers", *Microfluidics and Nanofluidics*, Vol. 4, 2008, 419-425.

Chung, C. K., Shih, T. R., Chen, T. C., Wu, B. H., "Mixing behavior of the rhombic micromixers over a wide Reynolds number range using Taguchi method and 3D numerical simulations", *Biomedical Microdevices*, Vol. 10, 2008, 739-748.

Chung, C. K., Wu, C. Y., Shih, T. R., "Effect of baffle height and Reynolds number on fluid mixing", *Microsystem Technologies*, Vol. 14, 2008, 1317-1323.

DeMello, A. J., "Control and detection of chemical reactions in microfluidic systems", *Nature*, Vol. 442, 2006, 394-402.

Drese, K., S., "Optimization of interdigital micromixers via analytical modeling - exemplified with the SuperFocus mixer", *Chemical Engineering Journal*, Vol. 101, 2004, 403-407.

Ducrée, J., Brenner, T., Haeberle, S., Glatzel, T., Zengerle, R., "Multilamination of flows in planar networks of rotating microchannels", *Microfluidics and Nanofluidics*, Vol. 2, 2006, 78-84.

Ehrfeld, W., Golbig, K., Hessel, V., Löwe, H., Richter, T., "Characterization of mixing in micromixers by a test reaction: Single mixing units and mixer arrays", *Industrial and Engineering Chemistry Research*, Vol. 38, 1999, 1075-1082.

Fang, W-F and Yang, J-T, "A novel microreactor with 3D rotating flow to boost fluid reaction and mixing of viscous fluids", *Sensors and Actuators, B: Chemical*, Vol. 140, 2009, 629-642.

Floyd-Smith, T. M., Golden, J. P., Howell, P. B., Ligler, F. S., "Characterization of passive microfluidic mixers fabricated using soft lithography", *Microfluidics and Nanofluidics*, Vol. 2, 2006, 180-183.

Fukuyama, T., Shinmen, M., Nishitani, S., Yamaura, R., Ryu, I., "A Copper-Free Sonogashira Coupling Reaction in Ionic Liquids: An Easy Catalyst Recycling", *Symp Organomet Chem Jpn*, Vol.4, 2002, 1691-1694.

Hardt, S. Schönfeld, F., "Laminar mixing in different interdigital micromixers: II. Numerical simulations", *AIChE Journal*, Vol. 49, 2003, 578-584.

Hardt, S., Pennemann, H., Schönfeld, F., "Theoretical and experimental characterization of a low-Reynolds number split-and-recombine mixer", *Microfluidics and Nanofluidics*, Vol. 2, 2006, 237-248.

Hessel, V., Hardt, S., Löwe, H., Schönfeld, F., "Laminar mixing in different interdigital micromixers: I. Experimental characterization", *AIChE Journal*, Vol. 49, 2003, 566-577.

Hoffmann, M., Schluter, M., Rabiger, N., "Experimental investigation of liquid-liquid mixing in T-shaped micro-mixers using μ-LIF and μ-PIV", *Chemical Engineering Science*, Vol. 61, 2006, 2968-76.

Hong, C. C., Choi, J. W., Ahn, C. H., "A novel in-plane passive microfluidic mixer with modified Tesla structures", *Lab on a Chip*, Vol. 4, 2004, 109-13.

Howell P. B., Mott D. R., Golden J. P., Ligler F. S., "Design and evaluation of a Dean vortex-based micromixer", *Lab on a chip*, Vol.4, 2004, 663-9.

Hsieh, S. S., Huang, Y. C., "Passive mixing in micro-channels with geometric variations through μPIV and μLIF measurements", *Journal of Micromechanics and Microengineering*, Vol. 18, 2008, p 065017 (11 pp.).

Hu, Y. H., Chang, M., Lin, K. H., "A study of two fluids mixing in a helical-type micromixer", *Journal of Physics: Conference Series*, Vol. 48, 2006, 531-6.

Huang, S. H., Wang, S. K., Khoo, H. S., Tseng, F. G., "AC electroosmotic generated in-plane microvortices for stationary or continuous fluid mixing", *Sensors and Actuators, B: Chemical*, Vol. 125, 2007, 326-336.

Hung, C. I., Wang, K. C., Chyou, C. K., "Design and flow simulation of a new micromixer", *JSME International Journal, Series B (Fluids and Thermal Engineering)*, Vol. 48, 2005, 17-24.

Jang, L. S., Chao, S. H., Holl, M. R., Meldrum, D. R., "Resonant mode-hopping micromixing", *Sensors and Actuators, A: Physical*, Vol. 138, 2007, 179-186.

Jen, C. P., Wu, C. Y., Lin, Y. C., Wu, C. Y., “Design and simulation of the micromixer with chaotic advection in twisted microchannels”, *Lab on a Chip*, Vol. 3, 2003, 77-81.

Jeon, M. K., Kim, J. H., Noh, J., Kim, S. H., Park, H. G., Woo, S. I., “Design and characterization of a passive recycle micromixer”, *Journal of Micromechanics and Microengineering*, Vol. 15, 2005, 346-350.

Jiang, F., Drese, K. S., Hardt, S., Küpper, M., Schönfeld, F., “Helical flows and chaotic mixing in curved micro channels”, *AIChE Journal*, Vol. 50, 2004, 2297-2305.

Jin, S. Y., Liu, Y. Z., Wang, W. Z., Cao, Z. M., Koyama, H. S., “Numerical evaluation of two-fluid mixing in a swirl micro-mixer”, *Journal of Hydrodynamics*, Vol. 18, 2006, 542-546.

Kang, T. G., Singh, M. K., Kwon, T. H., Anderson, P. D., “Chaotic mixing using periodic and aperiodic sequences of mixing protocols in a micromixer”, *Microfluidics and Nanofluidics*, Vol. 4, 2008, 589-599.

Kim, D. S., Lee, I H., Kwon, T. H., Cho, D. W., “A barrier embedded Kenics micromixer”, *Journal of Micromechanics and Microengineering*, Vol. 14, 2004, 1294-301.

Kim, D. S., Lee, S. W., Kwon, T. H., Lee, S. S., “A barrier embedded chaotic micromixer”, *Journal of Micromechanics and Microengineering*, Vol. 14, 2004, 798-805.

Koch, M., Chatelain, D., Evans, A. G. R., Brunnschweiler, A., "Two simple micromixers based on silicon", *Journal of Micromechanics and Microengineering*, Vol. 8, 1998, 123-6.

Kumar, V., Aggarwal, M., Nigam, K. D. P., "Mixing in curved tubes", *Chemical Engineering Science*, Vol. 61, 2006, 5742-53.

Lee, J., Kwon, S., "Mixing efficiency of a multilamination micromixer with consecutive recirculation zones", *Chemical Engineering Science*, Vol. 64, 2009, 1223-31.

Lee, K., Kim, C., Shin, K. S., Lee, J. W., Ju, B. K., Kim, T. S., Lee, S. K., Kang, J. Y., "Fabrication of round channels using the surface tension of PDMS and its application to a 3D serpentine mixer", *Journal of Micromechanics and Microengineering*, Vol. 17, 2007, 1533-41.

Lee, N. Y., Yamada, M., Seki, M., "Development of a passive micromixer based on repeated fluid twisting and flattening, and its application to DNA purification", *Analytical and Bioanalytical Chemistry*, Vol. 383, 2005, 776-782.

Lee, S. W., Kim, D. S., Lee, S. S., Kwon, T. H., "A split and recombination micromixer fabricated in a PDMS three-dimensional structure", *Journal of Micromechanics and Microengineering*, Vol. 16, 2006, 1067-72.

Lee, S-H, Kang, H-J, Choi, B., "A study on the novel micromixer with chaotic flows" *Microsystem Technologies*, Vol. 15, 2009, 269-77.

Lin, C. H., Tsai, C. H., Pan, C. W., Fu, L. M., "Rapid circular microfluidic mixer utilizing unbalanced driving force", *Biomedical Microdevices*, Vol. 9, 2007, 43-50.

Lin, C. H., Tsai, C. H., Fu, L., M., "A rapid three-dimensional vortex micromixer utilizing self-rotation effects under low Reynolds number conditions", *Journal of Micromechanics and Microengineering*, Vol. 15, 2005, 935-943.

Lin, Y. C., Chung, Y. C., Wu, C. Y., "Mixing enhancement of the passive microfluidic mixer with J-shaped baffles in the tee channel", *Biomedical Microdevices*, Vol. 9, 2007, 215-21.

Liu, M., Xie, C., Zhang, X., Chen, Y., "Numerical simulation on micromixer based on synthetic jet", *Acta Mechanica Sinica/Lixue Xuebao*, Vol. 24, 2008, 629-636.

Liu, R. H., Ralf, L., Roberta L, D. S., Yang, J., Grodzinski, P., "Hybridization enhancement using cavitation microstreaming", *Analytical Chemistry*, Vol. 75, 2003,1911-1917.

Liu, R. H., Stremler, M. A., Sharp, K. V., Olsen, M. G., Santiago, J. G., Adrian, R. J., Aref, H., Beebe, D. J., "Passive mixing in a three-dimensional serpentine microchannel", *Journal of Microelectromechanical Systems*, Vol. 9, 2000,190-7.

Liu, R. H., Yang, J., Pindera, M. Z., Athavale, M., Grodzinski, P., "Bubble-induced acoustic micromixing", *Lab on a Chip*, Vol. 2, 2002, 151 – 157.

Liu, Y., Cheng, C., Liu, Y., Prud'homme, R. K., Fox, R. O., "Mixing in a multi-inlet vortex mixer (MIVM) for flash nano-precipitation", *Chemical Engineering Science*, Vol. 63, 2008, 2829-2842.

Löb, P., Drese, K. S., Hessel, V., Hardt, S., Hofmann, C., Löwe, H., Schenk, R., Schönfeld, F., Werner, B., "Steering of liquid mixing speed in interdigital micro mixers - From very fast to deliberately slow mixing", *Chemical Engineering and Technology*, Vol. 27, 2004, 340-345.

Lob, P., Pennemann, H., Hessel, V., "g/l-dispersion in interdigital micromixers with different mixing chamber geometries", *Chemical Engineering Journal*, Vol. 101, 2004, 75-85.

Lob, P., Pennemann, H., Hessel, V., Men, Y., "Impact of fluid path geometry and operating parameters on l/l-dispersion in interdigital micromixers", *Chemical Engineering Science*, Vol. 61, 2006, 2959-67.

Luo, W. J., "Effect of ionic concentration on electrokinetic instability in a cross-shaped microchannel", *Microfluidics and Nanofluidics*, Vol. 6, 2009, 189-202.

Mao, H., Yang, T., Cremer, P. S., "A microfluidic device with a linear temperature gradient for parallel and combinatorial measurements", *Journal of the American Chemical Society*, Vol. 124, 2002, 4432-4435.

Mengeaud, V., Josserand, J., Girault, H. H., "Mixing processes in a zigzag microchannel: Finite element simulations and optical study", *Analytical Chemistry*, Vol. 74, 2002, 4279-4286.

Mielnik, M. M., Ekatpure, R. P., Saetran, L. R., Schonfeld, F., "Sinusoidal crossflow microfiltration device - experimental and computational flowfield analysis", *Lab on a Chip*, Vol. 5, 2005, 897-903.

Mouza, A. A., Patsa, C. M., Schönfeld, F., "Mixing performance of a chaotic micro-mixer", *Chemical Engineering Research and Design*, Vol. 86, 2008, 1128-1134.

Nguyen, N. T., Wu, Z., "Micromixers-a review", *Journal of Micromechanics and Microengineering*, Vol. 15, 2005, R1-16.

Nguyen, T. N. T., Kim, M. C., Park, J. S., Lee, N. E., "An effective passive microfluidic mixer utilizing chaotic advection", *Sensors & Actuators: B. Chemical*, Vol. 132, 2008, 172-81.

Park, J. M., Kim, D. S., Kang, T. G., Kwon, T. H., "Improved serpentine laminating micromixer with enhanced local advection", *Microfluidics and Nanofluidics*, Vol. 4, 2008, 513-523.

Park, S. J., Kim, J. K., Park, J., Chung, S., Chung, C., Chang, J. K., "Rapid three-dimensional passive rotation micromixer using the breakup process", *Journal of Micromechanics and Microengineering*, Vol. 14, 2004, 6-14.

Pennemann, H., Hardt, S., Hessel, V., Löb, P., Weise, F., "Micromixer based liquid/liquid dispersion", *Chemical Engineering and Technology*, Vol. 28, 2005, 501-508.

Ribeiro, N., Green, M., Charron, M., "Assessment of multiple intravenous pumps infusing into a single site", *Journal of Nuclear Medicine Technology*, Vol. 36, 2008, 88-90

Schönfeld, F., Hardt, S., "Simulation of Helical Flows in Microchannels", *AIChE Journal*, Vol. 50, 2004, 771-778.

Schonfeld, F., Hessel, V., Hofmann, C., "An optimised split-and-recombine micro-mixer with uniform 'chaotic' mixing", *Lab on a Chip*, Vol. 4, 2004, 65-9.

Serra, C., Sary, N., Schlatter, G., Hadziioannou, G., Hessel, V., "Numerical simulation of polymerization in interdigital multilamination micromixers", *Lab on a chip*, Vol. 5, 2005, 966-73.

Shih, T. R., Chung, C. K., "A high-efficiency planar micromixer with convection and diffusion mixing over a wide Reynolds number range", *Microfluidics and Nanofluidics*, Vol. 5, 2008, 175-183.

Stroock, A. D., Dertinger, S. K. W., Ajdari, A., Mezic, I., Stone, H. A., Whitesides, G. M., "Chaotic mixer for microchannels", *Science*, Vol. 295, 25, 2002, 647-651.

Sudarsan, A. P., Ugaz, V. M., "Fluid mixing in planar spiral microchannels", *Lab on a Chip*, Vol. 6, 2006, 74-82.

Sudarsan, A. P., Ugaz, V. M., "Multivortex micromixing", *Proceedings of the National Academy of Sciences*, Vol. 103, 2006, 7228-7233.

Tafti, E. Y., Kumar, R., Cho, H. J., "Effect of laminar velocity profile variation on mixing in microfluidic devices: the sigma micromixer", *Applied Physics Letters*, Vol. 93, 2008, p 143504 (3 pp.).

Tsai, J. H., Lin, L., "Active microfluidic mixer and gas bubble filter driven by thermal bubble micropump", *Sensors and Actuators, A: Physical*, Vol. 97-98, 2002, 665-671.

Tung, K. Y., Yang, J. T., "Analysis of a chaotic micromixer by novel methods of particle tracking and FRET", *Microfluidics and Nanofluidics*, Vol. 5, 2008, 749-759.

Vanapalli, S. A., Van den Ende, D., Duits, M. H. G., Mugele, F., "Scaling of interface displacement in a microfluidic comparator", *Applied Physics Letters*, Vol. 90, 2007, 114109.

Wang, H., Iovenitti, P., Harvey, E., Masood, S., "Optimizing layout of obstacles for enhanced mixing in microchannels", *Smart Materials and Structures*, Vol. 11, 2002, 662-7.

Wang, L., Yang, J. T., Lyu, P. C., "An overlapping crisscross micromixer", *Chemical Engineering Science*, Vol. 62, 2007, 711-20.

Wu, Z., Nguyen, N. T., "Convective-diffusive transport in parallel lamination micromixers", *Microfluidics and Nanofluidics*, Vol. 1, 2005, 208-217.

Xia, H. M., Shu, C., Wan, S. Y. M., Chew, Y. T., "Influence of the Reynolds number on chaotic mixing in a spatially periodic micromixer and its characterization using dynamical system techniques", *Journal of Micromechanics and Microengineering*, Vol. 16, 2006, 53-61.

Yang, J. T., Huang, K. J., Tung, K. Y., Lyu, P. C., "A chaotic micromixer modulated by constructive vortex agitation", *Journal of Micromechanics and Microengineering*, Vol. 17, 2007, 2084-92.

Yang, J. T., Lin, K. W., "Mixing and separation of two-fluid flow in a micro planar serpentine channel", *Journal of Micromechanics and Microengineering,* Vol. 16, 2006, 2439-48.

Yang, S-Y, Lien, K-Y, Huang, K-J, Lei, H-Y, Lee, G-B, "Micro flow cytometry utilizing a magnetic bead-based immunoassay for rapid virus detection", *Biosensors and Bioelectronics*, Vol. 24, 2008, 861-868.

Yang, S-Y., Lin, J-L., Lee, G-B., "A vortex-type micromixer utilizing pneumatically driven membranes", *Journal of Micromechanics and Microengineering*, Vol. 19, 2009, 035020 (9 pp.).